
[All ETDs from UAB](#)

[UAB Theses & Dissertations](#)

1999

Ab initio molecular dynamics simulation of charged and neutral solitons in polyacetylene.

Todd Edward DeVore
University of Alabama at Birmingham

Follow this and additional works at: <https://digitalcommons.library.uab.edu/etd-collection>

Recommended Citation

DeVore, Todd Edward, "Ab initio molecular dynamics simulation of charged and neutral solitons in polyacetylene." (1999). *All ETDs from UAB*. 6358.
<https://digitalcommons.library.uab.edu/etd-collection/6358>

This content has been accepted for inclusion by an authorized administrator of the UAB Digital Commons, and is provided as a free open access item. All inquiries regarding this item or the UAB Digital Commons should be directed to the [UAB Libraries Office of Scholarly Communication](#).

INFORMATION TO USERS

This manuscript has been reproduced from the microfilm master. UMI films the text directly from the original or copy submitted. Thus, some thesis and dissertation copies are in typewriter face, while others may be from any type of computer printer.

The quality of this reproduction is dependent upon the quality of the copy submitted. Broken or indistinct print, colored or poor quality illustrations and photographs, print bleedthrough, substandard margins, and improper alignment can adversely affect reproduction.

In the unlikely event that the author did not send UMI a complete manuscript and there are missing pages, these will be noted. Also, if unauthorized copyright material had to be removed, a note will indicate the deletion.

Oversize materials (e.g., maps, drawings, charts) are reproduced by sectioning the original, beginning at the upper left-hand corner and continuing from left to right in equal sections with small overlaps. Each original is also photographed in one exposure and is included in reduced form at the back of the book.

Photographs included in the original manuscript have been reproduced xerographically in this copy. Higher quality 6" x 9" black and white photographic prints are available for any photographs or illustrations appearing in this copy for an additional charge. Contact UMI directly to order.

UMI[®]

Bell & Howell Information and Learning
300 North Zeeb Road, Ann Arbor, MI 48106-1346 USA
800-521-0600

AB INITIO MOLECULAR DYNAMICS SIMULATION
OF CHARGED AND NEUTRAL SOLITONS IN POLYACETYLENE

by

TODD EDWARD DEVORE

A DISSERTATION

Submitted to the graduate faculty of The University of Alabama at Birmingham,
in partial fulfillment of the requirements for the degree of
Doctor of Philosophy

BIRMINGHAM, ALABAMA

1999

UMI Number: 9946704

UMI Microform 9946704
Copyright 1999, by UMI Company. All rights reserved.

**This microform edition is protected against unauthorized
copying under Title 17, United States Code.**

UMI
300 North Zeeb Road
Ann Arbor, MI 48103

ABSTRACT OF DISSERTATION
GRADUATE SCHOOL, UNIVERSITY OF ALABAMA AT BIRMINGHAM

Degree Doctor of Philosophy Program Physics

Name of Candidate Todd Edward DeVore

Committee Chair Dr. Ryoichi Kawai

Title Ab Initio Molecular Dynamics Simulation of Charged
and Neutral Solitons in Polyacetylene

The polyacetylene (PA) system has a two-fold degenerate ground state that allows for excitations known as solitons. Solitons are believed to be highly mobile, with a predicted effective mass on the order of the electron mass m_e . Both semiempirical and first principles methods have been used by others to investigate static properties of solitons. Dynamics studies have been limited almost entirely to semiempirical methods. We employ density functional theory and Car-Parrinello ab initio molecular dynamics to investigate charged and neutral solitons in finite polyenes (C_nH_{n+2}). Calculations are performed for both even-membered (n is even) and odd-membered polyenes. Our calculations indicate that these finite systems have a dimerization which is reasonably close to observed experimental values obtained from PA films. We find a soliton state for the ground state of odd-membered polyenes of the trans-transoid isomer of PA.

Car-Parrinello ab initio molecular dynamics allows us to observe the interaction of the soliton with the chain end or conformational defects while treating electron-electron correlation and electron-phonon coupling from first principles. We simulate mobile neutral and charged solitons in polyene chains both with and without an important common defect. The defect we include in the otherwise trans-transoid chain of PA is a single bond that forms a cis-transoid structure. Our simulations indicate the soliton has a small effective mass and moves with an average speed of about 1.0×10^5 m/s in the absence of an external field, in general agreement with

previous results from semiempirical studies. However, we find the soliton's motion is greatly affected by the finite chain ends, lattice vibrations, and the presence of the cis-transoid defect. The qualitative nature of the soliton motion with these factors included has not been previously shown.

ACKNOWLEDGEMENTS

I express my sincere appreciation to Dr. Ryoichi Kawai. He has always been willing to share his vast knowledge on many subjects. I have been able to conduct research under his direction at interesting locations, including the Wright Patterson Air Force Base and University of California San Diego.

I am grateful to my committee members, Dr. Joseph Harrison, Dr. David Agresti, Dr. Tracy Hamilton, and Dr. Charles Katholi.

Finally, I would like to thank Dr. Ed Wills and Dr. James Martin for their support and insight regarding my development as a laboratory coordinator and instructor while I completed this work.

TABLE OF CONTENTS

	<i>Page</i>
ABSTRACT	ii
ACKNOWLEDGEMENTS	iv
TABLE OF CONTENTS	v
LIST OF TABLES	vii
LIST OF FIGURES	viii
1 INTRODUCTION	1
2 OVERVIEW OF PA INVESTIGATIONS	6
2.1 SSH model	6
2.2 Ab initio PA studies	9
2.3 Soliton state in the SSH model	10
2.4 Experimental evidence for solitons	12
3 AB INITIO CALCULATION METHODOLOGY	19
3.1 Density functional theory and the LDA approximation	19
3.2 Exchange-correlation energy functional	23
3.3 Basis set and energy minimization	25
3.4 Testing the implementation of the plane-wave LDA/LSDA method . .	29
3.5 Gradient corrections to the local density approximation	29
3.6 Molecular dynamics methodology	31
4 RESULTS OF AB INITIO CALCULATIONS OF MODEL PA	34
4.1 Results for even-membered polyenes	35
4.2 Polyenes with a <i>cis</i> bond defect	37
4.3 Odd-membered polyenes of <i>trans</i> -PA: Static calculations	41
4.4 Odd-membered <i>trans</i> polyenes with one <i>cis</i> bond	45
5 DYNAMICS SIMULATION OF SOLITONS	55

TABLE OF CONTENTS (Continued)

	<i>Page</i>
5.1 Brief summary of previously published simulation results	55
5.2 Initial conditions used for this dynamical study	58
5.3 Initial configurations for all- <i>trans</i> polyenes	59
5.4 Initial configurations for polyenes with one <i>cis</i> bond defect	59
 6 CAR-PARRINELLO AB INITIO MOLECULAR DYNAMICS RESULTS .	 67
6.1 Details of soliton motion: A neutral soliton in all- <i>trans</i> $C_{33}H_{35}$	68
6.2 Details of soliton motion: A negatively charged soliton in a <i>trans</i> polyene $C_{33}H_{35}$ with a central <i>cis</i> bond	71
 7 CONCLUSIONS	 106
 APPENDIX: LDA CALCULATION IN MOMENTUM SPACE FORMALISM	 108
 LIST OF REFERENCES	 127

LIST OF TABLES

<i>Table</i>	<i>Page</i>
I Predicted energetic and structural parameters as calculated by Suhai using different theoretical methods and a double-zeta basis set.	10
II Theoretical and experimental geometries.	30
III Bond alternation as predicted by LDA with and without generalized gradient correction.	34
IV Predicted lengths of short/long central bonds in even-membered polyene systems.	36
V Average speed of the soliton in each simulated system for each pass over the chain center (m/s).	68

LIST OF FIGURES

<i>Figure</i>		<i>Page</i>
1	Geometry of the two experimentally detected isomers of PA.	5
2	Two possible configurations or "phases" of <i>trans</i> -PA.	16
3	The soliton kink and antikink both connect the two possible phases of bond ordering.	16
4	Energy as a function of displacement u away from equidistant C-C bonding.	17
5	Net spin density predicted from SSH model for the width parameters $l = 7$ and $l = 11$	18
6	Reversed spin-charge relation for neutral, negative, and positive soliton	18
7	Example of an all- <i>trans</i> C_nH_{n+2} polyene.	47
8	Carbon-carbon bond lengths and HOMO density 1 au above the polyene plane for $C_{32}H_{34}$	47
9	The two possible isomers of all- <i>cis</i> -PA.	48
10	Structure, total energy, and calculated bond lengths for $C_{10}H_{12}$ with one <i>cis</i> bond	49
11	Comparison of carbon-carbon bond lengths between all- <i>trans</i> $C_{18}H_{20}$ and the same system with a central <i>cis</i> bond and either a straight or bent geometry.	50
12	Lowest-energy bond lengths	51
13	Order parameter Δr_n from calculated geometry of $C_{33}H_{35}^-$ and $C_{17}H_{19}$.	52
14	Spin-polarization density along a line parallel to the $C_{33}H_{35}$ chain axis 1 au above the polyene plane.	53
15	Calculated carbon-carbon bond lengths and spin-polarization density 1 au above plane of $C_{31}H_{33}$ polyene with a <i>cis</i> bond	54

LIST OF FIGURES (Continued)

<i>Figure</i>		<i>Page</i>
16	Schematic representation of an odd-membered polyene with a uniform, uninterrupted dimerization.	62
17	Bond order parameter for the initial geometry used by Förner et al. to initiate soliton dynamics.	62
18	Starting bond length configurations for our dynamics simulations. . .	63
19	Initial bond order parameter for all- <i>trans</i> systems with 33 carbon atoms	64
20	Schematic picture of the polyene with one <i>cis</i> bond for which dynamics simulations were performed.	64
21	Initial bond lengths of polyene system with one <i>cis</i> bond.	65
22	Bond order parameter of polyene system with one <i>cis</i> bond at the beginning of dynamics simulation.	66
23	Order parameter from $t = 0$ to 250 au	75
24	Order parameter from $t = 300$ to 550 au	76
25	Order parameter from $t = 600$ to 850 au	77
26	Order parameter from $t = 900$ to 1150 au	78
27	Order parameter from $t = 1200$ to 1450 au	79
28	Order parameter from $t = 1500$ to 1750 au	80
29	Order parameter from $t = 1800$ to 2050 au	81
30	Order parameter from $t = 2100$ to 2350 au	82
31	Order parameter from $t = 2400$ to 2550 au	83
32	Position of each kink and antikink vs. time	84
33	Spin-polarization density 1 au above the plane of the polyene	85
34	Potential energy and carbon-carbon bond lengths for times shown . .	86
35	Potential energy and carbon-carbon bond lengths for times shown . .	87

LIST OF FIGURES (Continued)

<i>Figure</i>		<i>Page</i>
36	Order parameter from $t = 0$ to 250 au	88
37	Order parameter from $t = 300$ to 550 au	89
38	Order parameter from $t = 600$ to 850 au	90
39	Order parameter from $t = 900$ to 1150 au	91
40	Order parameter from $t = 1200$ to 1450 au	92
41	Order parameter from $t = 1500$ to 1750 au	93
42	Order parameter from $t = 1800$ to 2050 au	94
43	Order parameter from $t = 2100$ to 2350 au	95
44	Order parameter from $t = 2400$ to 2650 au	96
45	Position of each kink and antikink vs. time	97
46	HOMO level density 1 au above polyene at $t = 0$	97
47	HOMO density and change for times specified and change in HOMO density between times specified 1 au above the plane of the polyene. .	98
48	HOMO density and change for times specified and change in HOMO density between times specified 1 au above the plane of the polyene. .	99
49	HOMO density and change for times specified and change in HOMO density between times specified 1 au above the plane of the polyene. .	100
50	HOMO density and change for times specified and change in HOMO density between times specified 1 au above the plane of the polyene. .	101
51	HOMO density and change for times specified and change in HOMO density between times specified 1 au above the plane of the polyene. .	102
52	Difference in bond length between horizontal <i>cis</i> bond (of length "b") and adjacent bond (of length "a") vs. time.	103
53	Bond length of terminal carbon-carbon bond vs. time	104
54	Change in potential energy vs. time for polyene with <i>cis</i> bond	105

1 INTRODUCTION

Polyacetylene (PA) is the simplest example of a material categorized as a conducting polymer. The polymer takes the form of either of two isomers, *trans-transoid* or *cis-transoid*. These are shown schematically in Fig. 1. In both forms the carbon atoms have three out of four valence electrons in sp^2 hybridized orbitals forming σ type bonds in the molecular plane. Each C-H unit contributes a π electron to form a quasi-one-dimensional valence band along the chain. The *trans-transoid* isomer is the thermodynamically stable form of polyacetylene [1]. While *cis-transoid* and *trans-transoid* polyacetylene can coexist at low temperatures, pure *cis*-PA will be isomerized to *trans*-PA if the film is heated above 150° C. This dissertation will focus on the *trans-transoid* isomer. From here on the abbreviation PA shall refer to *trans-transoid* polyacetylene unless otherwise noted.

Pure PA is an electrical insulator with a band gap of about 1.5 eV. The conductivity of the material has a value on the order of 10^{-4} S cm⁻¹ [2]. However, PA may be doped with impurity atoms such as iodine to raise the conductivity over many orders of magnitude. The maximum conductivity of doped PA is over 10^5 S cm⁻¹, which is comparable to metals like Cu [2,3].

One obvious reason for interest in conducting polymers is the wide range of applications that could be found for materials with mechanical properties of plastics that conduct like metals. There are processes readily available for casting thin, flexible layers of conducting polymer film on a wide variety of substrates. Practical applications include preventing the buildup of charge on surfaces with antistatic polymer films [4]. Camouflage fabrics can be treated to prevent radar reflection [4]. Considerable effort has been focused on using conducting polymers as a replacement

for conventional inorganic semiconductors for making LEDs [5]. A main drawback encountered thus far is the generally faster degradation rate of the polymer materials due to overheating or oxidative reactions. Environmental instability is particularly severe for the PA films, although the material is still intensively studied due to its unique properties.

Despite the simplicity of the idealized PA system $(CH)_n$, real polymer materials are very complex due to the high degree of disorder in the crystalline structure. The details of a real sample's morphology are extremely sensitive to polymerization methods and conditions and are difficult to reproduce. The polymer material is grown as a film which can have thickness from 10^{-5} to 0.5 cm [3]. The as-grown films consist of randomly oriented fibrils about 200-300 Å in diameter and are typically a few thousand Å in length [2]. The as-grown films are mostly of the *cis*-PA form which is converted to the *trans* form above 150° C. The films can be stretched and the fibrils aligned to produce material with a high degree of crystallization. Experimental data indicate 75-90% of such a sample is crystallized. The disordered regions are not well characterized due to the combination of intrinsic defects such as cross-links, chain twists, and interstitial impurities. Only with high quality stretched samples is it possible to achieve conductivities on the order of 10^5 S cm⁻¹ after doping [2]. Refinements in preparation techniques have led to an increase of the maximum conductivity of doped PA over almost four orders of magnitude since the late 1970's.

While the quality of the material has improved, scientists have continued to study PA intensively to understand its insulator-metal transition and to explain its unusual transport, optical, and magnetic properties. Experiments show pure PA exhibits Curie paramagnetism corresponding to about one spin per several thousand CH groups [6]. Electron spin resonance (ESR) experiments show these spins are highly diffusive along the polymer chains [7]. If one assumes that charge is associated with these spins, a significant electric current is expected. However, only a very small

current is observed. When crystalline PA is doped with donor impurity atoms, the Curie paramagnetism decreases while the conductivity increases. In order to explain these results, it is necessary to assume the existence of spinless charged excitations. Such unusual excitations can be explained by traveling solitons. The nature of soliton transport along a PA chain is the main focus of this dissertation. Soliton excitations are unique to the *trans* isomer of the polymer and owe their existence to the quasi-one-dimensionality of the system, a two-fold degenerate ground state, and coupling between ionic and electronic degrees of freedom.

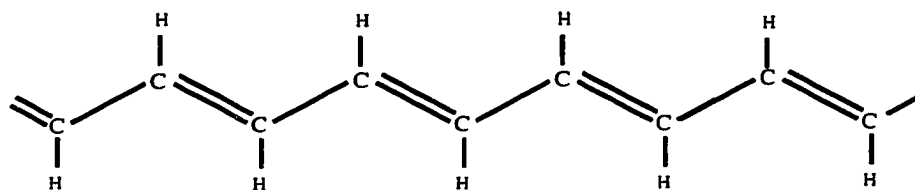
Microscopic details of soliton transport are unknown due to the complexity of the PA material. These complications arise from interactions between neighboring chains, cross-links, sp^3 carbon defects, bending and twisting of fibrils in crystalline PA, and residual *cis*-PA sections. It is estimated from infrared-absorption data [8] and near-infrared photoluminescence experiments [9] that after heat treatment isomerization the *cis* isomer still exists at a level of at least 5-7%. Due to this large concentration, these residual *cis* bonds may significantly affect the dynamics of charge and spin carriers in the PA system.

Idealized PA systems have been extensively investigated with semiempirical methods that treat explicitly only the π electrons that contribute to the valence band of PA. Highly accurate *ab initio* methods have also been employed. Among *ab initio* methods, density functional theory (DFT) has been used by many groups due to the computational efficiency of this method.

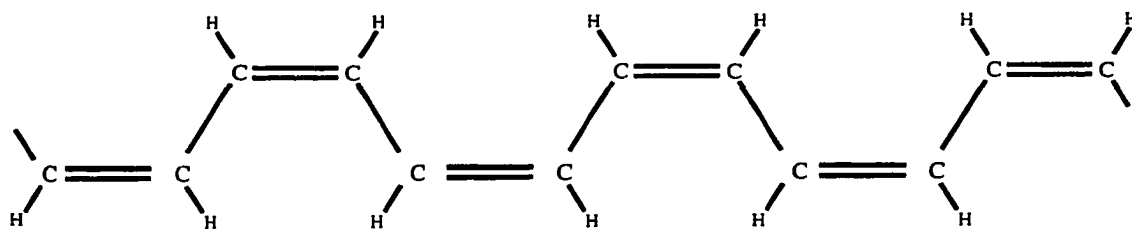
The investigation of soliton dynamics has been almost exclusively limited to semi-empirical methods. Generally, *ab initio* investigations have focused on static structures. It is highly desirable to investigate soliton dynamics with a first-principles method. Since solitons exist due to electron-phonon interaction, a method that treats both electrons and nuclear motion from first principles is necessary. Furthermore, it is difficult to treat impurities with semiempirical methods due to the uncertainty

of how semiempirical parameters should be determined. This investigation employs DFT with the local density approximation (LDA) and Car-Parrinello ab initio molecular dynamics. This method allows us to simulate dynamics from first principles. Mobile solitons in both idealized single PA chains and chains with a *cis* bond defect are considered. Results will be compared with previous model calculations and experiments where applicable. Our goal is to investigate the transport properties of a soliton in pure and defective PA using first-principles methods. We also investigate the applicability of a popular semi-empirical method to the study of soliton dynamics. The famous model of Su, Schrieffer, and Heeger (SSH model) [10,11] has been to this point a de facto standard paradigm used to discuss mobile solitons.

The general outline of the document proceeds as follows: The second major section, following this Introduction, describes PA in more detail. Evidence supporting the existence of the soliton is reviewed. An overview of the theoretical methods used to investigate PA is given. The third major section reviews the methodology of DFT/LDA and Car-Parrinello ab initio molecular dynamics simulations. Test results of our density functional code for small hydrocarbon molecules are given. The fourth major section will describe our results for the ground state of various finite chains of PA. Results are shown for polyenes both with and without the common defect of a *cis* bond. The fifth major section reviews briefly results from previous studies of soliton dynamics. The sixth major section describes our own Car-Parrinello ab initio molecular dynamics simulation results for mobile solitons in finite polyenes with and without a defect. The final section concludes and summarizes what can be learned about soliton transport from ab initio molecular dynamics simulations of mobile solitons.



trans-transoid PA (*trans*-PA)



cis-transoid PA (*cis*-PA)

FIG. 1: Geometry of the two experimentally detected isomers of PA. *trans*-PA is the main focus of this study.

2 OVERVIEW OF PA INVESTIGATIONS

Peierls [12] proved a general theorem on the stability of a one-dimensional lattice. For a system with a partially filled valence electron energy band, the theorem predicts the nuclear configuration to be unstable. It states a new nuclear configuration with a larger unit cell is formed such that a band gap appears at a new Brillouin zone boundary. For example, a system with a half-filled band forms a unit cell twice as large as the original. The effect of unequal distances between a nuclear site and its nearest neighbors caused by this instability is called dimerization. Although PA is not exactly a linear system, it is generally considered the physical system most likely to exhibit dimerization due to the Peierls instability. X-ray scattering [13] and nuclear magnetic resonance studies [14] confirm the system does exhibit alternating carbon-carbon bond lengths (see Fig. 1). These lengths are approximately 1.44 Å and 1.36 Å.

Bond ordering can occur with either of the two phases shown in Fig. 2. If the two different phases coexist in the same system, there must be a domain boundary as shown in Fig. 3. This domain boundary is typically referred to as a soliton. In this dissertation, I shall call a boundary consisting of two adjacent single bonds a kink, and I shall call a boundary with two adjacent double bonds an antikink.

In this section I explain the Peierls instability and structure of the domain boundary using an empirical method. Empirical methods have been used extensively to anticipate important physical characteristics of PA and the soliton excitation.

2.1 SSH model

In 1979 Su et al. [10] investigated PA using a tight-binding model with explicit electron-phonon coupling. In their model only π electrons are considered and the effects of σ electrons are included as an interaction potential between the nuclei. Taking a harmonic approximation, their Hamiltonian is given by

$$H = \frac{K}{2} \sum_n (u_n - u_{n-1})^2 + \frac{M}{2} \sum_n \dot{u}_n^2 - \sum_{n,s} \left[t_0 + \alpha(u_n - u_{n+1}) \right] (C_{n+1,s}^\dagger C_{n,s} + C_{n,s}^\dagger C_{n+1,s}), \quad (1)$$

where t_0 is the electron hopping integral between nearest neighbors on an undimerized carbon chain, α is the electron-phonon coupling constant, K is a spring constant arising from the σ bonds and M is the mass of a CH unit. The dynamical variables u_n represent the displacement of the n th carbon site from its equilibrium position on the undimerized chain. In this one-dimensional model, u_n is the actual nuclear displacement projected on the axis of the polymer. The bonded carbon-hydrogen pairs are considered to move as a unit. The $C_{n,s}$ ($C_{n,s}^\dagger$) is the annihilation (creation) operator for the π electron on the n th site with spin s .

The dimerization is described by the alternating sign of the displacement parameter u , which oscillates in sign for the perfectly dimerized chain.

$$u_l = (-1)^l u_0 = u_0 e^{\pm 2il k_f a}. \quad (2)$$

$$k_f = \frac{\pi}{2a}. \quad (3)$$

Here u_0 is the absolute value of the displacement of each C-H unit, k_f is the Fermi wave vector, and $2a$ is the size of the unit cell. The parameter a is the projection of the equidistant (average) C-C bond length along the one-dimensional axis of the polymer. With this alternation, the resonance integrals $t_{l,l+1}$ must also have an alternating value:

$$t(u_l, u_{l+1}) = t_0 - \frac{1}{2} (-1)^l \Delta_0. \quad (4)$$

$$\Delta_0 = 4\alpha u_0. \quad (5)$$

The quantity Δ , called the bond alternation order parameter, has units of energy and is directly related to the dimerization. The energy dispersion relation for this dimerized system with 2 C-H pairs in each unit cell can be written as follows:

$$E_k^2 = 4t_0 \cos^2(ka) + \Delta_0^2 \sin^2(ka). \quad (6)$$

This relation shows there is a band gap of magnitude $2\Delta_0$ at the zone boundary. A band gap of approximately 1.4-1.8 eV is found by experiment [3, 15].

The equilibrium displacement u_0 depends on the choice of parameters used. There is no unique way to determine α and K in this model. Values are typically determined such that the observed band gap of about 1.5 eV is reproduced and u_0 is a few hundredths of an angstrom, which compares well to the experimental value of about 0.030 Å [13]. The following set of values are commonly used:

$$\Delta_0 = 0.7 \text{ eV}. \quad (7)$$

$$W = 4t_0 = 10 \text{ eV} (W \text{ is bandwidth}). \quad (8)$$

$$\alpha = 4.1 \frac{\text{eV}}{10^{-10}m}. \quad (9)$$

$$K = 21 \frac{\text{eV}}{10^{-10}m}. \quad (10)$$

The adiabatic potential $E(u)$ for a uniformly dimerized system is shown in Fig. 4. $E(u = 0)$ corresponds to the unstable nondimerized geometry, while $E(u = \pm u_0)$ is the energy for the two degenerate ground states. The existence of these two degenerate ground states is consistent with Peierl's prediction. As indicated in Fig. 4 the two degenerate minima of $E(u)$ correspond to the two possible phases shown in Fig. 2. Without dimerization [at $E(u = 0)$], the system is symmetric about reflection in any plane perpendicular to the PA chain and containing a (CH) group; with dimerization, such a reflection brings phase A into phase B and vice versa. In physical terms this phenomenon is called "symmetry breaking" [16].

2.2 Ab initio PA studies

The small energy differences and very small atomic displacements away from equidistant bond positions are a challenge for ab initio methods. Many ab initio studies have been performed on PA since the late 1980's. The explicit inclusion of electron-electron interaction and the effect this may have on the predicted dimerization suggest an opportunity to generalize the Peierls mechanism to include the effect of these interactions. A very wide range of methods has been used to study PA. These methods include Hartree-Fock [17,18], Hartree-Fock with many-body perturbation theory [17, 19, 20], and DFT [17, 19, 21–23]. The variants of DFT methods include the linear-muffin-tin-orbital method [23], pseudopotentials [21], and the linear-combination-of-atomic-orbitals (LCAO) approach [17, 19]. Density functional calculations have employed both the local density approximation (LDA) and gradient correction methods used to improve many-body effects. These approximations are described below in chapter 3.

Results of calculations using some of the techniques mentioned above are listed in Table I. Results are taken from Suhai [19]. Here MP2 and MP4 are the second and fourth order Möller-Plesset perturbation theory methods [24]. HF is the Hartree-Fock method. The BHH procedure, developed by Becke [25], uses a gradient-corrected exchange functional with a mixture of exact HF exchange that is determined by semiempirical methods. BP86 and BLYP each use a gradient-corrected exchange functional of Becke [26] and correlation functionals developed by Perdew [27] (BP86) or by Lee, Yang, and Parr [28] (BLYP).

From these results some general conclusions can be made regarding the effects of treating explicitly the electron interactions with different approximations. Hartree-Fock calculations overestimate the dimerization, while LDA calculations tend to predict dimerization much smaller than the experimental value [19, 29]. When a gradient-corrected energy functional that incorporates the exact Hartree-Fock ex-

TABLE I: Predicted energetic and structural parameters as calculated by Suhai using different theoretical methods and a double-zeta basis set. Here r_0 is the optimal carbon-carbon distance for the nondimerized chain, $\Delta E(\text{alt-eq})$ is the energy difference between the nondimerized and dimerized structure, and Δr is the difference in bond lengths for the dimerized chain. Distances are in Å and the energy is in au/(CH unit).

Method	r_0	$\Delta E(\text{alt-eq})$	Δr
HF	1.3962	-0.00202	0.1074
BHH	1.4042	-0.00087	0.0819
BP86	1.4163	-0.00018	0.0187
BLYP	1.4189	-0.00042	0.0120
MP2	1.4250	-0.00091	0.0834
MP4	1.4290	-0.00084	0.0843

change energy is used, a dimerization close to the experimental value is obtained. The computationally expensive MP2 and MP4 methods, which also incorporate the exact exchange, also give a bond alternation close to the experimental value of about 0.08 Å [14]. These results show how the predicted structure depends highly on the details of the technique used to describe the electron-electron interactions. Inclusion of exact exchange energy appears to play an important role in producing correct dimerization values. The density functional calculations listed have been shown to give results that are sensitive to how the Brillouin zone is sampled with k points to determine the energy [29]. It has been pointed out that the small dimerization predicted by LDA may be a systematic error of LDA directly comparable to the error one obtains with SSH using a weak electron-lattice coupling parameter [30].

2.3 Soliton state in the SSH model

A quantity used to describe the extent of lattice dimerization or local changes in the bond length alternation pattern is referred to as an order parameter. A site dependent order parameter useful for investigating the soliton is given by

$$\Delta_l = 4(-1)^l \alpha u_l. \quad (11)$$

This order parameter has dimensions of energy. In the ideal dimerized ground state $\Delta_l = +\Delta_0$ (for phase A) or $\Delta_l = -\Delta_0$ (for phase B) for the entire chain. For a system with both phases coexisting on the same chain, the order parameter changes sign at the domain boundary. Su et al. [11] showed that the SSH Hamiltonian has an excited state where the order parameter does make such a transition, described by the equation

$$\Delta_l = \Delta_0 \tanh\left(\frac{la}{\xi}\right), \quad (12)$$

where ξ is the coherence length. This is given by

$$\xi = \frac{2t_0a}{\Delta_0}. \quad (13)$$

The coherence length serves as a unit of measure of the width of this geometrical phase transition (soliton). The transition occurs over a region of length 2ξ . The predicted width of the geometrical soliton depends on the exact values of the parameters used in the SSH Hamiltonian. Using parameters introduced above, the SSH model predicts $\xi = 7a$, which is in general agreement with experiment [31].

The SSH model provides some specific predictions for the electronic state associated with a soliton. Eigenfunctions of the SSH Hamiltonian can be written in terms of single-particle wave functions $\psi_{l,v}$, whose modulus squared describes the probability of finding an electron localized at the l th C-H unit for the v th eigenfunction. The midgap soliton state has an eigenfunction with the following characteristics:

$$\psi_{l=2m+1} = 0. \quad (14)$$

$$\psi_{l=2m} \sim (-1)^m \psi_0 \cosh^{-1}\left(\frac{2ma}{\xi}\right). \quad (15)$$

This form of ψ_l corresponds to a modulated spin density that vanishes on every other C-H site as seen in Fig. 5.

In the ground state of the PA system, there exists the same number of occupied states in the valence band and unoccupied states in the conduction band. This

situation is not changed when a midgap soliton state is present. When the system is neutral, a midgap soliton state will be singly occupied. The addition or removal of an electron from this highest occupied state will give a system with both a soliton and a net charge. The manner in which the charge and spin of the soliton depend on the occupation of the midgap state is pictured in Fig. 6. If there are zero or two electrons occupying the soliton state, there will be no net spin density associated with the soliton, but there will be a modulated charge density varying as ψ_l^2 .

Unlike other electronic excitations which carry both charge and spin, the soliton has a very unusual charge-spin relation. The existence of solitons with this property is thought to explain unusual experimentally observed characteristics of the PA system. For example, when PA is doped with donor impurity atoms, the conductivity increases significantly; however, the Curie paramagnetism drops. This is an effect that can be explained if the donor atoms promote population of the midgap soliton states, increasing the number of charged but spinless solitons. The above results for the soliton molecular orbital and soliton geometry have been checked with *ab initio* methods. These results, including results from the present study, will be discussed. Other predictions from the model which will be compared with results from *ab initio* calculations include the predicted formation energy and activation energy of the soliton. The activation energy, the energy required for the soliton center to move along the chain from one site to the next, is estimated to be roughly 0.002 eV/C-H unit [11] using the SSH model. This is an important quantity related to the dynamical behavior investigated here.

2.4 Experimental evidence for solitons

As discussed above, the SSH model was the first independent electron model to predict the existence of the soliton. Some brief observations on the experimental evidence for the soliton and its properties follow. Most of this information is summa-

rized in detail in the reviews by Yu [16], Kahol et al. [31], and others in this collection, as well as in the references listed in these reviews.

The existence of neutral solitons in undoped PA implies the existence of unpaired spins. Before the soliton model was established, ESR experiments were performed during the 1970's on samples of undoped PA [3,6]. The results suggest Curie paramagnetism corresponding to roughly one spin per several thousand lattice constants. Above 50 K these spins are diffusive in the direction of the polymer chains. It was difficult to explain before the soliton model why the conductivity remains negligible in the presence of mobile spins. Although the soliton model helps to explain some anomalous properties, the microscopic details of PA structure and dynamics are not well understood.

Time-resolved ESR detects both “pinned” defects and mobile defects in PA. The two types cannot be distinguished below 50 K. The pinning mechanism has been suggested to be due to the trapping of solitons by the uncontrolled presence of oxygen [32] and the presence of remnant sections of the *cis* isomer in otherwise pure (*trans*) PA [8,9].

The ESR spectrum of undoped PA has been simulated using various model Hamiltonians that predict the spin density distribution due to the soliton [31]. A given spin density distribution is used to determine the components of the hyperfine tensors needed to construct the Hamiltonian used to simulate the spectrum. The models used to determine the spin densities include the SSH model and the Peierls-Hubbard model, which is a tight-binding model like SSH that includes on-site and nearest-neighbor electron-electron interactions. It turns out that when a large number of protons are coupled to single spin, many different forms for the spin density distribution can be used to fit the ESR spectrum equally well [31]. The form of the soliton spin density distribution predicted by SSH was shown in Fig. 5. It has been determined that spin densities given by functional forms that lead to a Gaussian or even rectangular form

of the distribution fit the ESR power spectrum as well as the form predicted by SSH. ESR does not unambiguously define the spin density distribution of the soliton.

More detailed information about the soliton spin distribution can be obtained from the electron-nuclear-double-resonance (ENDOR) technique and the electron-nuclear-nuclear-triple-spin resonance technique. Experiments with these resonance techniques have confirmed the π electron character of the spin carrier in PA. The ENDOR experiments indicate a small negative spin density distribution on every other site within the soliton. These are the carbon atom sites that SSH theory predicts to have zero spin density. The negative spin densities appear to be a consequence of electron-electron interaction as they are anticipated by models and *ab initio* methods that include these interactions explicitly. Models used to fit the ENDOR spectra also seem to indicate a total spin distribution length of about 50 carbon-carbon bond lengths with a half-width of 11 carbon-carbon bonds. The spin density distribution with this width as predicted by SSH is shown in Fig. 5.

It should be noted that while the existence of the mobile soliton is supported by spin resonance experiments, there is no agreement among researchers on the value of diffusion rates for solitons along and perpendicular to the chain direction. It is known that below 30 K most solitons are trapped, whereas above this temperature the diffusion constant is proportional to the square root of temperature. The mechanism which traps solitons is not clearly understood. Furthermore, there are several difficulties involved with interpreting any experimental results. First, it is difficult to compare results from different samples made by different techniques that tend to have quite different morphologies and conjugation lengths (uninterrupted alternating bond lengths). One type of pure PA, referred to as "Durham" PA, is believed to have an average conjugation length of only 30-40 carbon-carbon bonds [33]. The densities of samples made from different methods range from 0.4 g/cm³ to 1.2 g/cm³ [3]. Furthermore, it is difficult to simulate experimental spectra using models that incorporate

electron-electron correlation. The fact that it is difficult to determine the typical abundance of defects, including *cis*-bonded regions, twisted chains, or cross-linking, complicates analysis.

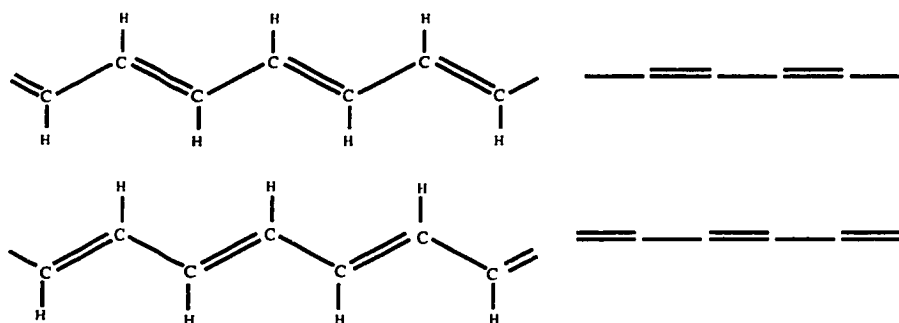


FIG. 2: Two possible configurations or "phases" of *trans*-PA. The different ordering of the single and double bonds is emphasized by the schematic representation shown at the right of each chain.

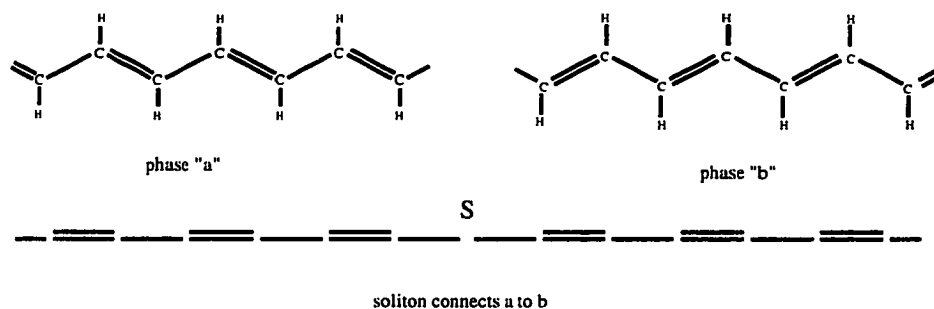


FIG. 3: The soliton kink and antikink both connect the two possible phases of bond ordering. The region where the bond ordering is interrupted is also known as a domain wall.

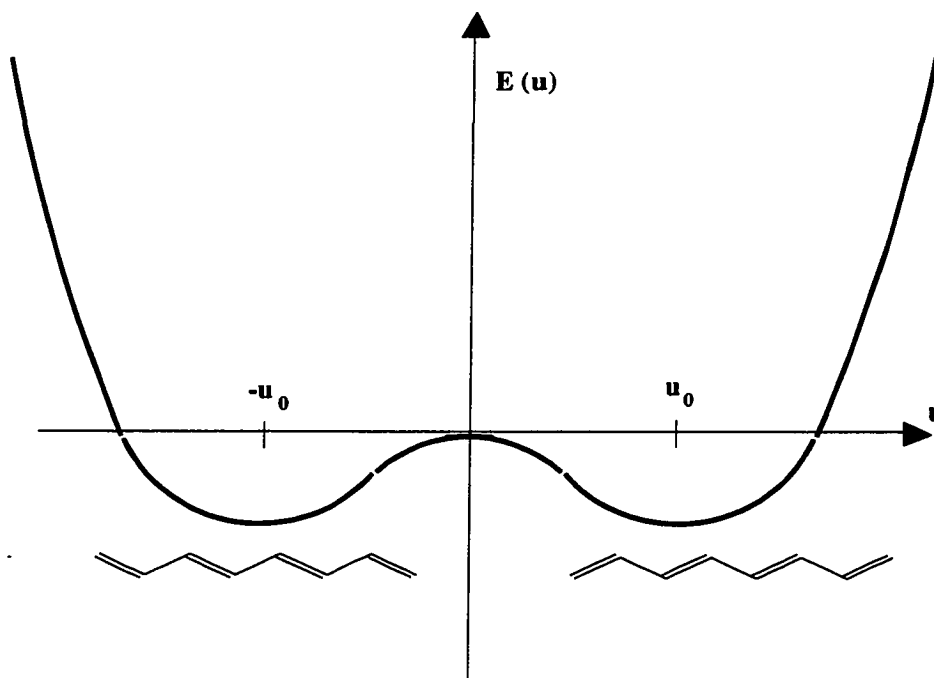


FIG. 4: Energy as a function of displacement u away from equidistant C-C bonding. The minima at $\pm u_0$ correspond to ground states with bonding order of phase A or phase B.

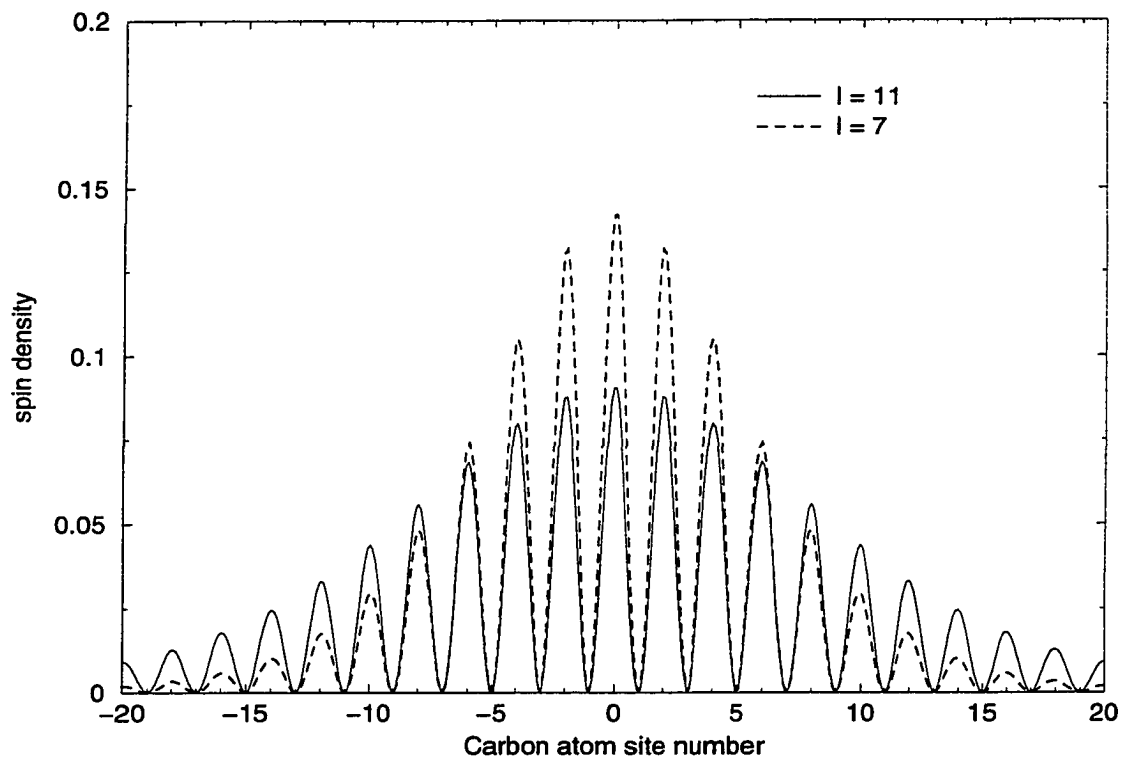


FIG. 5: Net spin density predicted from SSH model for the width parameters $l = 7$ and $l = 11$.

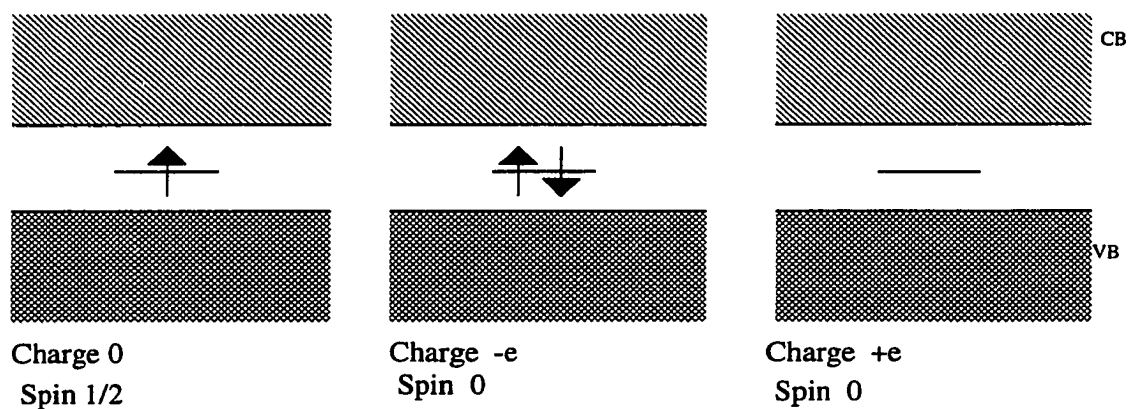


FIG. 6: Reversed spin-charge relation for neutral, negative, and positive soliton.

3 AB INITIO CALCULATION METHODOLOGY

Due to dimerization each (CH) unit is shifted about 0.02 Å from a position that would correspond to an undimerized chain. To describe such minute details of the structure accurately from a first-principles method is very challenging. Methods such as the Hartree-Fock and configuration interaction have been used to study more real-world systems with the availability of increasingly powerful computers. However, most methods such as these are still only practically applicable to systems with a few tens of atoms. DFT can be used with a total-energy pseudopotential method to model systems of a few hundred atoms from first principles. Unlike the Hartree-Fock method, both electronic exchange and correlation are taken into account. DFT has been used for both molecular and crystal systems to predict with accuracy equilibrium bond distances, phonons, and phase-transition pressures and temperatures [34, 35].

3.1 Density functional theory and the LDA approximation

DFT, like other total-energy theories, attempts to describe as precisely as possible the ground state of interacting electrons moving in a potential $v(\mathbf{r})$. The total energy of the electron system is given by the time-independent Schrödinger equation:

$$\hat{H}\Psi = E\Psi, \quad (16)$$

where Ψ is the wave function describing the system of electrons and \hat{H} is the Hamiltonian. Ψ depends on both the spin and position of each electron:

$$\Psi = \Psi(\mathbf{r}_1, \sigma_1, \mathbf{r}_2, \sigma_2 \dots). \quad (17)$$

\hat{H} can be expressed in terms of three operators:

$$\hat{H} = \hat{T} + \hat{V}_{ne} + \hat{V}_{ee}, \quad (18)$$

where \hat{T} is the kinetic energy operator, \hat{V}_{ne} is the electron-ion potential energy operator, and \hat{V}_{ee} is the electron-electron repulsion energy operator.

$$\hat{T} = \sum_{i=1}^N -\frac{1}{2} \nabla_i^2. \quad (19)$$

$$\hat{V}_{ne} = \sum_{i=1}^N v(\mathbf{r}_i). \quad (20)$$

$$\hat{V}_{ee} = \sum_{i < j}^N \frac{1}{r_{ij}}. \quad (21)$$

Based on the variational principle, the ground state Ψ_0 can be obtained by minimizing the total-energy expectation value. The total-energy E can be written in functional form:

$$E[\Psi] = \frac{\langle \Psi | \hat{H} | \Psi \rangle}{\langle \Psi | \Psi \rangle}. \quad (22)$$

Every eigenstate Ψ that satisfies Eq. (16) corresponds to a stationary point of the energy functional. Taking the variation of Eq. (22), we find

$$\delta[\langle \Psi | \hat{H} | \Psi \rangle - E \langle \Psi | \Psi \rangle] = 0. \quad (23)$$

Although it is difficult to find the exact wave function Ψ_0 that gives the lowest E satisfying Eq. (23), it is possible to find an upper bound to the true ground state energy by using the energy variational principle. When Eq. (23) is solved with an approximate solution Ψ' , a resulting energy E' will be above the ground state energy.

$$E' \geq E_0. \quad (24)$$

If one can make successively better approximations for Ψ_0 , the approximate energy E' should converge closer to E_0 from above.

Hohenberg and Kohn showed [36] that the energy E could be written as a unique functional of the electron density $\rho(\mathbf{r})$, where $\rho(\mathbf{r})$ is given in terms of Ψ by

$$\rho(\mathbf{r}_1) = N \int \dots \int |\Psi(\mathbf{r}_1, \sigma_1, \mathbf{r}_2, \sigma_2, \dots)|^2 d\sigma_1 d\mathbf{r}_2 d\sigma_2 \dots \quad (25)$$

The first Hohenberg-Kohn theorem states that the external potential $v(\mathbf{r})$ is determined within a trivial additive constant by the electron density $\rho(\mathbf{r})$. Since $\rho(\mathbf{r})$ uniquely determines $v(\mathbf{r})$, it also determines the ground state and all physical properties related to the total energy. The second Hohenberg-Kohn theorem establishes the energy variational principle in terms of $\rho(\mathbf{r})$. It states that for a trial density $\rho'(\mathbf{r})$ such that $\rho'(\mathbf{r}) > 0$ and $\int \rho'(\mathbf{r}) d\mathbf{r} = N$, the following is true for the energy functional:

$$E_0 \leq E_v[\rho']. \quad (26)$$

The fundamental energy functional can be written as follows:

$$E_v[\rho'] = \int v(\mathbf{r})\rho'(\mathbf{r})d\mathbf{r} + \frac{1}{2} \int \int \frac{\rho'(\mathbf{r})\rho'(\mathbf{r}')}{|\mathbf{r} - \mathbf{r}'|} d\mathbf{r}d\mathbf{r}' + T_s[\rho'] + E_{xc}[\rho']. \quad (27)$$

The terms on the right-hand side of Eq. (27) represent the potential energy due to the external field, the classical Coulomb energy, the kinetic energy of a non-interacting electron gas of density ρ' , and the exchange-correlation energy. The exchange-correlation is defined in terms of other functionals as follows:

$$E_{xc}[\rho] = T[\rho] - T_s[\rho] + V_{ee}[\rho] - J[\rho]. \quad (28)$$

The functional $T[\rho]$ is the energy functional for the exact kinetic energy for interacting electrons. Explicit mathematical expressions for $T[\rho]$ and V_{ee} are unknown. $J[\rho]$ is the classical Coulomb repulsion energy, which is part of the functional (27) above:

$$J[\rho] = \frac{1}{2} \int \int \frac{\rho(\mathbf{r})\rho(\mathbf{r}')}{|\mathbf{r} - \mathbf{r}'|} d\mathbf{r}d\mathbf{r}' \quad (29)$$

The functional $T_s[\rho]$ can be written down exactly for a noninteracting reference system. If a system of electrons with no electron-electron repulsion is described in terms

of a wavefunction Ψ_s , the kinetic energy $T_s[\rho]$ is given by

$$T_s[\rho] = \langle \Psi_s | \sum_{i=1}^N \frac{-1}{2} \nabla_i^2 | \Psi_s \rangle. \quad (30)$$

Since Ψ_s for the noninteracting system can be expressed as a Slater determinant of individual electron orbitals ψ_i , $T_s[\rho]$ can be further specified as

$$T_s[\rho] = \sum_{i=1}^N \langle \psi_i | \frac{-1}{2} \nabla_i^2 | \psi_i \rangle. \quad (31)$$

Kohn and Sham [37] developed a total-energy functional using single electron orbitals. These individual orbitals are determined by a self-consistent method [37]. Kohn and Sham further proposed an approximate $E_{xc}[\rho]$, taking into account only the local component of the exact exchange energy. This approximation is called the LDA. This approximation made it possible to apply DFT to realistic systems. For this dissertation, I will apply LDA to the PA system.

The significance of the Kohn-Sham energy functional relation, Eq. (27), and the computational advantages motivated by the functional are briefly outlined below. The Kohn-Sham method replaces the full interacting particle problem with a coupled single particle problem. In the Kohn-Sham picture, the density is defined by

$$\rho(\mathbf{r}) = \sum_s^N \sum_i |\psi_i(\mathbf{r}, s)|^2. \quad (32)$$

Using this definition of density, Kohn and Sham developed self-consistent equations for ψ_i . Solutions to these self-consistent equations provide the density that corresponds to the minimum of the energy functional as shown below.

The minimization of $E[\rho]$ subject to a normalization constraint on the density leads directly to the Kohn-Sham self-consistent equations. These equations provide the mathematical “machinery” for practical DFT calculations. The constraint associated with the density is specified as follows:

$$\int \rho(\mathbf{r}) d\mathbf{r} = N \quad (33)$$

The N-electron charge density which makes Eq. (27) stationary satisfies the the following Euler equation:

$$\frac{\delta T_s}{\delta \rho} + v(\mathbf{r}) + \frac{\delta J}{\delta \rho} + \frac{\delta E_{xc}}{\delta \rho} = \mu. \quad (34)$$

Here μ is a Lagrange undetermined multiplier associated with the constraint from Eq. (33). This relation is written more compactly as follows:

$$\mu = v_{eff}(\mathbf{r}) + \frac{\delta T_s}{\delta \rho}. \quad (35)$$

If the functional derivative of E_{xc} was not included with the other terms above, finding the density satisfying Eq. (35) would be accomplished by solving the self-consistent Hartree equations. Kohn and Sham proved that with the effective potential v_{eff} the density which satisfies Eq. (35) can be found with the following self-consistent single orbital equations with the same form as the simple Hartree equations:

$$[-\frac{1}{2}\nabla^2 + v_{eff}]\psi_i = \varepsilon_i\psi_i. \quad (36)$$

$$v_{eff}(\mathbf{r}) = v(\mathbf{r}) + \int \frac{\rho(\mathbf{r}')}{|\mathbf{r} - \mathbf{r}'|} d\mathbf{r}' + \frac{\delta E_{xc}}{\delta \rho}. \quad (37)$$

$$\rho(\mathbf{r}) = \sum_i^N \sum_{\sigma} |\psi_{i\sigma}(\mathbf{r})|^2. \quad (38)$$

3.2 Exchange-correlation energy functional

An expression for the exchange-correlation energy must be specified to utilize the above Kohn-Sham orbital equations. LDA provides the simplest method for this specification. LDA has been the most commonly used approximation in total-energy pseudopotential calculations. It is utilized in calculations to be described here. It is constructed by assuming the exchange-correlation energy per electron at a point \mathbf{r} in the electronic system is equal to the exchange-correlation energy per electron in a homogeneous electron gas that has the same density as the electronic system at point \mathbf{r} . Therefore, if ε_{xc} is the exchange-correlation energy per electron in a homogeneous gas of density ρ , the functional is thus specified:

$$E_{xc}[\rho(\mathbf{r})] = \int \varepsilon_{xc}[\rho(\mathbf{r})]\rho(\mathbf{r})d\mathbf{r}. \quad (39)$$

The term incorporated into v_{eff} above involving E_{xc} is known as the exchange-correlation potential. It is specified using LDA as follows:

$$\frac{\delta E_{xc}[\rho]}{\delta \rho} = \frac{\delta[\rho(\mathbf{r})\varepsilon_{xc}(\mathbf{r})]}{\delta \rho(\mathbf{r})} \quad (40)$$

This local density approximation makes the v_{eff} a local operator in the above Kohn-Sham equations. This is an important advantage over other methods such as Hartree-Fock which provide one-electron Hamiltonians with nonlocal potential operators. Self-consistent equations with nonlocal operators require considerably greater computational effort. The total electronic energy is given by the following expression:

$$E = \sum_i^N \varepsilon_i - \frac{1}{2} \int \frac{\rho(\mathbf{r})\rho(\mathbf{r}')}{|\mathbf{r} - \mathbf{r}'|} d\mathbf{r}d\mathbf{r}' + E_{xc}[\rho] - \int \frac{\delta E_{xc}[\rho(\mathbf{r})]}{\delta \rho(\mathbf{r})} d\mathbf{r}. \quad (41)$$

Several parameterizations have been developed for the exchange-correlation energy of the homogeneous electron gas ε_{xc} . The calculations discussed here use a form obtained by Vosko, Wilk, and Nusair [38]. These parameterizations use interpolation formulas to link exact results for a high-density electron gas and calculations of the ε_{xc} for intermediate and low-density electron gases.

The LDA cannot be formally justified for systems with dramatic density variations such as atoms and molecules. However, in practice LDA can be used to predict properties such as binding energy and ground state geometries with accuracy at least as good as Hartree-Fock methods. Examples of results for small molecules obtained with the LDA computer code used in this study are shown below.

Some of the polyene systems discussed below have a net spin. The use of the spin-polarized version of the Kohn-Sham equations is necessary for such systems. The spin Kohn-Sham equations allow electrons of different spins to have different spatial densities. The spin-polarized energy functional and self-consistent equations

are analogous to the above Eqs. (27), (31), and (36). These are summarized as follows [39]:

$$[-\frac{1}{2}\nabla^2 + v_{eff}[\rho_{\uparrow}, \rho_{\downarrow}]\psi_{i\sigma} = \varepsilon_{i\sigma}\psi_{i\sigma}. \quad (42)$$

$$v_{eff}(\mathbf{r}) = v(\mathbf{r}) + \int \frac{\rho(\mathbf{r}')}{|\mathbf{r} - \mathbf{r}'|} d\mathbf{r}' + \frac{\delta E_{xc}}{\delta \rho_{\sigma}}. \quad (43)$$

$$E_{xc}[\rho_{\uparrow}, \rho_{\downarrow}] = \int \varepsilon_{xc}[\rho_{\uparrow}, \rho_{\downarrow}]\rho(\mathbf{r}) d\mathbf{r}. \quad (44)$$

$$\rho_{\sigma}(\mathbf{r}) = \sum_i^{occupied} |\psi_{i\sigma}(\mathbf{r})|^2 \sigma = \uparrow, \downarrow. \quad (45)$$

$$\rho(\mathbf{r}) = \rho_{\uparrow}(\mathbf{r}) + \rho_{\downarrow}(\mathbf{r}). \quad (46)$$

The use of the homogeneous spin-polarized electron gas to specify E_{xc} in the third equation above is called the local spin density approximation (LSDA), analogous to the approximation of Eq. (39).

3.3 Basis set and energy minimization

In order to minimize the energy functional using LDA (LSDA), a basis set must first be chosen for the expansion of the orbitals ψ_i . A plane-wave basis set is used for the calculations in this study. A plane-wave basis provides a complete orthonormal basis with no system-dependent parameters. However, a plane-wave basis forces the use of periodic boundary conditions. Nonperiodic systems such as molecules require the use of periodic supercells, which are repeated over all space. Each supercell contains one molecule separated from neighboring cells with a large vacuum. For any such periodic system, Bloch's theorem states that each orbital wave function can be written as a sum of plane waves:

$$\psi_i(\mathbf{r}) = \sum_{\mathbf{G}} c_{i,\mathbf{k}+\mathbf{G}} \exp^{i(\mathbf{k}+\mathbf{G})\cdot\mathbf{r}}. \quad (47)$$

This expression is based on the existence of periodic boundary conditions for the system with reciprocal lattice vectors \mathbf{G} . The long finite polyenes considered in

this study are incorporated into a periodic system via the use of periodic supercells. Each finite polyene is centered in a cell large enough to avoid interaction with others in the lattice.

Each plane-wave with coefficient $c_{i,\mathbf{k}+\mathbf{G}}$ has a kinetic energy of magnitude $\frac{\hbar^2}{2m}|\mathbf{k} + \mathbf{G}|^2$. To perform a calculation, the infinite summation must be truncated. The truncation of the plane-wave basis occurs at a finite reciprocal vector \mathbf{G}_{max} . The accuracy of the basis is measured by the cutoff energy $E_c = \frac{\hbar^2}{2m}G_{max}^2$. A higher cutoff energy E_c provides more accurate results. The truncation always leads to some error in the computed total energy. In practice the number of plane-waves is increased until the increasing cutoff energy produces a converged result for the total energy. For the polyene calculations performed for this study, it was determined that an acceptable energy cutoff should be given by about 60 Rydbergs, which requires the use of several hundred thousand plane-waves.

The use of a plane-wave basis requires a pseudopotential approximation for the potential $v(\mathbf{r})$ for the ions and non-valence shell electrons. An extremely large number of plane-waves would be needed to expand the tightly bound core orbitals and the rapidly oscillating valence orbitals in the core region. The pseudopotential approximation allows valence wave functions to be expanded with a much smaller basis set than would otherwise be possible. This approximation removes the core electrons and replaces them and the strong ionic potential with a weaker pseudopotential. This pseudopotential acts on a set of pseudo wave functions rather than the true valence wave functions. Outside a well-defined core region, the pseudopotential and original potential are identical. An important requirement of pseudopotentials is norm conservation of wave functions. It is important to conserve the norm of wave functions in order to ensure the real and pseudo wave functions are identical outside the core region. The pseudopotential is also constructed to produce the same scattering outside the core region as that produced by the real potential. The most general

expression for a pseudopotential is

$$v_{pseudo} = \sum_{l,m} |lm\rangle V_l \langle lm|, \quad (48)$$

where $|lm\rangle$ are the spherical harmonics and V_l is the pseudopotential for angular momentum quantum number l . A pseudopotential that uses a different potential V_l for each different angular momentum component of the wave function is known as a nonlocal pseudopotential. A set of norm-conserving, nonlocal pseudopotentials developed by Hamann [40] is used here for $v(\mathbf{r})$. Bylander and Kleinman [41] suggested a separable form of the pseudopotential as follows:

$$v_{pseudo} = v_{local} + \sum_l |\xi_l\rangle \langle \xi_l|, \quad (49)$$

where the first term is a local part of the pseudopotential and second term is the completely nonlocal contribution for angular momentum l . Although a real-space expression for v_{pseudo} is complicated by this procedure, computations involving the pseudopotential are sped up considerably when performed in reciprocal space.

Although a very large number of plane-waves are required, this basis set is preferred in the present calculation for reasons other than the ease of controlling basis set size and error. The simple form of the plane-waves helps in the design of highly efficient algorithms for massively parallel computers. The form of the Hamiltonian in the Kohn-Sham equations has a particularly simple form using this basis. Substituting Eq. (48) into the eigenvalue equation, Eq. (36), gives

$$\sum_{\mathbf{G}'} \left[\frac{\hbar^2}{2m} |\mathbf{k} + \mathbf{G}|^2 \delta_{\mathbf{G}\mathbf{G}'} + v_{eff}(\mathbf{G} - \mathbf{G}') \right] c_{i,\mathbf{k}+\mathbf{G}'} = \varepsilon_i c_{i,\mathbf{k}+\mathbf{G}}. \quad (50)$$

The kinetic energy term is diagonal in the plane-wave basis, and each component of v_{eff} is expressed in terms of its discrete Fourier transform.

The total-energy functional is minimized when self-consistent solutions are obtained for the eigenvalue Eq. (50). Conventional matrix diagonalization techniques are not practical. The large number of required basis states makes storage of the entire

Hamiltonian matrix prohibitive. Furthermore, the cost of matrix diagonalization increases as the third power of the number of basis states. The formalism used for LDA energy calculations in reciprocal space is elaborated in the Appendix.

This study uses a simple iterative method to minimize the total-energy functional. For a given ionic configuration \mathbf{R}_i , this functional is given by

$$E[\psi_{i,\sigma}, \mathbf{R}_I] = \sum_{i,\sigma}^{occ} \langle \psi_{i,\sigma} | [\frac{1}{2} \nabla^2 + v(\mathbf{r}) + \frac{1}{2} \Phi(\rho) + \varepsilon_{xc}(\rho_\uparrow, \rho_\downarrow)] | \psi_{i,\sigma} \rangle + \frac{1}{2} \sum_{I \neq J} \frac{Z_I Z_J}{|\mathbf{R}_I - \mathbf{R}_J|}. \quad (51)$$

This is the same relation given above for the electronic energy functional with Φ representing the Coulomb interaction between electrons and the ion-ion repulsion energy included. It is often desirable to know the ψ_i and \mathbf{R}_i corresponding to the ground state (global minimum of E) for the system of interest. Also, given an initial non-ground-state configuration \mathbf{R}_i , we often wish to find the ψ_i which minimizes the total energy E . This second case is useful for starting subsequent molecular dynamics simulations where the trajectory of the system should be on the Born-Oppenheimer surface. In other words, the ψ_i should remain close to the instantaneous lowest-energy set for each new \mathbf{R}_i .

It is not necessary to approach the minimum of E along the Born-Oppenheimer surface. Therefore, the ψ_i and \mathbf{R}_i can be treated as independent degrees of freedom. The method of steepest descent minimization used in this study takes this approach and provides a simple algorithm for obtaining the nearest minimum starting from an initial set of ψ_i and \mathbf{R}_i . Only first-order derivatives of the energy functional are required with this method. A generalized force for the electronic orbitals is defined as follows:

$$f_{i,\sigma} = -\frac{\delta E}{\delta \psi_{i,\sigma}^*} + \sum_j \Lambda_{ij} \psi_{j,\sigma}, \quad (52)$$

where the second term on the right-hand side ensures that the wave functions satisfy the orthonormal constraint using a Lagrangian multiplier matrix Λ_{ij} . The first “force”

term is expressed as the following:

$$-H\psi_i = -\frac{\delta E}{\delta\psi_{i,\sigma}^*}, \quad (53)$$

where H is the one-electron Hamiltonian of the Kohn-Sham equations. The force $(-H\psi_i)$ is the gradient of the Kohn-Sham energy functional at the point in Hilbert space corresponding to the wave function ψ_i . The force on the ions is given by

$$F_I = -\nabla_I E. \quad (54)$$

Given these force equations, the system converges towards a minimum according to the following finite difference equations;

$$\psi_{i\sigma}^{n+1} = \psi_{i\sigma}^n + \xi f_{i\sigma} \quad (55)$$

$$\mathbf{R}_I^{n+1} = \mathbf{R}_I^n + \eta F_I \quad (56)$$

where the parameters ξ and η control step lengths.

3.4 Testing the implementation of the plane-wave LDA/LSDA method

We tested our implementation of the method by calculating systems of small molecules containing carbon and hydrogen. The results are shown in Table II under the column LDA-PW. For comparison other ab initio results obtained by Johnson, Gill, and Pople [42] are also shown. Molecular geometries generally agree with experiment with errors less than a few percent. Therefore, we believe it is appropriate to use this method for PA.

3.5 Gradient corrections to the local density approximation

Including the lowest-order gradient correction, the exchange-correlation energy $E_{xc}[\rho]$ has the form

$$E_{xc}[\rho(\mathbf{r})] = \int \varepsilon_{xc}[\rho(\mathbf{r})]\rho(\mathbf{r})d\mathbf{r} + \int \Gamma_{xc}(\rho(\mathbf{r}))|\nabla\rho(\mathbf{r})|^2d\mathbf{r}. \quad (57)$$

TABLE II: Theoretical and experimental geometries. Bond distances in angstroms and bond angles in degrees. Theoretical values from Johnson et al. were obtained using 6-31G* basis set (except plane-wave calculations).

Molecule	Param.	S-VWN	B-LYP	HF	MP2	QCISD	LDA-PW	Expt
CH	R_{C-H}	1.152	1.146	1.108	1.120	1.131	1.130	1.120
CH ₃	R_{C-H}	1.093	1.090	1.073	1.078	1.083	1.075	1.079
CH ₄	R_{C-H}	1.101	1.100	1.084	1.090	1.094	1.084	1.086
HCCH	R_{C-C}	1.212	1.215	1.185	1.216	1.211	1.189	1.203
	R_{C-H}	1.078	1.073	1.057	1.066	1.069	1.061	1.061
H ₂ CCH ₂	R_{C-C}	1.331	1.341	1.317	1.335	1.337	1.310	1.339
	R_{C-H}	1.098	1.095	1.076	1.085	1.088	1.081	1.085
H ₃ CCH ₃	$\theta(\text{HCH})$	116.4	116.2	116.4	116.6	116.3	116.5	117.8
	R_{C-C}	1.513	1.541	1.527	1.524	1.528	1.501	1.526
	R_{C-H}	1.105	1.104	1.086	1.093	1.097	1.089	1.088
	$\theta(\text{HCH})$	107.2	107.5	107.7	107.7	107.7	107.2	107.4
O ₂	R_{O-O}	1.215	1.240	1.168	1.246	1.221	1.206	1.207
N ₂	R_{N-N}	1.122	1.118	1.078	1.130	1.114	1.089	1.098
NO	R_{N-O}	1.161	1.176	1.127	1.143	1.174	1.143	1.151
BeH	R_{Be-H}	1.370	1.355	1.348	1.348	1.357	1.343	1.343

It is difficult to find a form for $\Gamma_{xc}(\rho(\mathbf{r}))$ which recovers the exact known result of E_{xc} for the uniform homogeneous electron gas [43]. Furthermore, gradient-corrected schemes often produce exchange-correlation potentials with unphysical asymptotic behavior close to the atomic nucleus or in the tail of the electron distribution of finite systems [44]. Furthermore, pseudopotentials generated with most gradient-correction schemes tend to have strong oscillations and other irregularities inside the core region, which limits their practicality [45].

Recent attempts to find an improved gradient-corrected functional separate the exchange-correlation energy into separate exchange and correlation contributions. One such widely tested method employs a gradient-corrected exchange functional proposed by Becke [26] and a gradient-corrected correlation energy functional proposed by Perdew [27]. This corresponds to the method listed as BP86 in Table I. I implemented this approximation in my plane-wave density functional code. To construct pseudopotentials with these gradient-corrected formulas, I followed closely the

prescription given by Hamann [40]. Our generated pseudopotentials match those generated by Ortiz and Ballone [45]. Our calculations testing bond lengths and cohesive energies of small molecules matched results reported in Ref. [45].

As will be shown in chapter 4, the inclusion of this gradient correction does not improve the agreement of our predicted dimerization (for the infinite PA system) with experiment. Suhai [19] also found that only gradient-corrected methods that include some mixing of exact exchange energy improve LSDA predictions for PA. Gradient-correction schemes are known to often fail to improve predictions for equilibrium lattice constants in extended systems even while they generally improve structural predictions for molecules [46].

3.6 Molecular dynamics methodology

The Car-Parrinello molecular dynamics method is used here for dynamical simulations of solitons in PA. Again, as in the steepest descent algorithm, the $\psi_{i\sigma}$ and the \mathbf{R}_I are treated as independent degrees of freedom. Car and Parrinello proposed the following Lagrangian with the electronic orbitals treated as dynamical variables [47]:

$$L = \sum_{i\sigma} \mu \langle \dot{\psi}_{i\sigma} | \dot{\psi}_{i\sigma} \rangle + \frac{1}{2} M_I \dot{\mathbf{R}}_I^2 - E[\psi_{i\sigma} \mathbf{R}_I]. \quad (58)$$

Here, μ is a fictitious mass associated with the electronic orbitals and M_I is the ionic mass. The wave functions are subject to the orthonormal constraint for all times.

$$\langle \psi_{i\sigma}(t) | \psi_{j\sigma}(t) \rangle = \delta_{ij}. \quad (59)$$

The resulting equations of motion are expressed as

$$\mu \ddot{\psi}_{i\sigma} = -H \psi_{i\sigma} + \sum_j \epsilon_{ij} \psi_{j\sigma} \quad (60)$$

$$M_I \ddot{\mathbf{R}}_I = -\nabla_I E \quad (61)$$

The $\epsilon_{i\sigma}$ is a Lagrange multiplier to hold the orthogonality of Eq. (59). The conserved quantity includes the sum of two classical mechanical kinetic energies as given by

$$E_{total} = K_I + K_E + E_{LDA} \quad (62)$$

$$K_I = \frac{1}{2} M_I \dot{\mathbf{R}}_I^2 \quad (63)$$

$$K_e = \mu \sum_{i,\sigma} \langle \dot{\psi}_{i\sigma} | \dot{\psi}_{i\sigma} \rangle, \quad (64)$$

where E_{LDA} is given by the value of the LDA energy functional. This E_{total} is monitored as the dynamics evolve as a check against calculation errors.

The equations of motion above are solved using a standard finite difference technique known as Verlet's algorithm [48]. It gives the value of the i_{th} electronic state after a consecutive time step Δt as

$$\psi_{i\sigma}(\Delta t) = 2\psi_{i\sigma}(0) - \psi_{i\sigma}(-\Delta t) + \Delta t^2 \ddot{\psi}_i(0), \quad (65)$$

where Δt is the time step, $\psi_{i\sigma}$ is the value of the state at the present time step, and $\psi_{i\sigma}(-\Delta t)$ is the value of the state at the previous time step. Substitution of Eq. (60) into Eq. (65) gives

$$\psi_{i\sigma}(\Delta t) = 2\psi_{i\sigma}(0) - \frac{\Delta t^2}{\mu} [H\psi_{i\sigma} - \sum_j \epsilon_{ij} \psi_{j\sigma}(0)]. \quad (66)$$

The Verlet algorithm introduces an error of order Δt^4 into the integration of the equations of motion.

The Car-Parrinello algorithm offers computational advantage over other methods used to observe the trajectory of a system on the Born-Oppenheimer surface. The electronic wave functions “move” with velocities in such a manner that they remain very close to the instantaneous ground state wave functions for the ionic configuration at each time step. It is not necessary to diagonalize and store the entire Hamiltonian matrix. Instead, it is necessary to store only the wave functions operated on by the Hamiltonian in the form of their expansion coefficients. Updating the wave functions

for a new time step requires the storage of the wave functions for the current and previous time steps, as evident from Eq. (66). For the dynamics studies described here, $\mu = 300m_e$ and the time step $\Delta t = 1$ au (≈ 0.024 fs).

4 RESULTS OF AB INITIO CALCULATIONS OF MODEL PA

We have investigated the infinite PA system with periodic boundary conditions using the method described above in section 3. Since the supercell used must be finite, we have a finite number of reciprocal lattice vectors (k points) for use in these total-energy calculations. The results for the predicted bond alternation using different numbers of atoms in increasingly larger supercells are shown in Table III. Calculations listed using a generalized gradient correction use functionals proposed by Becke [26] and Perdew [27] and are implemented with a pseudopotential method as described by Ortiz and Ballone [45]. The computer code for generating pseudopotentials developed by Hamann [49] was modified to include the gradient correction. Again, as discussed above, this particular gradient-correction scheme has not given an improvement for predicted dimerization.

TABLE III: Bond alternation as predicted by LDA with and without generalized gradient correction. $\Delta_{exp} \approx 0.08 - 0.1 \text{ \AA}$

Unit cell	R_{C-C}	$R_{C=C}$	$\Delta \text{ (\AA)}$
C_8H_8	1.46	1.34	0.12
C_8H_8 GGC	1.46	1.33	0.13
$C_{16}H_{16}$	1.42	1.35	0.07
$C_{16}H_{16}$ GGC	1.43	1.36	0.07
$C_{32}H_{32}$	1.41	1.35	0.06
$C_{32}H_{32}$ GGC	1.42	1.37	0.05

In agreement with previous studies [19, 29], I find that the dimerization decreases as the number of k points used for the calculation increases. This result was also confirmed by Bylaska [50] in an extensive study of carbon chain systems using this method. For an infinitely large unit cell size, I expect that my predicted dimer-

ization will be considerably smaller than experiment. Therefore, based on my own and other previous results, I conclude that LDA/LSDA or the gradient-correction method I have tested to this date is not appropriate for describing the dimerization of the infinite PA system. This is one reason I use finite polyene chains in this study to model the infinite PA system.

I investigate polyenes of the form C_nH_{n+2} for even and odd values of n up to $n = 33$. The end of a polyene chain forces dimerization. The final carbon-carbon bond is forced to be a double (short) bond by the presence of the extra terminating hydrogen atom. I refer to polyenes where n is an even(odd) integer as an even(odd)-membered polyene. As discussed below, it is possible to have only one phase of bond ordering in an even-membered polyene. However, odd-membered polyenes must have at least two phases present. The ground state of an odd-membered polyene is a soliton state.

4.1 Results for even-membered polyenes

The tendency of LDA to underestimate dimerization was discussed above. For calculations for the idealized infinite system, LDA calculations typically give a small dimerization that is 10% of the experimental value. Results from the LDA plane-wave basis method used here were tested for systems with as many as 32 carbon atoms in the unit cell (see Table III). While the difference in long and short bond lengths ($r_{C-C} - r_{C=C} = 0.06\text{\AA}$) is smaller than the experimental value of 0.08\AA [14], the value is reasonably close. Using larger unit cell sizes should gradually lead to smaller and negligible dimerization according to other previous results [19, 29].

Calculations were performed for this study on even-membered polyenes of pristine *trans*-PA to check how the predicted structure changes with increasing chain size. The results performed with the LDA plane-wave technique are listed in Table IV with the label LDA-PW. For comparison results of other ab initio methods [17, 51] are also included. These other calculations use techniques including second-order

TABLE IV: Predicted lengths of short/long central bonds in even-membered polyene systems. All calculations (except LDA-PW) used a 6-31G* basis set except results shown for B-LYP^d, which used a 6-31G** basis.

Method	$C_{10}H_{12}$	$C_{18}H_{20}$	$C_{30}H_{32}$	$C_{32}H_{34}$	∞ limit
HF ^a	1.332/1.459				1.325/1.462
MP2 ^b	1.360/1.440				1.373/1.423
B-LYP ^c	1.326/1.439	1.384/1.428	1.390/1.422		1.398/1.413
B-LYP ^d	1.376/1.438				1.398/1.417
B3-LYP ^c	1.360/1.438	1.366/1.430	1.368/1.426		
LDA-PW		1.360/1.410		1.360/1.400	1.351/1.410
exp. ^e					1.36/1.44
(a) Ref. [53]					
(b) Ref. [54]					
(c) Ref. [17]					
(d) Ref. [17]					
(e) Ref. [14]					

Möller-Plesset (MP2) and gradient-corrected LDA. These calculations are performed with different exchange functionals given by Becke [25, 26] (labeled by B and B3) and correlation functionals given by Lee, Yang and Parr [52] (labeled by LYP). The details of the methods are found in the references. The table gives calculated bond lengths for the long and short bonds near the center of each polyene. A schematic picture of an even-membered all-*trans* polyene is shown in Fig. 7. Figure 8 plots the bond length of each carbon-carbon bond from end to end for $C_{32}H_{34}$ as calculated by LDA-PW. The bond alternation is very uniform except near the ends, where the dimerization is accentuated by the terminal atoms. The highest occupied molecular orbital (HOMO) level contour plot shows the paired π electron bonding in the central section of the polyene that is expected to be characteristic of the ideal infinite chain.

In contrast to the infinite PA system, the finite even-membered polyene has a unique ground state. There are not two “phases” of bond ordering that give the same energy. This is obviously due to the effect of the chain ends. The total energy is lowest when the terminal carbon-carbon bonds are short instead of long. The electronic environment and lattice coupling should be similar to that for the ideally

electronic environment and lattice coupling should be similar to that for the ideally infinite chain with the degenerate ground state when the soliton is not too close to the chain ends. The study of the interaction of the soliton with a chain end is important since real solitons must, of course, exist on finite chains.

Density functional calculations tend to underestimate the dimerization in the infinite chain limit by at least 40%. However, for finite chains the dimerization appears to be rather independent of chain size and close to what is predicted with each method for the infinite chain limit. The B-LYP dimerization result is significantly reduced in the infinite limit; however, as discussed above, the value for the infinite chain is extremely sensitive to how the Brillouin zone is sampled. Although the experimental difference in r_{C-C} and $r_{C=C}$ is extremely small and sensitive to the specifics of how electron exchange and correlation are treated, different methods are seen to give very similar results. Although the dimerization in the long polyenes is found from these calculations to be roughly half of the experimental value, it is qualitatively correct. It will be assumed in the following analysis that LDA provides at least a good qualitative description of the electronic and lattice coupling that is important for studying soliton dynamics. This assumption is based on the above results and on the well known fact that density functional methods have been successfully used to predict with accuracy vibrational frequencies, bulk moduli, lattice constants, and other properties for a large variety of chemical systems. This general accuracy of LDA is discussed in detail in the reviews [39, 43].

4.2 Polyenes with a *cis* bond defect

As mentioned above, *trans*-PA is the lowest-energy and most thermally stable isomer of PA. Films of *trans*-PA are made from as-grown films of *cis*-PA by heating the film above 100° C. Experiments indicate that isomerization is not totally complete. Infrared absorption experiments indicate that residual *cis* segments are an important

defect at a typical estimated level of 5% [8]. In the real material a mobile soliton is likely to encounter such a defect, which is likely to impose an energy barrier. It has been suggested that solitons in *trans* regions of the chain may be trapped by bounding *cis* regions at low temperatures [8,9]. It is well known that a small number of neutral solitons are localized (trapped) within short *trans* segments in PA that is mostly *cis*-PA [55]. Several researchers have used a model of PA that includes temperature-dependent trapping probabilities to explain data from ESR and dynamical nuclear polarization experiments [31,32,55,56]. Results of these experiments generally imply that below 10 K there is no soliton diffusion, and between 10 K and 150 K trapped solitons gradually become mobile. Besides oxygen impurities adsorbed on sample surfaces and residual catalyst atoms, the presence of *cis* bonds may be an important source of soliton trapping.

There are two possible configurations of *cis*-PA as shown in Fig. 9. The *cis*-transoid is the only experimentally detected isomer and is closer to the lowest-energy *trans*-PA by about $0.05\text{eV}/(C_2H_2)$ according to *ab initio* calculations [57,58]. The *trans*-cisoid form is suspected to be a meta-stable form of PA as there is no detected local energy minimum in calculations where the bond order is gradually changed from the *cis*-transoid to the *trans*-cisoid configurations [57].

Calculations to determine the static properties of polyenes with one or two *cis* bond defects on an otherwise *trans* chain were performed for this study. It is useful to have some information on how the energy and bond order structure changes in the system before trying to simulate mobile solitons in the defect system. An even-membered polyene with a *cis* bond in the center is shown schematically in Fig. 10. It is expected that inclusion of a *cis* bond should not affect the general alternating bond length pattern for even-membered polyenes.. A central *cis* bond should be long if there are $4N$ carbon atoms and short if there are $4N - 2$. It is also expected that the lowest-energy configuration for the polyene structure should be a bent “boomerang”

angles between any three carbon bonds equal to about 125° [57,59]. It is interesting to note that a single *cis* bond geometrically separates the two possible “phases” or bond ordering of *trans*-PA like the soliton does. However, unlike the soliton there is no interruption or mismatch in the regular short-long bond alternation, which is a defining characteristic of a soliton.

The results of some calculations for the small system $C_{10}H_{12}$ are shown in Fig. 10. The “bent” structure with the middle *cis* bond is lower in energy, as expected, than the corresponding straight structure by 0.71 eV. When the geometry is allowed to relax, the straight system does not move towards the bent configuration. The average bond length is slightly larger for the straight structure, especially around the *cis* structure, where the lattice strain would intuitively be the largest. This strain energy is apparently more significant than the energy change created by moving the *cis* to another position along the chain while keeping the C-C-C bond angles $\approx 125^\circ$. As shown in Fig. 10 the energy was minimized with the *cis* bond at the end of the polyene instead of the middle. The *cis* bond is long in this case and corresponds to the trans-cisoid isomer of *cis*-PA shown above, which again has not been experimentally detected as a physically existing isomer. The difference in energy from the “bent” structure with the *cis* bond in the middle is smaller in this case, suggesting that retaining the energetically favorable 125° bond angles may be more important than exact position or type of *cis* bond when considering small energy differences.

Figure 11 shows similar results for bond lengths of $C_{18}H_{20}$ when the pure *trans* form of the polyene is compared to the same system with one *cis* bond in both the bent and straight chain geometries. The pure *trans* form is 0.024 eV lower in energy than the bent *cis* form. The *trans* form is lower than the straight chain with one *cis* by 0.90 eV and lower than a chain with two *cis* bonds in the middle by 1.44 eV. It appears that the presence of each *cis* bond in the straight polyene chain raises the energy on the order of $0.1\text{eV}/(C_2H_2 \text{ unit})$. These differences are of the same order of

energy on the order of $0.1\text{eV}/(\text{C}_2\text{H}_2 \text{ unit})$. These differences are of the same order of magnitude as the predicted difference between the infinite pure isomers (per C_2H_2) shown in Fig. 9. A single *cis* bond in a straight chain causes increase in bond length around the *cis* bond as seen in Fig. 11. The bond lengths shown for the bent structure are almost identical to the *trans* form. It is reasonable to infer that the increase in energy for the straight *cis* system comes from the distortion or strain caused by the *cis* region where the C-C-C bond angles are away from 125° . The C-C-C bond angle for the section connecting the *cis* bond to the *trans* chain is $\approx 150^\circ$ when the chain with one *cis* bond is straight.

We are interested in the energy barrier encountered by a mobile soliton caused by a single *cis* bond. Since the geometrical defect is expected to be distributed over roughly 15 carbon bonds, there must be a collective motion of all these C-H units to produce the motion depicted. However, each unit must only shift a very small amount as the soliton passes and changes one degenerate bonding phase to the other possible phase. The only estimate made to date for the energy required to promote the soliton center from one site to the next has been by Su et al. [11]. They estimated this activation energy with the SSH model to be $\approx 0.002 \text{ eV}$. However, it seems clear that the changes in bond length ordering seen around the *cis* region may change the activation energy required near the central *cis* bond. Furthermore, as the soliton passes over the *cis* bond, it is changing the bond from one possible type of *cis* structure to the other. However, as indicated above for finite even polyenes, the two forms or “phases” of *cis* bonds will not be energetically equivalent for a given finite chain. Therefore, the soliton should lose (or gain) some kinetic energy as the *cis* bond is transformed from one form to another, if indeed the soliton has enough kinetic energy to pass over the *cis* region. These ideas are discussed further in light of results of molecular dynamics simulations for a soliton colliding with a *cis* region described in chapter 6.

4.3 Odd-membered polyenes of *trans*-PA: Static calculations

Total-energy calculations for polyenes similar to those discussed above were performed to investigate properties of a static soliton. Like the polyenes above, these odd-membered polyenes have terminal carbon-carbon bond lengths that are shorter than the others. Figure 12 shows the calculated bond lengths of polyenes of various charge species with 17 and 33 carbon atoms. The bond lengths alternate between the ends and the polyene center. It is impossible for the short-long alternation pattern to proceed uninterrupted from one end to the other if the bond length pattern is symmetric about the polyene center. Figure 12 shows the symmetry is preserved with a topological “kink” or phase change in the bonding order characteristic of the soliton. An important quantity characterizing the soliton is the geometric width. This is the length of the chain segment over which the bond alternation changes from one phase to another. The changing bond alternation is usually described by the bond order parameter. The bond order parameter Φ_n introduced in section 2.1 was given in terms of the shift distance u_n of each of the carbon atoms away from a position that would correspond to an undimerized chain. The bond order parameter can also be discussed in terms of the length difference between adjacent bonds. The order parameter is then given by Δr_n , which is specified as follows:

$$\Delta r_n = -1^n[(\mathbf{r}_{n+1} - \mathbf{r}_n) - (\mathbf{r}_n - \mathbf{r}_{n-1})]. \quad (67)$$

Here Δr_n describes the difference in nearest-neighbor bond lengths with respect to a carbon atom labeled by integer n . The \mathbf{r}_n specifies the position of the n_{th} carbon atom site. For the ideal infinite PA system with no excitations or defects, Δr_n is equal to a constant $\pm\Delta r_\infty$ due to the uniform dimerization with the two possible “phases” of bond ordering. The bond alternation for the PA system with a soliton is predicted by the SSH model to have the form

$$\Delta r_n = -1^n \Delta r_\infty \tanh\left(\frac{n - n_0}{l}\right). \quad (68)$$

Here the integer n again labels each carbon atom on a chain with a soliton distortion centered about carbon atom n_0 . The factor -1^n gets rid of the oscillating sign of the bond length differences so that when $n - n_0 \gg l$ the order parameter $\Delta r_n = \pm \Delta r_\infty$. The total geometrical width of the soliton is $2l$ carbon-carbon bond lengths. This is the width of the segment over which the bond order changes from $-\Delta r_\infty$ to $+\Delta r_\infty$ or vice versa.

The bond alternation Δr_n for $C_{33}H_{35}^-$ and $C_{17}H_{19}$ obtained from our LDA code is shown in Fig. 13. Also shown is the bond order predicted from the SSH model using the $l = 10$ for the soliton half-width. While the experimental soliton width is uncertain, it has been reported that $l = 11$ generates a best fit for models used to simulate ENDOR spectra [31, 60]. Most SSH calculations use $l = 7$ since the use of this value leads to reasonable results for quantities like the bandwidth which have experimental values which are easier to measure.

From the figures it is apparent that SSH predicts an essentially complete transition over a length of about 22 carbon bonds, whereas the transition for the LDA predicted structure is more gradual and encompasses the whole chain. The shape of the tanh function does not seem to fit the LDA results very well. A common feature of both Hartree-Fock and LDA structures is that the bond length of the terminal carbon bonds is practically independent of system size. The environment around the terminal carbon atoms seems to fix Δr for the ends, and the bond alternation is greater than the experimental value of 0.08 Å near the ends. The curve for $C_{17}H_{19}$ is especially steep since the change in bond alternation pattern takes place over a segment half as large as that available in the larger system. Charged polyenes with up to 37 carbon atoms have been studied previously by Champagne, Deumens, and Ohrn [61] using Hartree-Fock self-consistent field calculations. The Hartree-Fock results better reflect the SSH tanh function shape for the alternation, although the best fit is for the relatively small half-width value of $l = 5.7$.

The bond alternation data show that far from the kink center the bond alternation is greater than the experimental value for Δr_∞ for the Hartree-Fock results and smaller for the LDA case. These results mirror the tendencies of these methods to overestimate (Hartree-Fock) and underestimate (LDA) the dimerization when the infinite system is considered. These results can be interpreted in terms of the SSH model. The SSH model gives us the following relations among the band gap (Δ_0), the valence bandwidth ($4t_0$), the electron-phonon coupling constant (α), and the soliton width l .

$$\Delta_0 = 4\alpha u_0 \quad (69)$$

$$l = \frac{t_0 a}{2\alpha u_0} \quad (70)$$

Here a is the unit cell length and u_0 is given by $\Delta r_\infty/4$. Kawai et al. [30] have shown that LDA results for carbon rings correspond to SSH results with a weak coupling constant α , while Hartree-Fock results map to a strong coupling constant. They also show that weak coupling leads to small dimerization and strong coupling leads to large dimerization. The very large width l of the distortion shown above is supported by Eq. (70) if LDA results correspond to SSH results with small α in finite as well as periodic systems.

In chapter 2 the modulated form of the soliton wave function was given in Eq. (15) as predicted by SSH. The density (charge or spin) is described by SSH by the relation

$$\rho_j = (1/l) \text{sech}^2(j/l) \cos^2(j\pi/2). \quad (71)$$

Clearly, the width of the electronic density associated with the soliton is expected to be much greater than its geometric width. From Fig. 5 above we see that a soliton with a geometric half-width of $l = 7$ is still at about half of its maximum amplitude at a distance of 7 carbon bond lengths from the soliton center. Figure 14 shows the spin polarization density ($\rho_\uparrow - \rho_\downarrow$) along a line parallel to the axis of neutral $C_{33}H_{35}$

and 1.4 au above the plane of the polyene, as calculated from our LDA computer code. This happens to be a soliton in motion, the density taken from a molecular dynamics time step when the soliton is near the center of the chain. The dynamics will be discussed in detail below. The very diffuse nature of the soliton as predicted by the LDA is again evident. Unlike the SSH density which is exactly zero on every other carbon site, the soliton density of Fig. 14 shows the density to be slightly negative there. This small negative density has been observed by triple resonance experiments (triple-ENDOR) [31,60]. This effect has also been anticipated by models such as the Peierls-Hubbard model [62,63] and ab initio studies [18,61,64] where electron-electron correlation is explicitly taken into account.

It is difficult to make detailed comparisons between the soliton nature shown here and that of other studies and experiments. This is due to the large uncertainties of the experimental data and the dependence of typical model calculations based on unknown guessed parameters. These static calculations show clearly that a soliton structure is located at the center of the chain in odd-membered polyenes of the *trans* form. In the idealized infinite chain, the soliton is expected to move anywhere along the chain with essentially no change in total energy of the system since each unit cell is equivalent. The dynamics simulations described in following sections confirm that a soliton distortion near an end of a finite chain is energetically unfavorable. The finite chain system provides a potential well, and it will be shown that as the soliton moves toward a chain end, the ionic kinetic energy decreases while the total potential energy (including electronic energy) increases. Although the soliton width described by LDA appears to be greater than that described by other methods such as Hartree-Fock, I expect that the energy difference calculated as the soliton center moves from site to site should be well described by molecular dynamics calculations using either method. As will be described, I am particularly interested in the change of the potential energy caused by the presence of a single *cis*-bond defect. This defect has a geometric

width of a few carbon-carbon bond lengths. The new qualitative information about the soliton-defect interaction given by LDA and molecular dynamics simulations is discussed below.

4.4 Odd-membered *trans* polyenes with one *cis* bond

The results above confirm that a soliton state exists as the ground state of odd-membered polyenes of the *trans*-PA form. Our density functional code was also used to find the ground state structure of the same odd-membered polyenes with one *cis* type bond near the center. Figure 15 shows the calculated carbon-carbon bond lengths and spin-polarization density for the polyene $C_{31}H_{33}$ with one *cis* bond. The system lacks the C_{2v} symmetry about the central carbon atom that exists for the all-*trans* odd-membered polyene. We find that the symmetry breaking introduced by the *cis* bond leads to a ground state without the existence of a soliton. In Fig. 15 the calculated bond lengths and spin-polarization density are shown. The spin-polarization density is concentrated on every other carbon atom site. However, unlike the soliton density there is a visibly greater concentration on one side of the *cis* bond over half of the polyene length. The bond length distribution also lacks symmetry about the central carbon atom. The bond ordering changes from one “phase” of bond ordering to the other in the central part of the polyene. This again satisfies the topological constraints imposed by the short bonds at the ends. The transition from one bond ordering to the other does not have the smooth, gradual character expected of a soliton.

While it is energetically favorable for a soliton to be located at the center of an odd-membered all-*trans* polyene, the ground state for the case with a *cis* bond gives no such indication. Dynamical simulations described below involve both a central *cis* bond and a soliton on the same odd-membered polyene chain. Before performing the full dynamics simulation, we need to “create” an initial excited state

of the polyene that leads to soliton-*cis* bond interaction. The initial geometries and ensuing dynamics are discussed below.

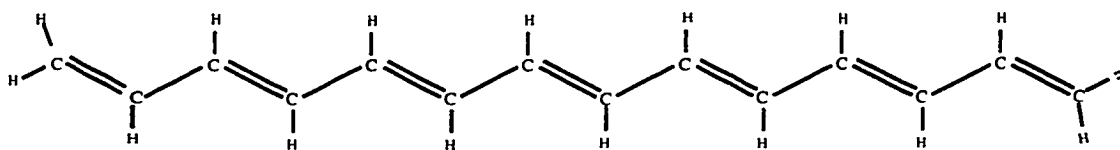


FIG. 7: Example of an all-*trans* C_nH_{n+2} polyene. Here $n = 14$.

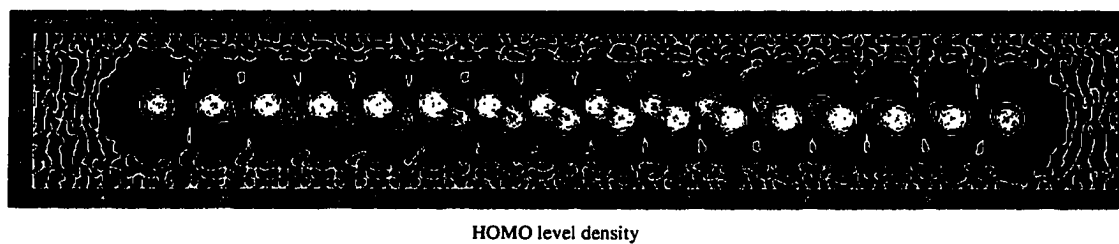
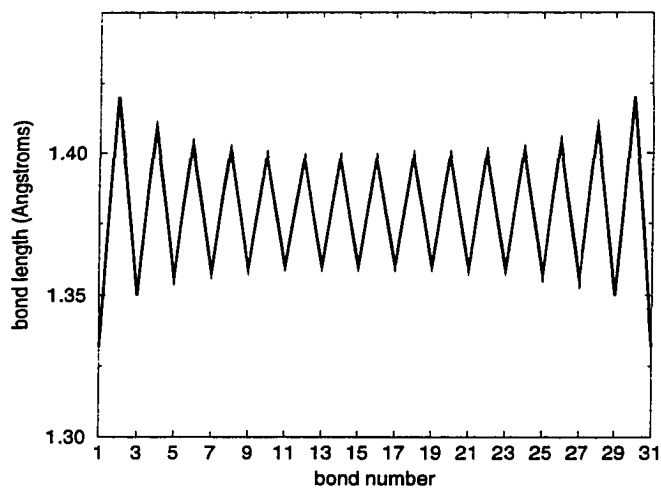
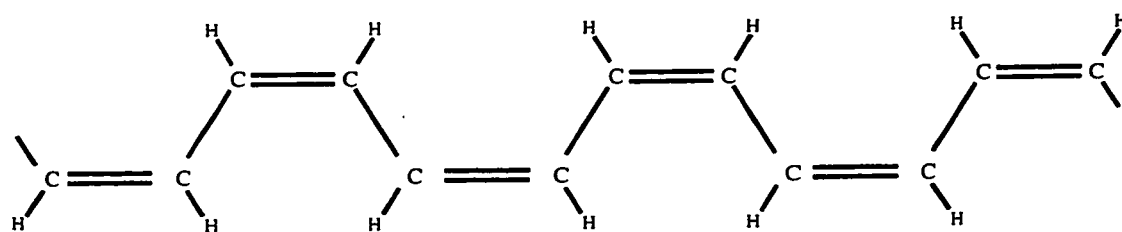
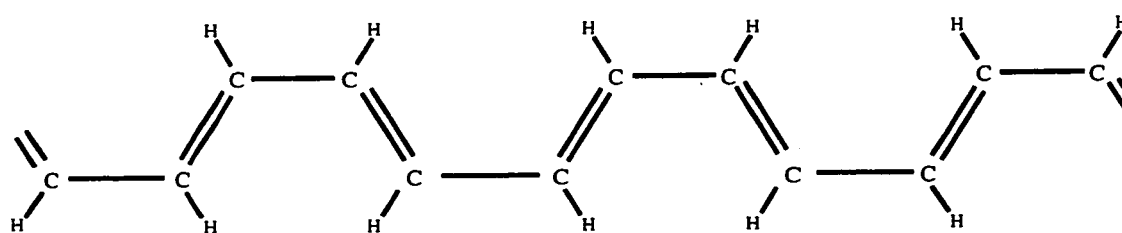


FIG. 8: Carbon-carbon bond lengths and HOMO density 1 au above the polyene plane for $C_{32}H_{34}$.



cis-transoid PA (*cis*- PA)



trans-cisoid PA

FIG. 9: The two possible isomers of all-*cis*-PA.

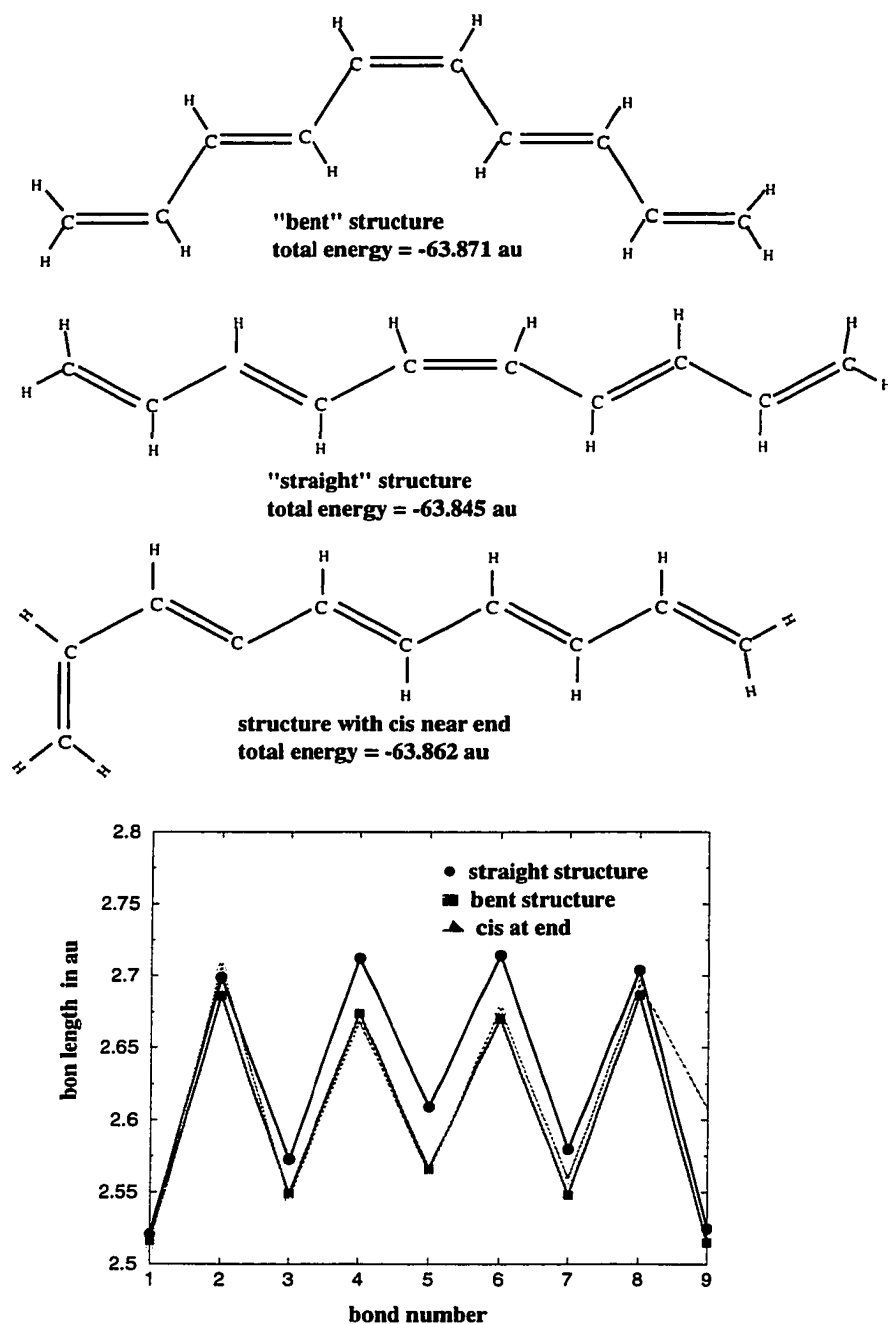


FIG. 10: Structure, total energy, and calculated bond lengths for $C_{10}H_{12}$ with one *cis* bond.

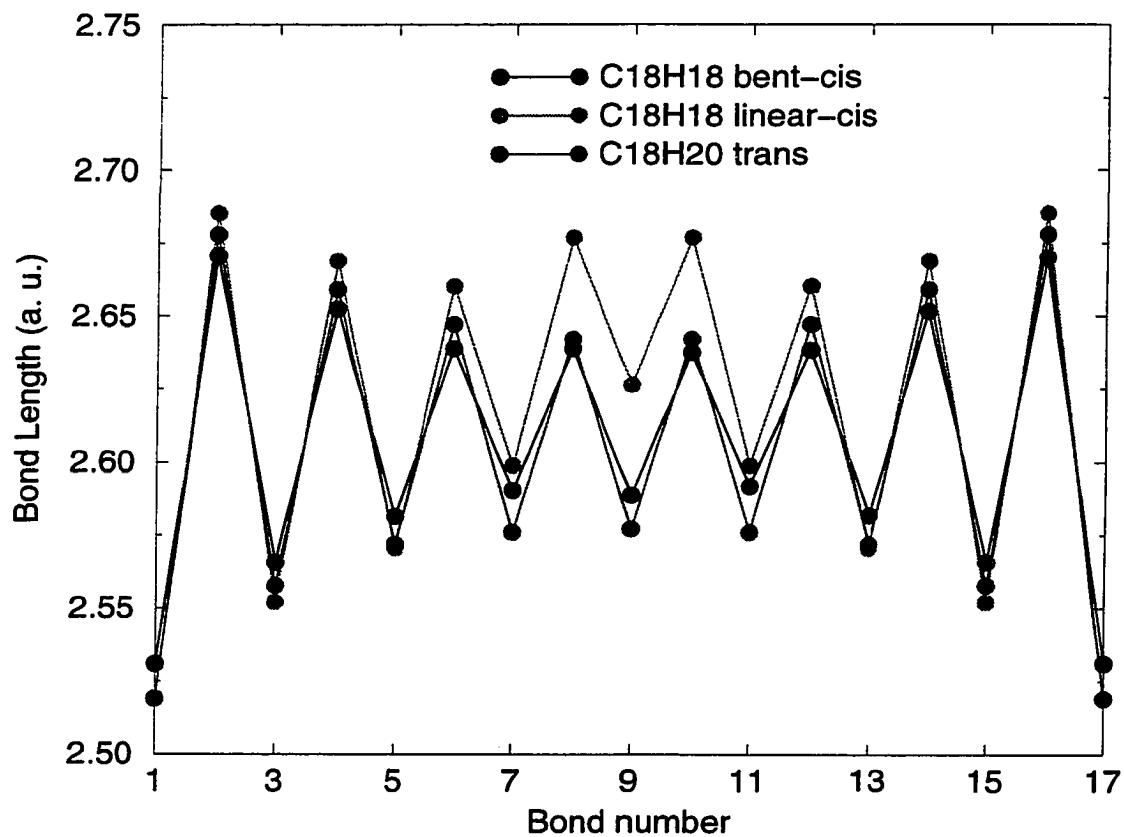


FIG. 11: Comparison of carbon-carbon bond lengths between all-*trans* $C_{18}H_{20}$ and the same system with a central *cis* bond and either a straight or bent geometry.

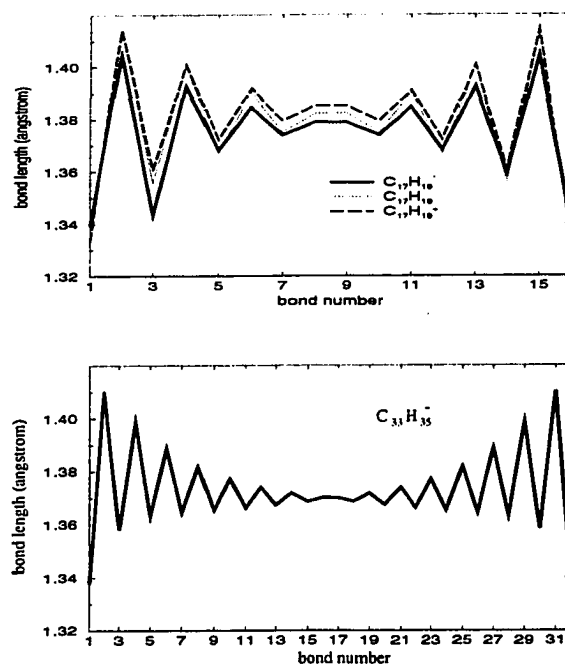


FIG. 12: Lowest-energy bond lengths.

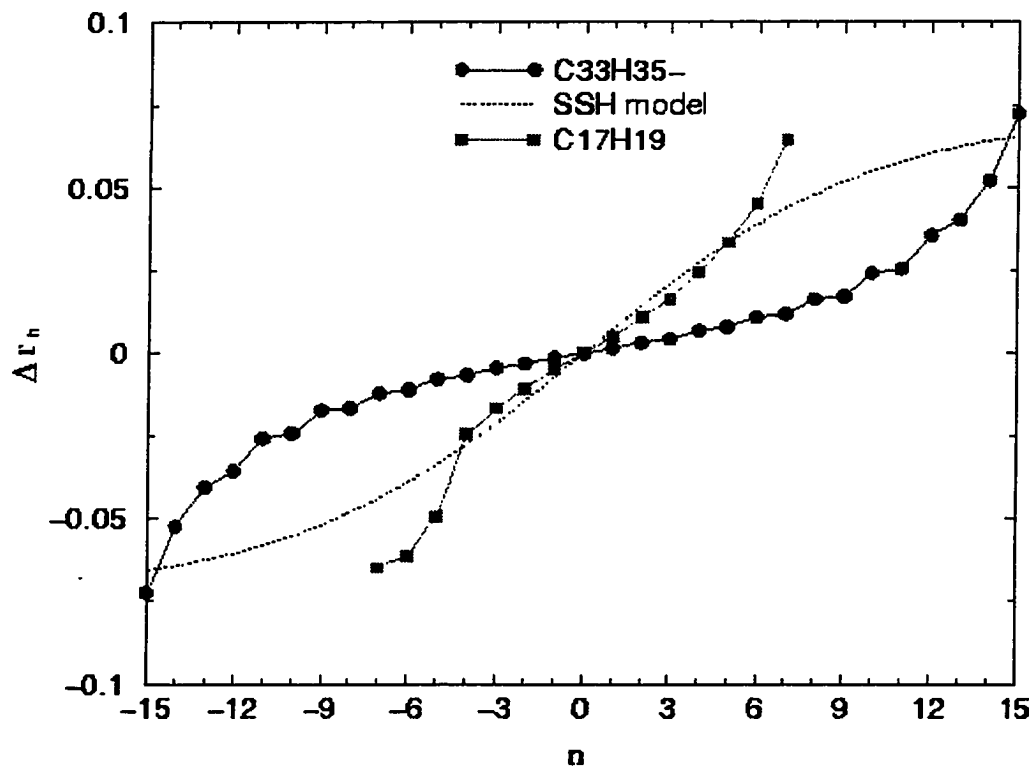


FIG. 13: Order parameter Δr_n from calculated geometry of $C_{33}H_{35}^-$ and $C_{17}H_{19}$. Here $n = 0$ labels the central carbon atom. Also shown is the order parameter predicted from SSH [Eq. (68)].

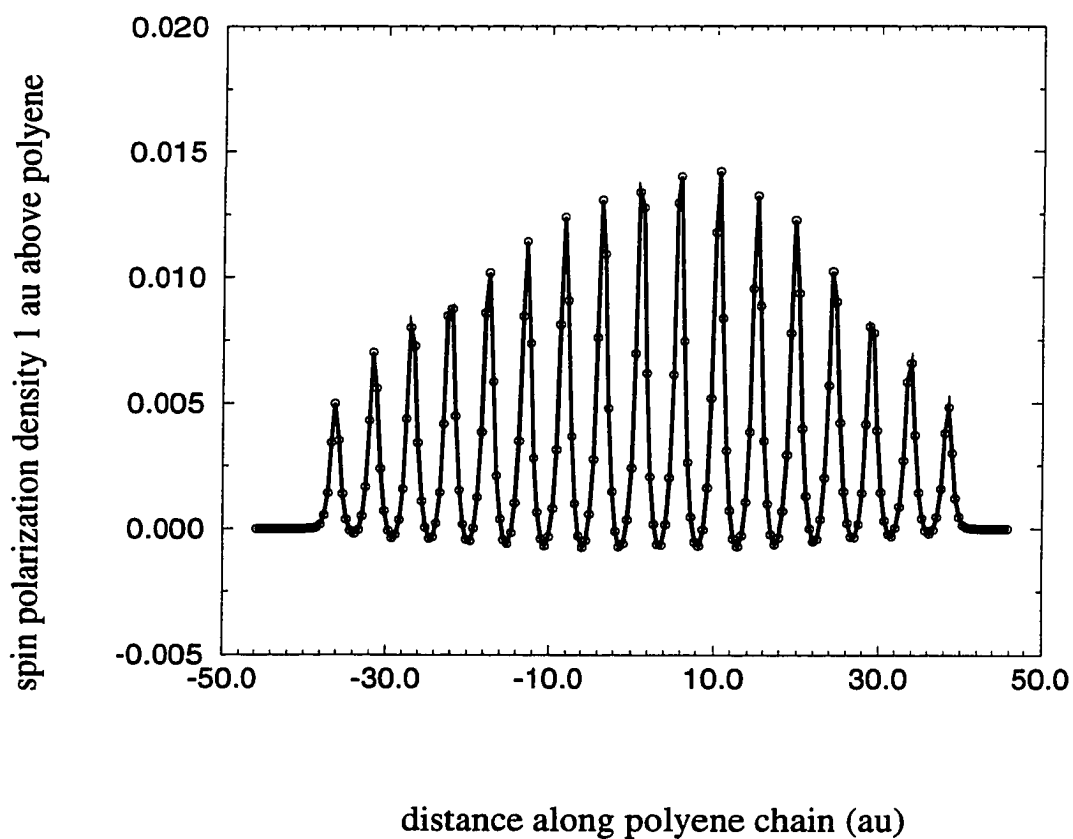


FIG. 14: Spin-polarization density along a line parallel to the $C_{33}H_{35}$ chain axis 1 au above the polyene plane.

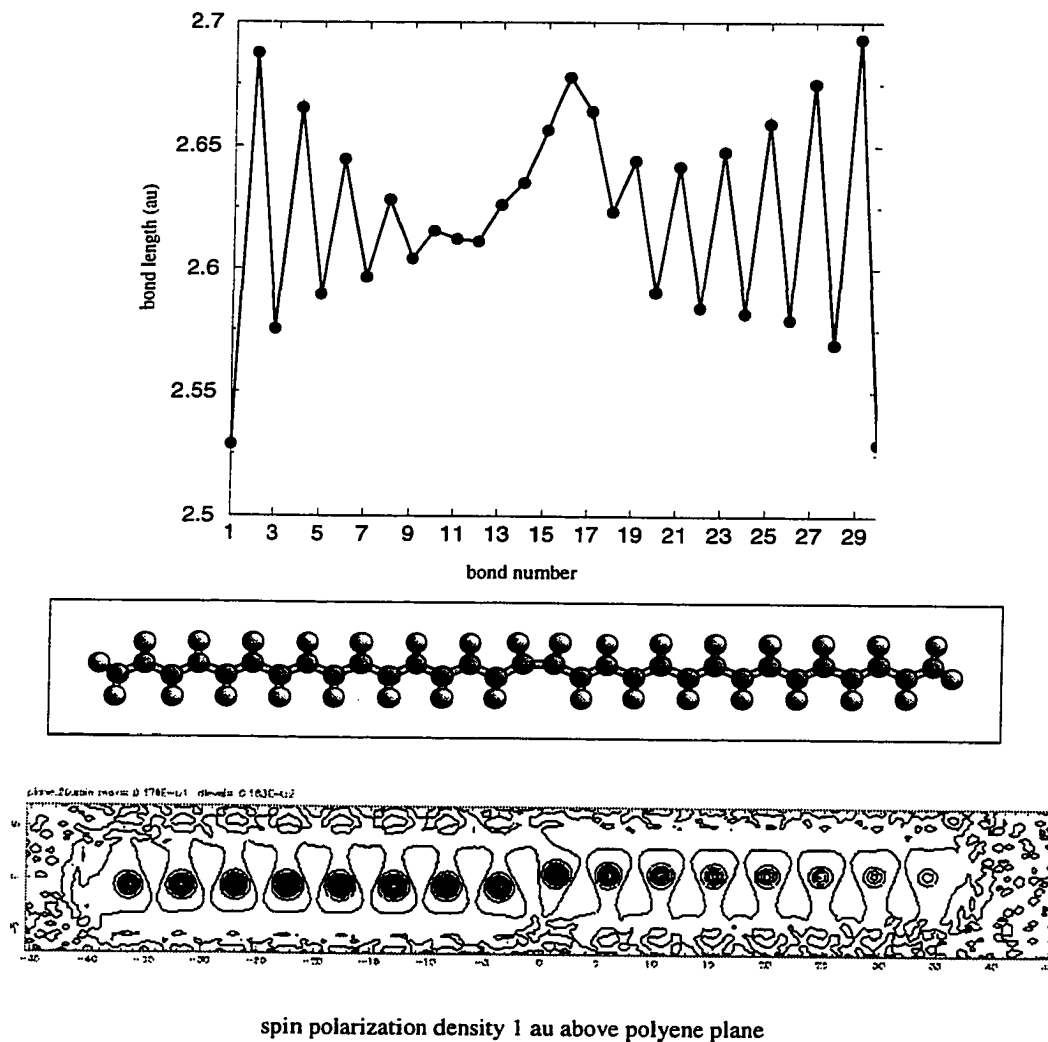


FIG. 15: Calculated carbon-carbon bond lengths and spin-polarization density 1 au above plane of $C_{31}H_{33}$ polyene with a *cis* bond.

5 DYNAMICS SIMULATION OF SOLITONS

In this chapter we review results of other recent dynamics studies of mobile solitons in PA. Previous studies have used empirical Hamiltonians almost without exception to investigate the qualitative motion of solitons. Methods used to initiate soliton dynamics are discussed. The initial conditions used for our simulations are also described below.

5.1 Brief summary of previously published simulation results

Most of the previous studies of solitons in PA address the soliton's dynamical properties through observations of static properties of chains containing the soliton defect. For example, Chance et al. [65] used a semiempirical method to find solutions of the Hartree-Fock Hamiltonian for a polyene with 17 carbon atoms and a static soliton kink. Specifically, the method known as MNDO (modified neglect of differential overlap) [66] was used. By performing many calculations with the kink centered on different points along the chain, they found the total-energy changes with a magnitude on the order of 1/100 eV until the kink is translated to within a few atoms of the terminal ends. Here the energy change away from the central position was ≈ 0.08 eV. Others have investigated the energetics of static kink-antikink pairs on finite chains using DFT [22, 67]. The results of these studies support the SSH picture of solitons as free quasiparticles in the absence of defects or interaction with phonon modes unrelated to soliton translation.

The dynamics of soliton have been studied exclusively with the SSH Hamiltonian and slight variants thereof, with only a couple of exceptions. There are other limitations of this model besides the dependence on uncertain parameters as discussed

above. With an SSH type model, only one type of lattice vibration is explicitly taken into account. It is not possible to distinguish neutral and charged defects from differences in geometry or kinetic properties. For finite chains, it can be shown that the system is unstable with respect to a shrinking of the entire chain, which makes an external force to keep a constant length necessary [68].

Despite the model's simplicity, the corresponding equations of motion appear to give qualitatively correct descriptions of dynamical properties. Su and Schrieffer used the model to predict that solitons could be photogenerated by a mechanism where electron-hole pairs evolve into solitons within an optical phonon period ($\approx 10^{-13}$ sec). This result has been confirmed by experiment [3]. Results from simulations performed by Su and Schrieffer for a mobile soliton on a chain with 31 carbon atoms predict a nearly constant soliton velocity of $\approx 1.4 \times 10^4$ m/sec. In the SSH simulations the soliton seems to “bounce” elastically from chain end to chain end as if moving in a “particle in a box” potential well. The speed should, of course, depend on the parameters and initial conditions chosen. The only initial condition reported by Su and Schrieffer (for a dynamics with a single soliton) is the configuration where $\Delta r_n = \Delta r_\infty$. This corresponds to the energetically unfavorable geometry with uninterrupted bond alteration (see Fig. 16). The system distorts to form a double bond at each end plus a mobile soliton. The speed is on the order of the speed of sound in this model, $\approx 1.5 \times 10^4$ m/sec. The effective mass of the soliton has also been estimated within the SSH model and given by [11]

$$M_{eff} = \frac{4}{3} \left(\frac{u_0}{a} \right)^2 \frac{M}{l}, \quad (72)$$

where u_0 is the dimerization amplitude along the chain axis, a is half the unit cell length of the infinite chain, M is the mass of a carbon-hydrogen bonded unit, and l describes the number of unit cell lengths covered by the soliton half-width. Using estimate from experiments gives $M_{eff} = 7.0 \times 10^{-30}$ kg, which is $\approx 8 m_e$.

One of the very few previous dynamical studies not using SSH was done by Förner et al. [69] for a soliton in a $(CH)_{29}$ system. They employed a Parisar-Parr-Pople Hamiltonian, which is a semiempirical Hamiltonian extending the SSH by including “on-site” and “off-site” electron-electron repulsion plus nearest-neighbor exchange. It is basically an approximate π electron self-consistent field method. This method has some practical difficulties like those mentioned for SSH. As for SSH a fictional force must be introduced to stabilize the system against lattice shrinking. The kink width is highly dependent on the exact value chosen for the on-site Hubbard U correlation parameter, and the velocity and spin density are highly dependent on the method used to compute the resonance integrals needed to compute the Fock matrices. With a parameter set used to reproduce experimental dimerization in long even-membered chains, Förner et al. found a narrow soliton covering about 6 lattice sites with a velocity of $\approx 3.1 \times 10^4$ m/sec. Their rough estimate for the effective (kinetic) mass is $\approx 15.0 m_e$. A distorted initial geometry corresponding to the order parameter shown in Fig. 17 was used to initiate soliton dynamics. The point along the chain where the order parameter changes sign (the soliton center) is energetically favored to be at the center, and the kink does in fact move from the end regions toward the center as expected.

The one previously published ab initio molecular dynamics simulation of soliton in PA was done by Champagne et al. [61]. The dynamics treatment here simulated a charged soliton in a $C_{13}H_{15}^+$ polyene system. The initial soliton structure is obtained from the ground state geometry of a restricted Hartree-Fock/Slater-type-orbitals method. A standard molecular dynamics procedure is used where the system evolves according to the equation

$$M_I \ddot{\mathbf{R}}_I = -\nabla_{\mathbf{R}_I} E[\mathbf{R}_I, \psi]. \quad (73)$$

This is the same as Eq. (60) above except here ψ is a single spin unrestricted determinant built from nonorthogonal spin orbitals with complex coefficients. Soliton motion

is initiated by switching on an external static electric field pulse parallel to the chain axis. The total evolution of the simulation in this study was 210 au (5.06 fs), which was enough time to observe the soliton center move just two carbon-carbon bond distances along the chain. The speed of the soliton was estimated at $\approx 5.9 \times 10^4$ m/sec and the (kinetic) effective mass is estimated at $\approx 10m_e$. This study also attempts to identify the vibrational normal modes having a pronounced soliton-like motion component. They find that chains with 21 or more carbon atoms have at least 3-4 modes making a substantial contribution to the mobile bond-alternation pattern expected (from SSH theory) for soliton translation.

My own ab initio molecular dynamics simulations represent an attempt to extend and qualitatively improve upon the above results. Specifically, I performed simulations of long enough duration to observe periodic soliton motions along the entire chain, including interaction with carbon atoms near the chain end. I investigated both charged and neutral soliton species at the ab initio level. I included the presence of a conformational defect that should be very common in the real PA system, a *cis* bond. Finally, I performed simulations for chains with up to 33 carbon atoms, which is more than twice the length considered in the ab initio study above and probably more representative of PA chain segments in the real bulk sample.

5.2 Initial conditions used for this dynamical study

I used two of the methods described above to initiate soliton motion in C_nH_{n+2} polyenes of various charge species for $n = 17$ and $n = 33$. For systems with all-*trans* type PA bonding, a geometry distortion similar to that used by Förner et al. was employed. For systems with a *cis* bond interruption of the *trans*-PA bonding, a method similar to that used by Su et al. was employed. These systems started out in an energetically unfavorable state with uninterrupted dimerization. A soliton was created as the system relaxed.

5.3 Initial configurations for all-*trans* polyenes

The initial bond length ordering I used for the all-*trans* polyenes with 17 or 33 carbon atoms is shown in Fig. 18. The initial order parameter $\frac{\Delta r_n}{\Delta r_\infty}$ for the longer polyene systems is shown in Fig. 19. The energy for each system was minimized using our density functional program as described above. These calculations were performed for (neutral) $C_{17}H_{19}$, $C_{33}H_{35}$, $C_{17}H_{19}^-$, and $C_{33}H_{35}^-$. This geometry was arrived at by inspecting the geometries of the ground states of each of the systems and by guesswork. The aim was to observe the soliton kink in motion as the system distorts towards a lower energy configuration while minimizing the excitation of vibrational modes unrelated to soliton motion. The change in the sign of the order parameter is more gradual than the abrupt transition chosen by Förner et al. for their simulations. However, as will be shown, I did not avoid the excitation of large-amplitude long-wavelength acoustic phonons. The vibrational motion significantly affects the soliton transport and can make the determination of the soliton center difficult since many changes in the sign of the order parameter can be induced. The order parameter probably has appreciable fluctuations even when the system is very close to the ground state. Su [70, 71] and Fradkin and Hirsch [72, 73] have shown that quantum zero point fluctuations of the ground state lattice should disrupt the dimerization and cause random changes in sign of the order parameter. Su reports that using a Monte Carlo functional integration method to evaluate the expectation value of the order parameter for a 16 carbon atom PA system gives $|\langle \frac{\Delta r_n}{\Delta r_\infty} \rangle| \approx 0.8$, where the exact ground state is characterized by $\frac{\Delta r_n}{\Delta r_\infty} = \pm 1$.

5.4 Initial configurations for polyenes with one *cis* bond defect

Dynamics calculations were performed for the systems $C_{17}H_{19}^-$, $C_{33}H_{35}^-$, and $C_{33}H_{35}^+$ with one *cis* bond defect adjacent to the central carbon atom. A bent configuration was chosen to minimize lattice strain around the *cis* region as shown in

Fig. 20. The initial bond lengths and order parameter chosen are shown in Figs. 21 and 22. There is no interruption of the short-long bond alternation pattern; therefore, the order parameter does not change sign. This is an energetically unfavorable initial condition that will create a soliton as the system starts to relax to a lower energy state. It was shown above in section 4.4 that polyenes with a central *cis* bond do not have a soliton kink in the ground state. It is therefore not possible to guess at an initial soliton geometry based on a distortion of the ground state. However, it is still desirable to have the resulting soliton kink moving across the chain with a minimum number of large-amplitude phonons which complicate observation of the soliton. To achieve this aim, I used the following procedure to obtain the geometry described by Figs. 21 and 22. The ground state of the polyene systems with an extra hydrogen atom bonded to a terminal carbon atom was calculated. The extra hydrogen on the terminal end of the resulting $C_{17}H_{19}^-$ or $C_{33}H_{36}^\pm$ polyene causes the final carbon-carbon bond to be longer than average as seen in Fig. 21. The bond length alternation pattern on the rest of the polyene is the same as that found previously for the all-*trans* $C_{32}H_{34}$ system shown in Fig. 8. Before starting the molecular dynamics simulation, one of the terminal hydrogen atoms is removed from the system, making a configuration such as that in Fig. 20. The long terminal carbon-carbon bond is energetically unfavorable in the resulting system. A soliton is created at the polyene end and moves towards the *cis* region.

The method used to define the order parameter seen in Fig. 22 for the system with one *cis* bond is slightly different than the method used for Δr_n shown for the all-*trans* polyene. The order parameter is given by Ω_n , defined as

$$\Omega_n = -1^n \frac{(d_n - d_{ave})}{\Delta r_\infty}. \quad (74)$$

Here d_n is the length of the n_{th} carbon-carbon bond and d_{ave} is the average bond length of the corresponding all-*trans* polyene system. Δr_∞ as above is the difference in length between any two adjacent carbon bonds in the infinite idealized *trans*-PA

system (0.08 \AA). This way of finding the order parameter gives the same basic information concerning the position along the chain where the bond length alternation pattern changes. Plotting the order parameter defined this way gives some information about the change of individual bonds as time passes. This is useful information when observing the dynamical behavior of the simulated system with one *cis* bond shown above since the extreme motions of the individual atoms near the polyene end and changes in bond length there greatly affect the observed soliton propagation.

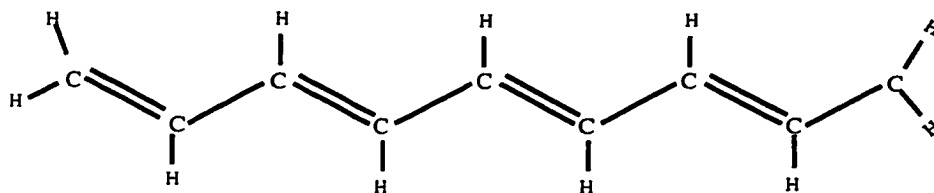


FIG. 16: Schematic representation of an odd-membered polyene with a uniform, uninterrupted dimerization. Such an initial configuration can be used to initiate soliton dynamics in simulations.

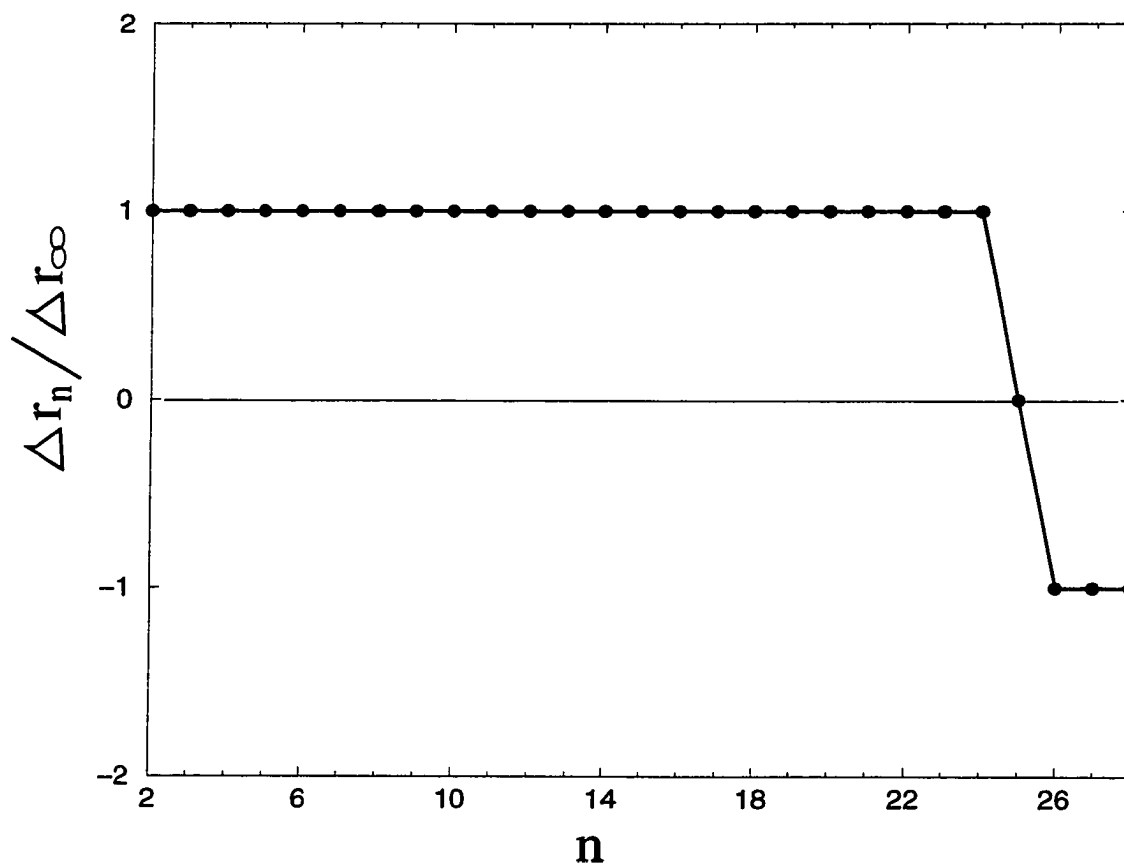


FIG. 17: Bond order parameter for the initial geometry used by Förner et al. to initiate soliton dynamics.

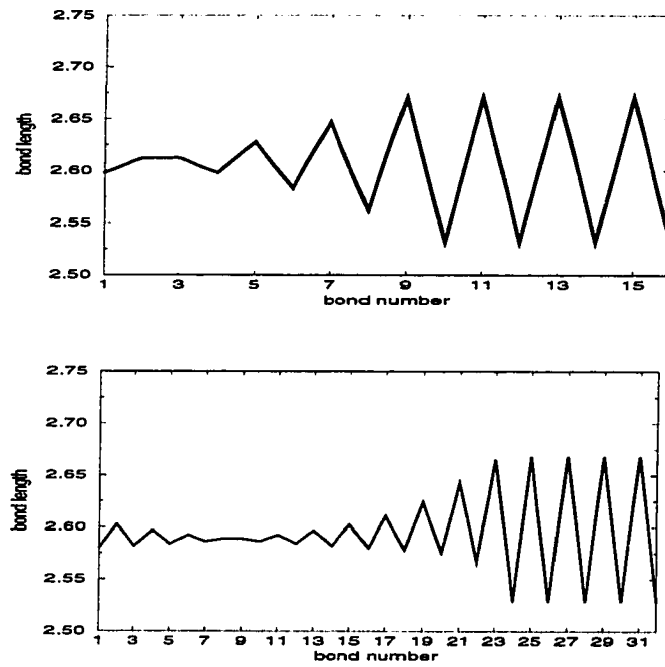


FIG. 18: Starting bond length configurations for our dynamics simulations.

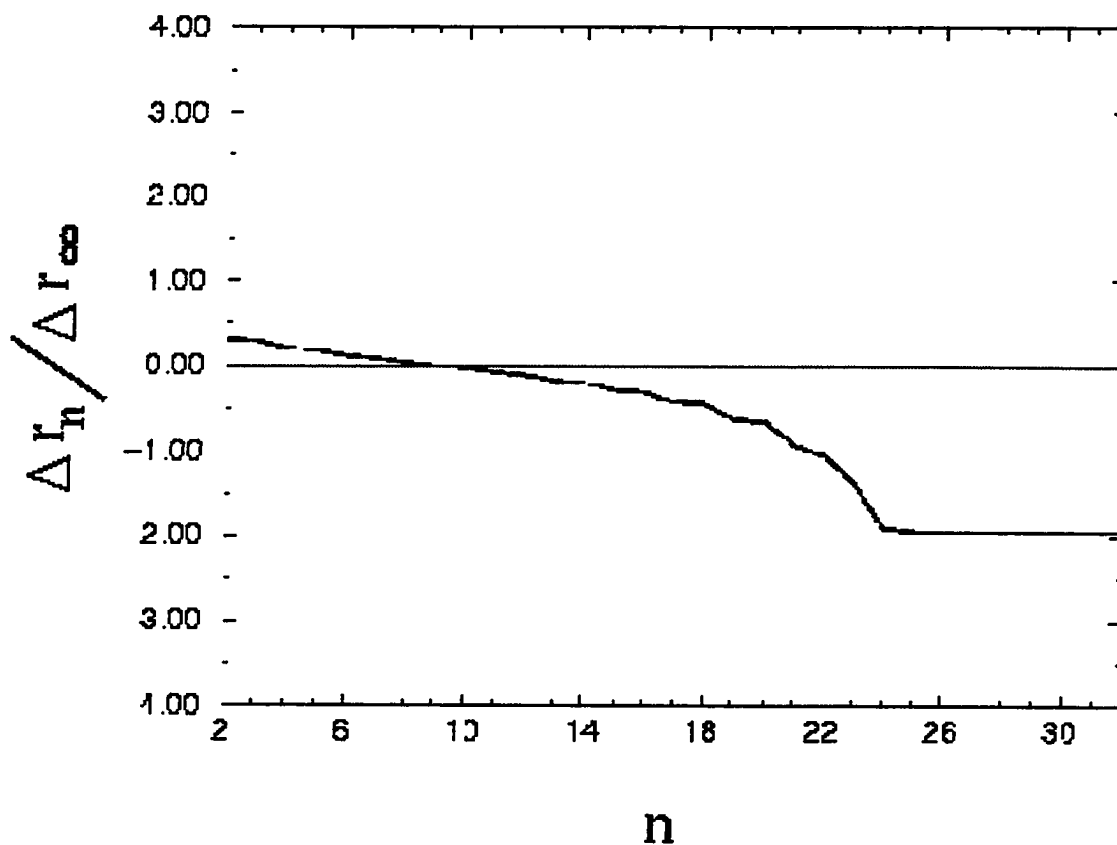


FIG. 19: Initial bond order parameter for all-*trans* systems with 33 carbon atoms



FIG. 20: Schematic picture of the polyene with one *cis* bond for which dynamics simulations were performed.

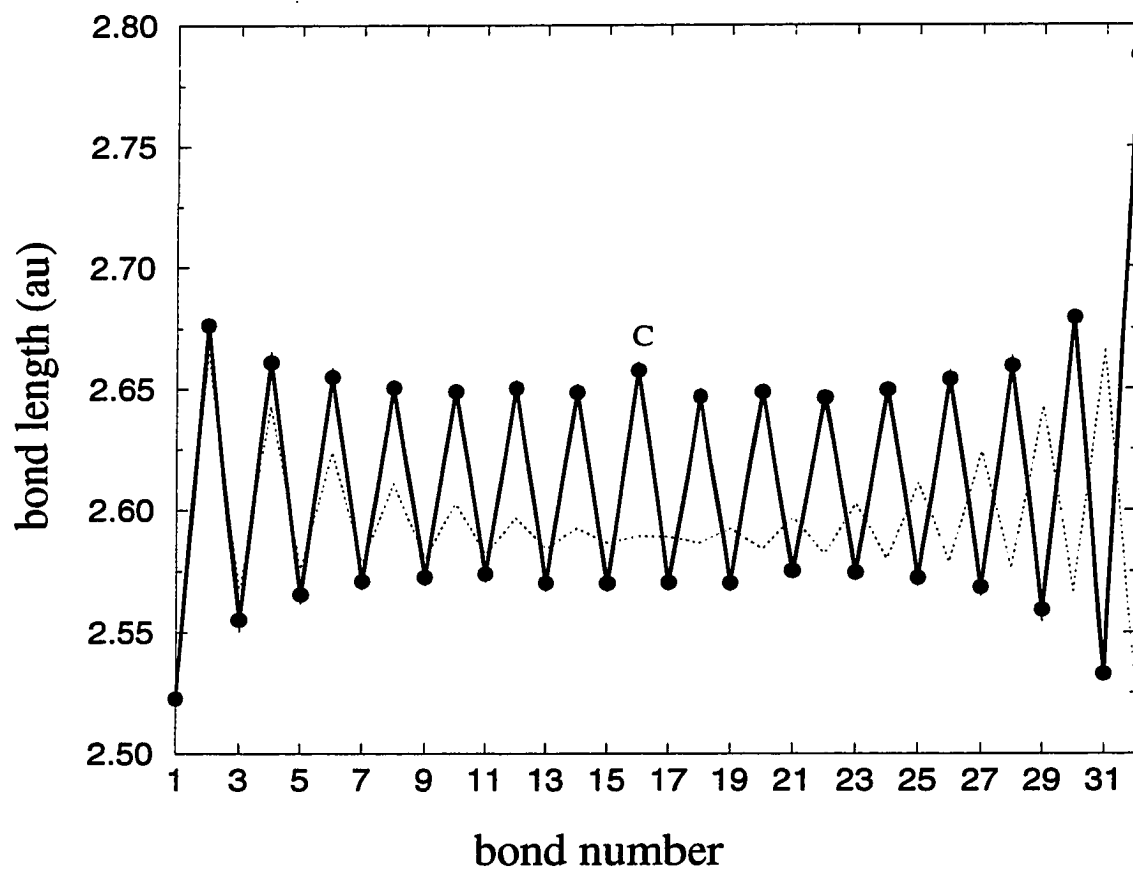


FIG. 21: Initial bond lengths of polyene system with one *cis* bond. The dotted line indicates the bond lengths found for the all-*trans* polyene shown for comparison.

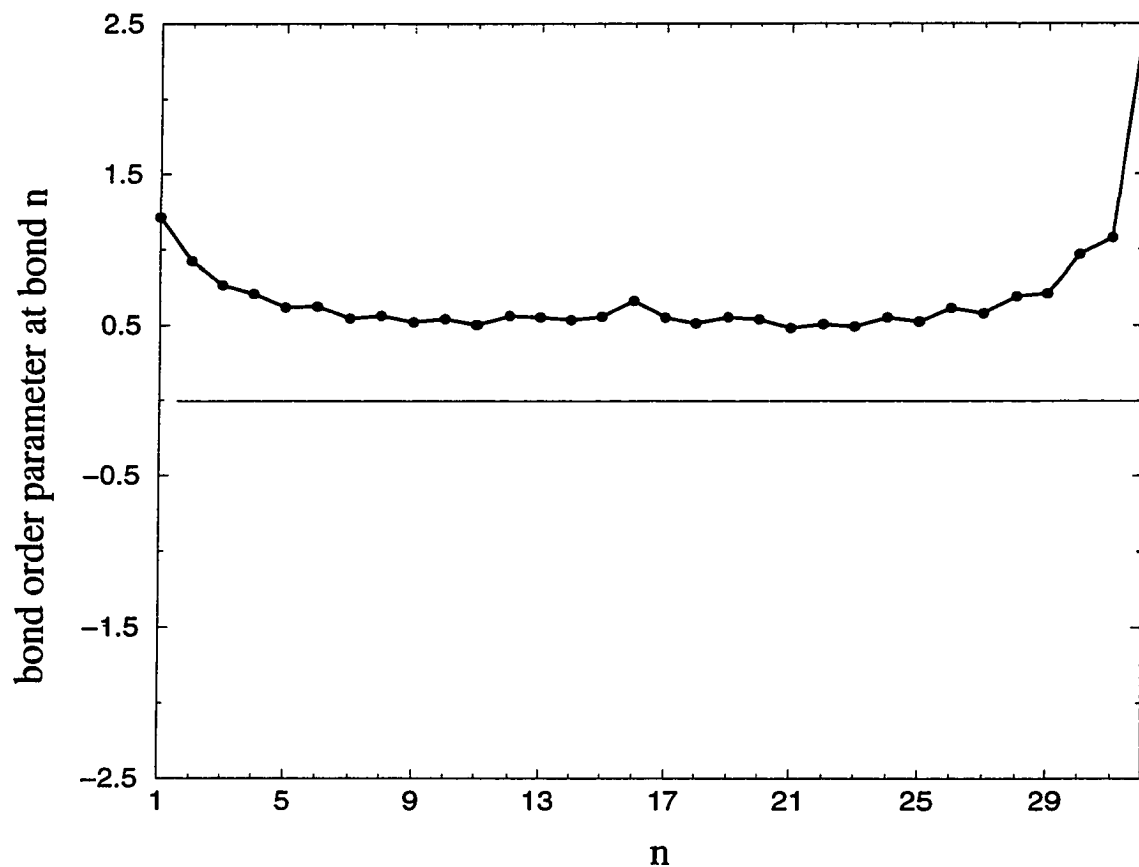


FIG. 22: Bond order parameter of polyene system with one *cis* bond at the beginning of dynamics simulation.

6 CAR-PARRINELLO AB INITIO MOLECULAR DYNAMICS RESULTS

Car-Parrinello ab initio molecular dynamics were performed for the polyenes C_nH_{n+2} ($n = 17, 33$) with initial polyene geometries as described above. The molecular dynamics time step Δt used for all simulations is $\Delta t = 1$ au (0.0242 fs). The fictitious mass associated with the electronic orbitals is $\mu = 300m_e$. The use of these parameters is described above in section 3.6. The total time for which each simulation was performed ranges between 1500 and 4000 au. For each system this time duration is sufficient for at least one “round trip” of the soliton kink across the polyene chain. This means that the soliton travels across the midpoint of the chain until it loses all kinetic energy and then returns back across the chain close to its initial position. The position of the soliton center is determined by direct inspection of the bond order parameter such as that in Fig. 19. The changing position along the chain length where the order parameter changes sign corresponds to the changing position of the soliton center.

I list in Table V the average speeds of the soliton in each system. The table lists the average speed of each soliton during each trip over the center region of each chain. With the initial conditions described above, the soliton velocity is $\approx 1 \times 10^5$ m/s for each system. The speed of the solitons tends to diminish by 10-30% with each pass over the chain. This reduction is probably due to scattering by phonon modes which are not coupled to the collective motion of the soliton. This is qualitatively different from the results described above obtained by Su and Förner et al., who found an essentially constant soliton velocity with the strictly one-dimensional models they employed. The speed of sound in metallic (doped) PA has been reported to be $v_s = 1.85 \times 10^4$ m/s [74], about one-fifth the typical speed I found. My result is also

TABLE V: Average speed of the soliton in each simulated system for each pass over the chain center (m/s).

polyene system	1st pass	2nd pass	3rd pass	4th pass
$C_{33}H_{35}^-$	2.0×10^5	1.4×10^5		
$C_{33}H_{35}$	8.6×10^4	9.9×10^4	7.4×10^4	
$C_{33}H_{35}^-$ with <i>cis</i>	2.7×10^5	1.8×10^5	1.2×10^5	8.6×10^4
$C_{33}H_{35}^+$ with <i>cis</i>	1.6×10^5	1.3×10^5	2.4×10^5	
$C_{17}H_{19}^-$	1.3×10^5	1.3×10^5	1.0×10^5	7.9×10^4
$C_{17}H_{19}$	1.2×10^5	8.4×10^4	8.3×10^4	

slightly higher than the speeds predicted by Champagne et al. (5.9×10^4 m/s), Förner et al. (3.5×10^4 m/s), and Su et al. (1.3×10^4 m/s) with their methods as described above. Comparing these speeds may not be so meaningful, however, since the initial conditions used to initiate the soliton motion are different in each case. Also, since the soliton is moving in a nonlinear system, slight differences in initial conditions may lead to considerable differences in speed. It is apparent from the results in Table V that for each chain length, the soliton in the polyene with a net negative charge moves noticeably faster across the chain than the soliton in the corresponding neutral or positive system. The initial conditions were used for each polyene system. Ab initio molecular dynamics results for solitons of different charge species in the same polyene system have not been previously reported to my knowledge; thus, this is the first observation of this effect.

6.1 Details of soliton motion: A neutral soliton in all-*trans* $C_{33}H_{35}$

I attempt here to illustrate some details of the soliton motion observed from simulation of the all-*trans* $C_{33}H_{35}$ (neutral) system. The motion of the negatively charged soliton in the $C_{33}H_{35}^-$ system is qualitatively the same, although the speed is faster. In Figs. 23 through 31, I show the bond order parameter $\Delta\tau_n$ from Eq. (67) for consecutive time intervals 50 au (1.21 fs) apart. The initial geometry chosen

does not result in an order parameter that is well fit by a tahn function as described by Eq. (68). The subsequent order parameters are also generally not of this form, which is not surprising given that my ground state soliton pictured in Fig. 13 did not match this form either. At each time interval there is at least one location along the chain where the order parameter crosses $\Delta r_n = 0$. For most consecutive pictures, it is easy to observe this crossing, which signifies the soliton center, change position along the chain. Keeping track of the soliton position in this manner is complicated, however, by occasional disruptions in the bond ordering that result in three crossings. Inspection of the figures shows times including $t = 450$ au and $t = 2250$ au where there are three such crossings, which correspond to three interruptions or “kinks” in the bond ordering. The bond ordering in the region of the bond numbered 24-26 changes more abruptly than in other areas of the chain, perhaps due to the initial condition chosen. The initial order parameter does not change smoothly in this region. This is the region where kinks other than the original are created during the simulation.

As described in chapter 2, each kink in the bond ordering separates segments of the chain with the two different possible “phases” of bond ordering. When there are two kinks in the bond ordering, the second is called an “antikink” since it returns the bond ordering to the phase present before the first kink. A third kink, if present, must be a regular kink since it again changes the phase of the bond ordering (the sign of the bond order parameter) back to the opposite of what was present before the first kink. Because of topological constraints forced by the end bonds in our odd-membered polyene, there must be only an odd number of phase changes, or changes of sign (kinks) of the bond order parameter. When there are three kinks present, the middle one must be an antikink. A kink and an antikink can annihilate each other and leave only a single kink in the odd-membered chain.

Figure 32 is a plot of the position along the length of the chain of each of these kinks during the time of the simulation. As seen in the figure the original kink moves

by itself as the only kink until some vibrational excitation creates a kink-antikink pair at $t \approx 350$ au. The original kink and the antikink move towards each other and are each destroyed at some time between $t = 550$ au and $t = 600$ au. The remaining kink is left to move towards the chain center, which my static calculations indicate is the lowest-energy position for a soliton. As previously discussed the term soliton refers to a geometrical kink and an electron state with a modulated density expected to be well described by Eq. (71). The net spin-polarization density of the system for times between $t = 950$ au and $t = 1450$ au is shown in Fig. 33. The modulated character of the density is what we expect for a neutral soliton, and the position maximum density corresponds with the position of the geometrical kink. When three kinks are present at the same time, the modulated density appears to stay centered around the original kink until annihilation occurs, when the soliton density quickly shifts to be centered around the remaining geometrical kink.

Figures 34 and 35 show the value of the potential energy vs. time. Also shown are the bond length configurations at various times from which it is possible to see the soliton kink changing position along the chain. The ground state of the static system is found to have a total energy of $E = -206.6075$ au. The initial dynamics is started with the system having energy about .631 eV higher than this ground state value. As the system evolves, the energy remains at least 0.13 eV above the ground state value. It seems clear that the extra energy has excited some phonon modes not directly related to the soliton motion. The soliton moves from site to site in a time period on the order of 50 au. The change in the value of the potential energy during such an interval varies from about 0.025 to 0.05 eV, depending on how steep the potential energy surface happens to be. The energy required for a soliton to move from one carbon atom site to the next was estimated by Su et al. to be 0.002 eV by using the SSH Hamiltonian. This estimate was made without any nuclear motion unrelated to the soliton translation. I can estimate that an activation energy of about

0.025 eV is required for my simulated system with vibrational modes that gradually slow the soliton.

Figure 32 shows that during the time interval 600-2300 au, when there is one soliton kink in the chain, the position of the soliton moves back and forth across the center along a length roughly symmetric about the center. It is presumed that the soliton has an effective mass, so that as it gains some kinetic energy by moving towards the center region, it proceeds to “overshoot” the minimum energy position until all the gained kinetic energy is again converted to potential energy. The effective mass M_s of the soliton is considered an important characteristic directly related to its mobility. We can make a very rough estimate of this quantity. We assume that the time average of the nuclear kinetic energy T is primarily associated with soliton displacement. Then M_s is given by $2T/v_s^2$, where v_s is the average speed. This estimate yields $M_s = 1.2 \times 10^{-30} \text{ kg}$ ($\approx 1.3m_e$). This rough estimate is of the same order of magnitude as the estimates made by Su et al. [10] and Champagne et al. [61].

6.2 Details of soliton motion: A negatively charged soliton in a *trans* polyene $C_{33}H_{35}$ with a central *cis* bond

The initial geometry and bond length configuration used to initiate Car-Parrinello ab initio molecular dynamics for $C_{33}H_{35}$ with a central *cis* bond were described above in Figs. 21 and 22. To illustrate the changing position of the mobile soliton peak, I again show the bond order parameter for the entire chain at intervals of 50 au for times from $t = 0$ to $t = 2650$ au. The modified order parameter Ω_n described above in Eq. (74) is plotted in Figs. 36 through 44. The plots appear more jagged at times here than those above since here the plots vary according to individual bond lengths. At time $t = 0$ through $t = 150$, the order parameter does not change sign. A soliton kink does not appear in the bond ordering until around 200 au. Figure 45 shows a contour plot of the HOMO level density at $t = 0$. Although a geometrical kink does not exist, there is already a modulated density of a soliton which shifts to-

wards the middle of the chain and follows the position of the geometrical kink as the system relaxes. The bond length of the final carbon bond is seen to be much greater than average bond length of the rest of the chain. This results in a large vibrational amplitude of the final bond that can be seen from the order parameter plots. This vibrational motion appears to induce a second bond ordering kink (an antikink) at $t = 850$ au. As seen from the order parameter plots the kink and antikink move towards each other and annihilate between $t = 1000$ and $t = 1050$ au, after which there is no geometrical soliton kink until about $t = 1150$ au. At this point in time the shrinking of the elongated carbon-carbon bond is again forcing the creation of a new soliton kink, which proceeds to make another trip across the polyene chain.

A plot of the position along the chain of each kink is shown in Fig. 46. The position of the central *cis* bond corresponds to the $y = 0$ position on the vertical axis. As the soliton starts from the right-hand extremity of the chain and moves toward the *cis* region, it is moving at a nearly constant speed until it crosses over into the other side of the chain. The distance the soliton travels across this second half of the chain before returning back is at least 30% less than the distance covered on the other side. The unsymmetric motion of the soliton is most likely due to a small energy barrier encountered when the bond ordering of the *cis* region is changing as the soliton passes through. The change of the bond length order in the *cis* region is shown in Fig. 52. We see that the horizontal *cis* bond (with length "b") is originally longer than the adjacent bonds, like the structure seen in the trans-cisoid isomer of Fig. 9. As the soliton moves towards the central kink region, the ordering gradually changes until the horizontal *cis* bond is shorter than its neighbors, like the structure of the cis-transoid isomer of Fig. 9. We see the bond ordering never completely reverses. The system prefers a longer horizontal *cis* bond; as the bond ordering changes back to this ordering as the soliton passes back over the *cis*, we see from Fig. 46 that the soliton seems to recover the speed it had before passing over the *cis* bond. In other words,

it appears that the *cis* region raises the potential energy surface seen by the soliton as it passes over, but the kinetic energy lost is restored on the return trip.

Contour plots of the HOMO level density 1 au above the plane of the polyene are shown in Figs. 47 through 51 for times between $t = 325$ au and $t = 1025$ au. The density is shown for intervals of 100 au. Also pictured is the change in the HOMO level density $\Delta\rho$ between these time intervals. As for the case of the all-*trans* polyene, the electronic density of the soliton covers the full length of the polyene. The position of maximum density (soliton center) moves back and forth across the chain, just as the neutral soliton discussed above does. The pictures of the change in density show that as the soliton moves the density generally increases over the seven or eight carbon atom sites nearest the leading edge of the soliton. For times between $t = 725$ au and $t = 925$ au, we see that the change in density is mostly concentrated on the final carbon atom site on the extreme leading edge of the soliton. It is during this time that the antikink is being created from the vibration of the final carbon-carbon bond. By the time $t = 1025$ au, the bulk of the density is at the extreme right side of the polyene and both the electronic and geometric configurations are returning close to their state at $t=0$. In this simulation we see that interruptions in bond ordering produced by large amplitude vibration affect the shifting of the soliton density in a subtle way. As the geometrical kink is being destroyed, the electronic density shifts quickly to the end until a new geometrical kink develops to move across the chain again. The new soliton kink moves with a noticeably smaller velocity than the original. This is clear from the position vs. time plot of Fig. 46. Presumably, the soliton-phonon interaction has dissipated some of the soliton's energy. The soliton makes a shorter trip across the center of the polyene and continues this slowing trend on its way back across the chain.

Figure 53 shows the how the length of the final carbon-carbon bond distance changes with time. The bond shrinks or expands to an extremum away from an

apparent equilibrium distance of 2.55 au every 450-500 atomic time units. The other carbon bonds also change lengths as the soliton passes over their position on the chain; however, their change is more gradual, as indicated by the change in the central *cis* bond in Fig. 52. The potential energy vs. time curve for the system in Fig. 54 has peaks at intervals of about 450-500 au that correspond closely to the times when the final carbon-carbon bond is at an amplitude extrema. This strong chain end vibration seems to have a strong effect on the potential energy surface.

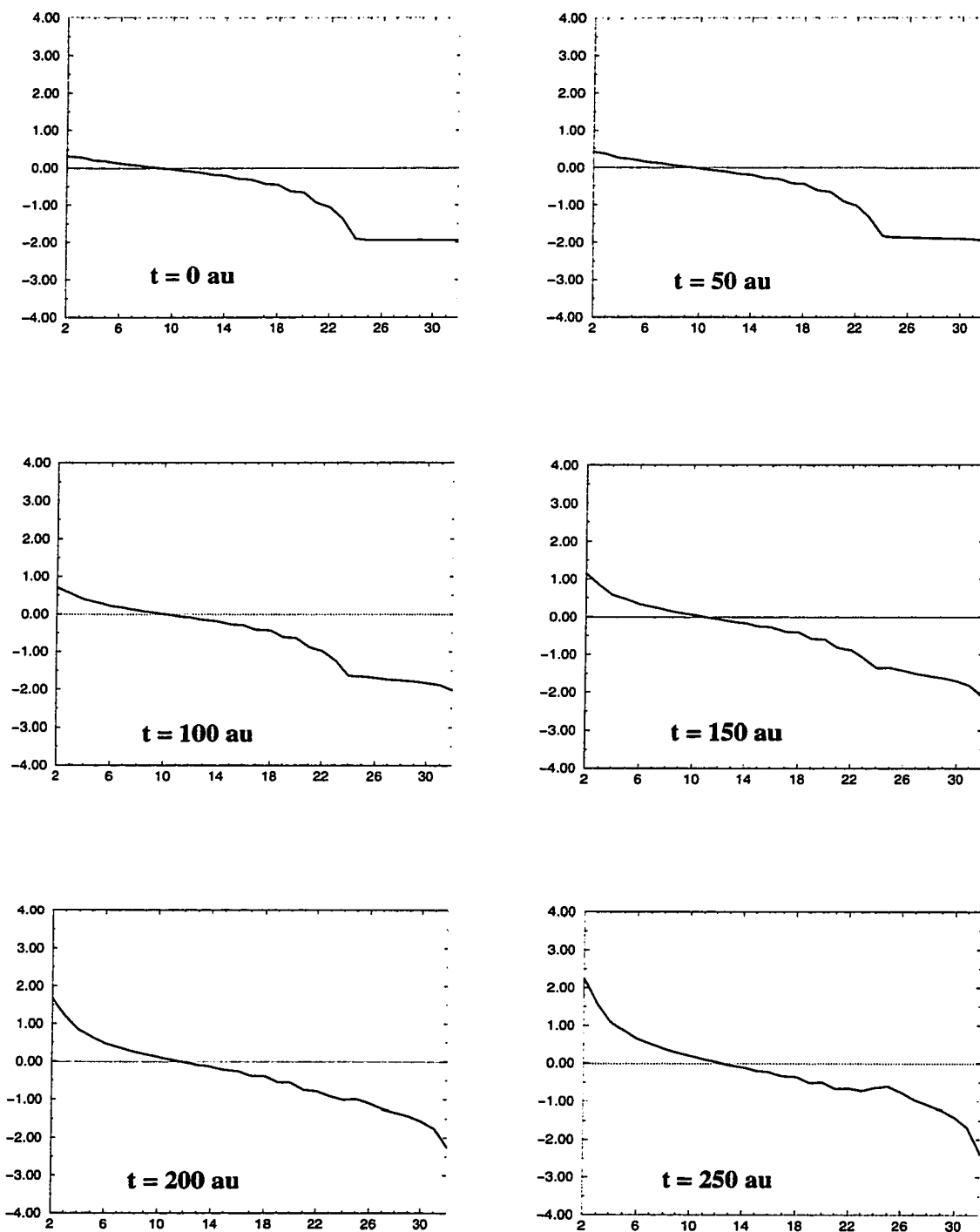


FIG. 23: Order parameter from $t = 0$ to 250 au.

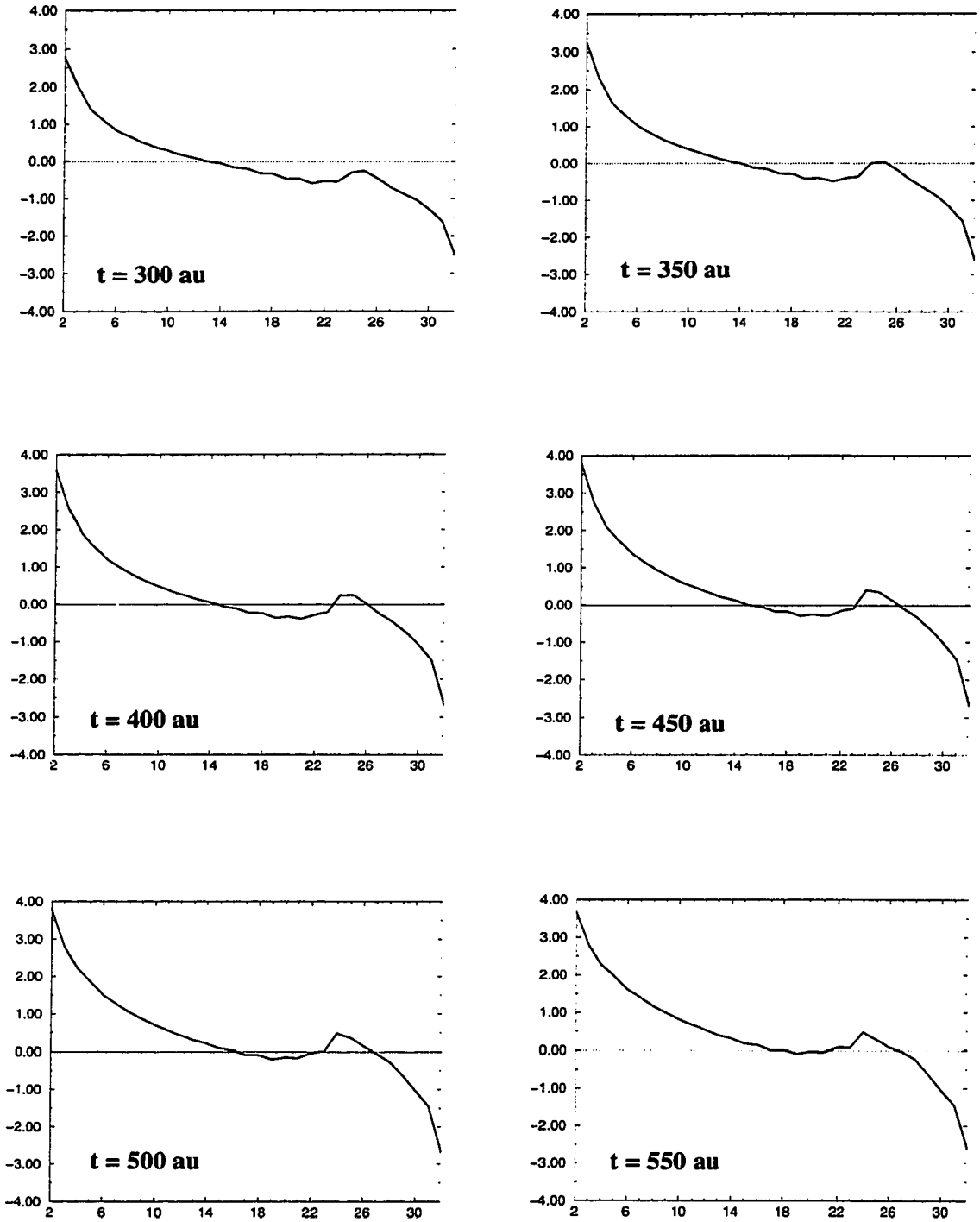


FIG. 24: Order parameter from $t = 300$ to 550 au.

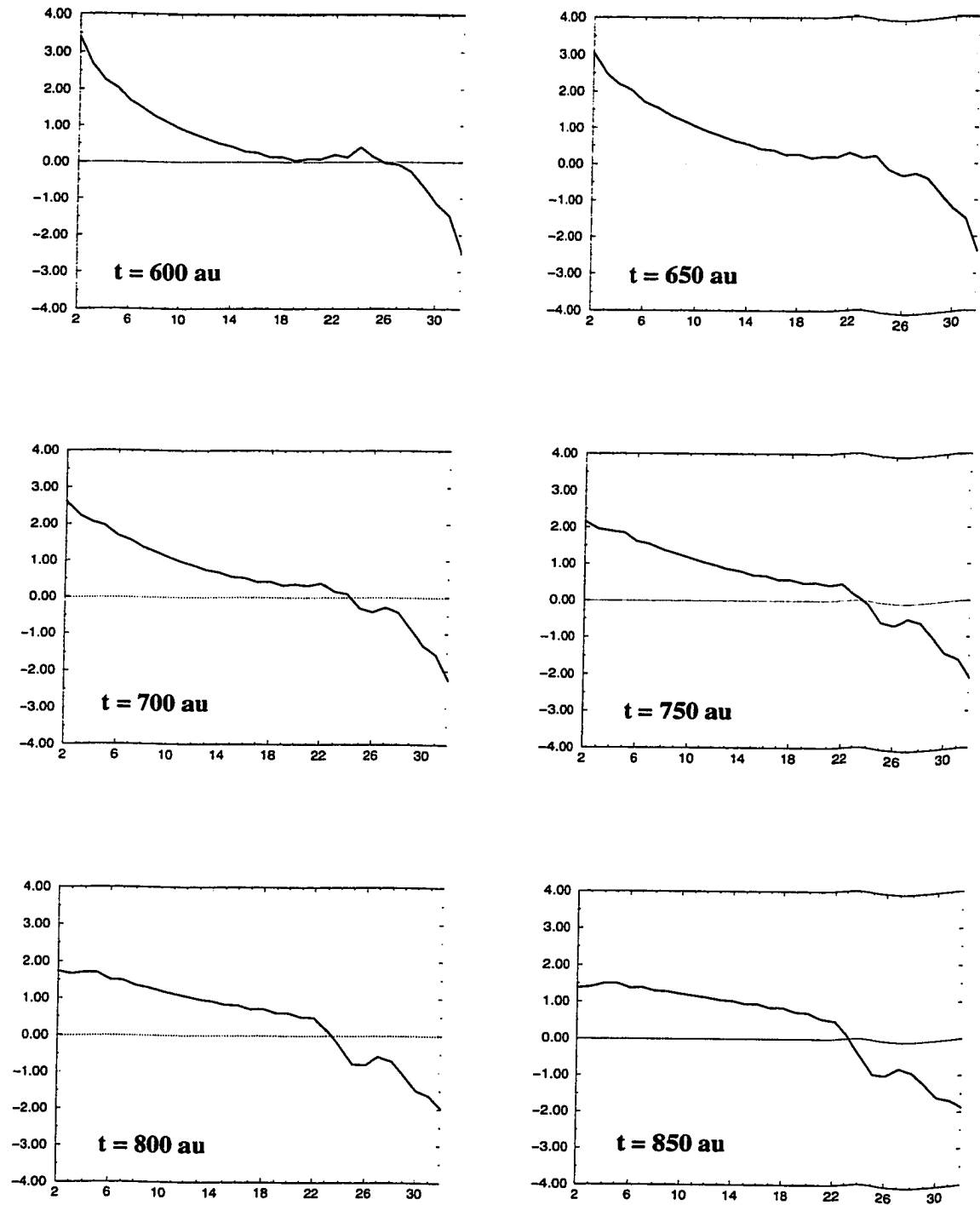


FIG. 25: Order parameter from $t = 600$ to 850 au.

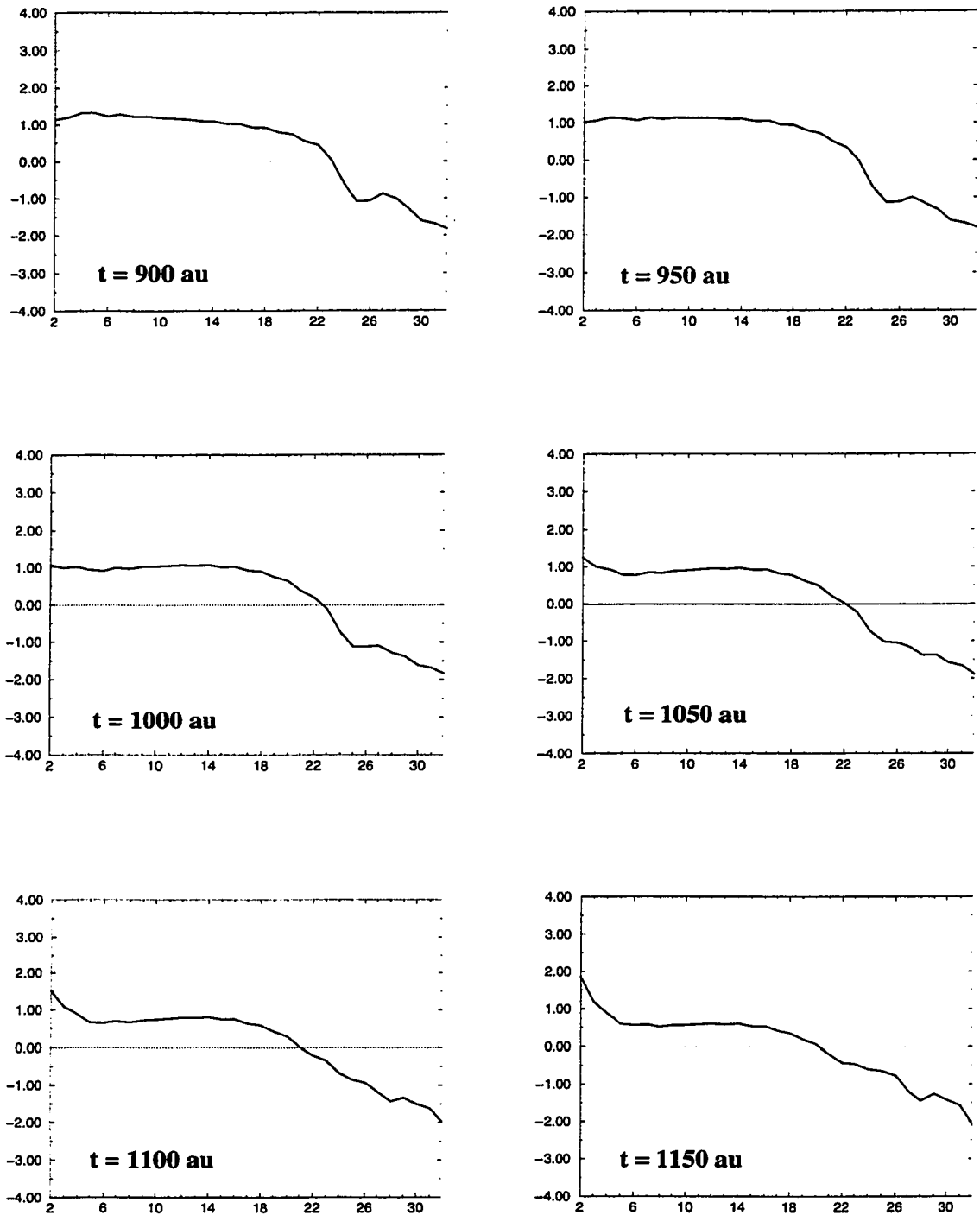


FIG. 26: Order parameter from $t = 900$ to 1150 au.

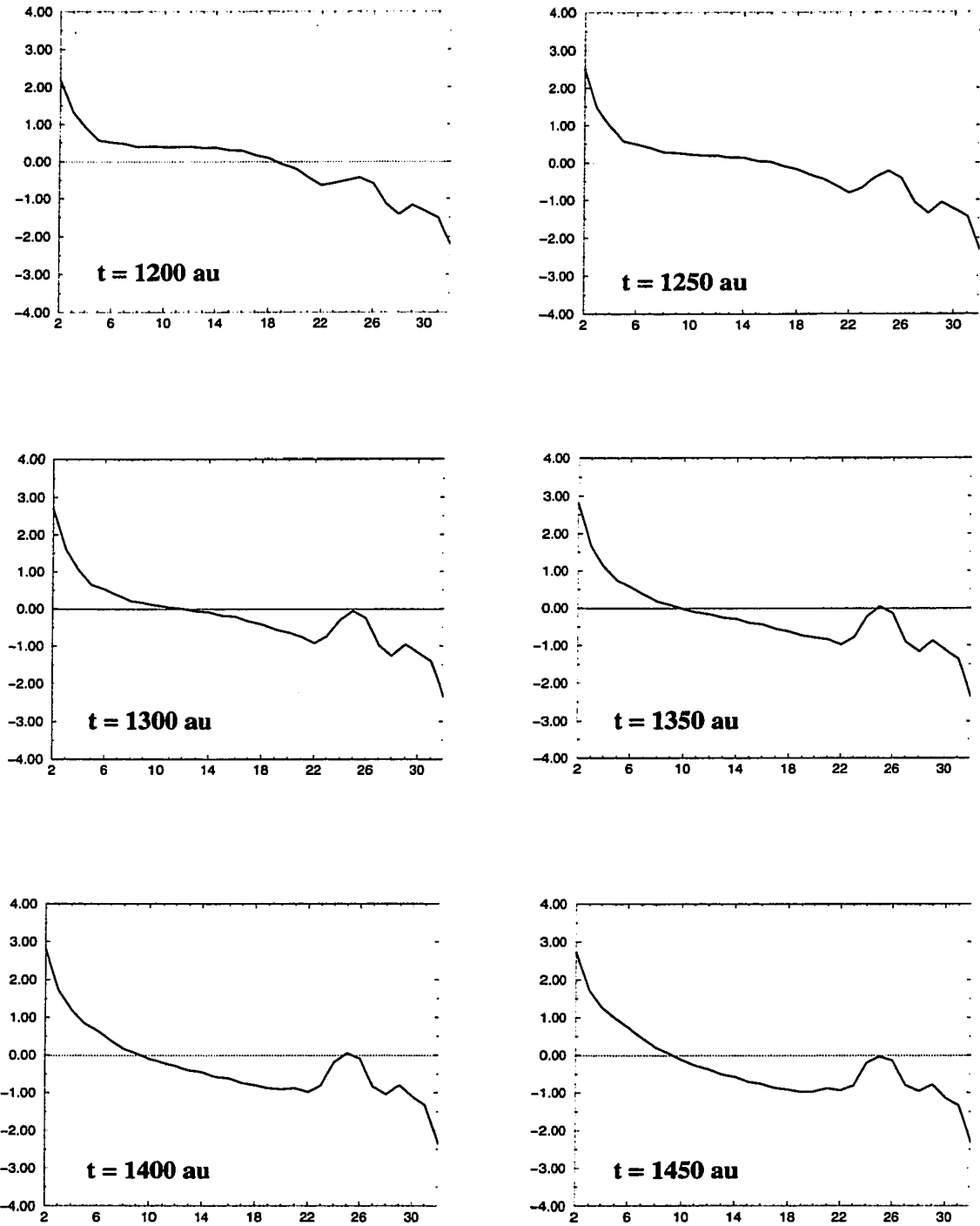


FIG. 27: Order parameter from $t = 1200$ to 1450 au.

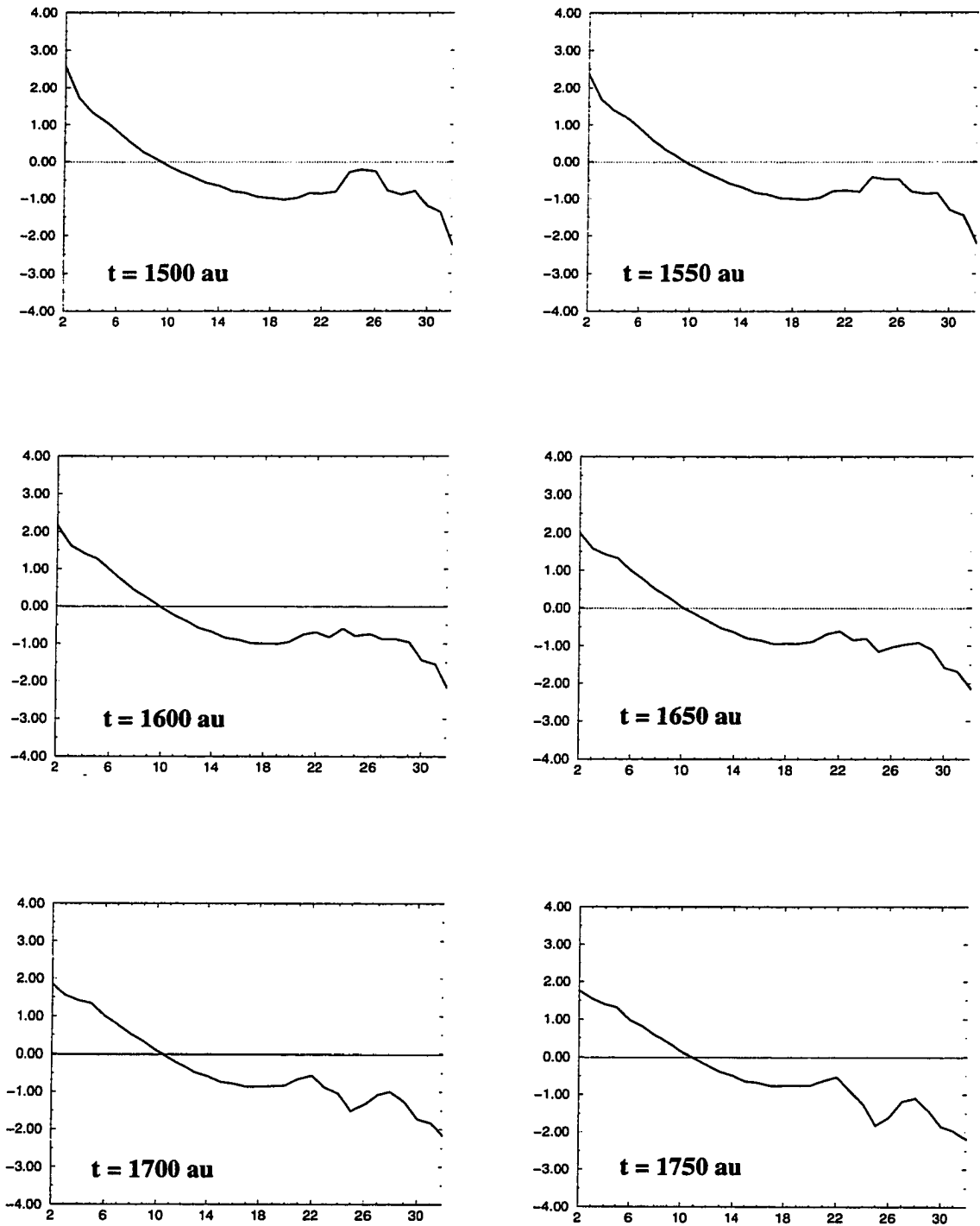


FIG. 28: Order parameter from $t = 1500$ to 1750 au.

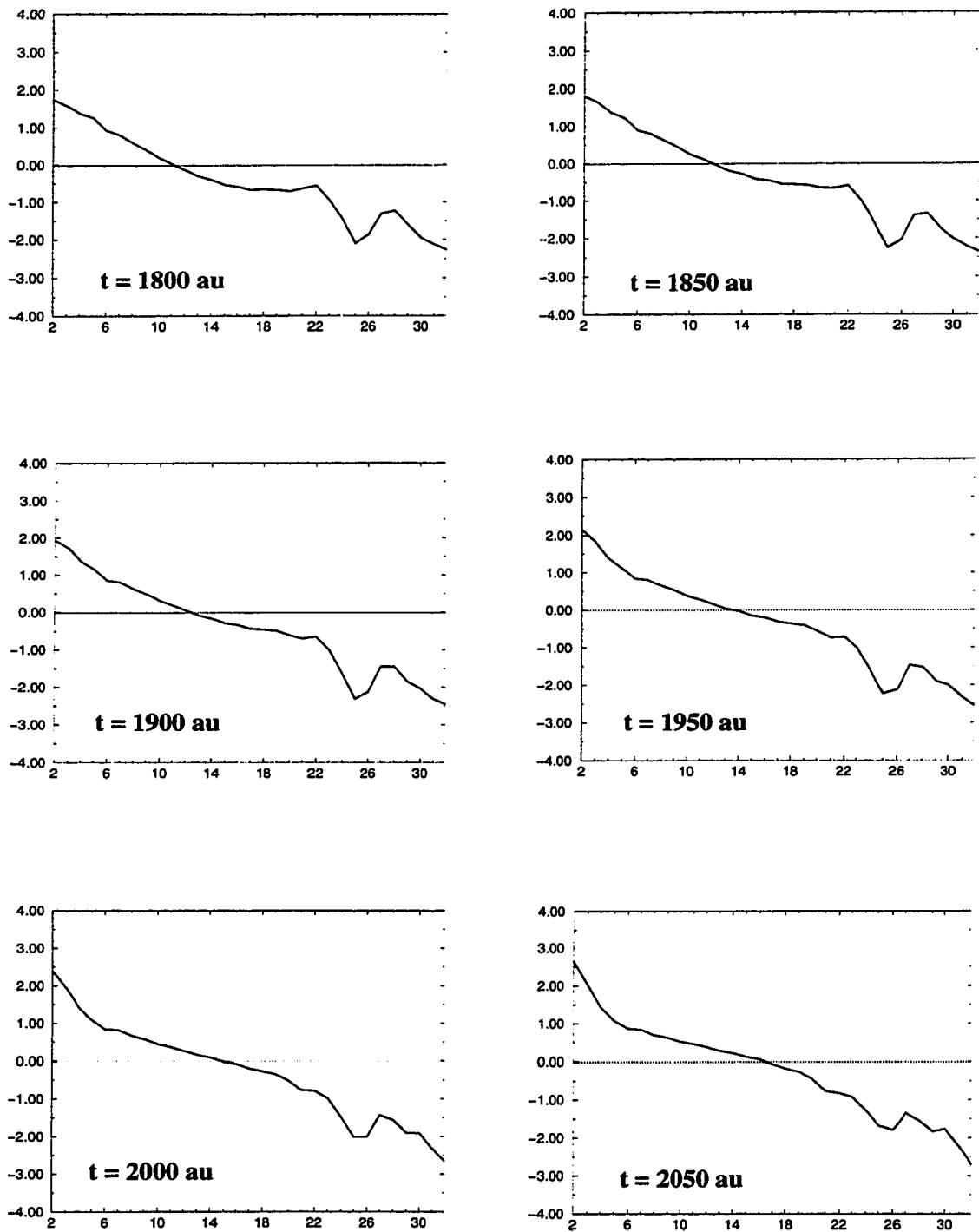


FIG. 29: Order parameter from $t = 1800$ to 2050 au.

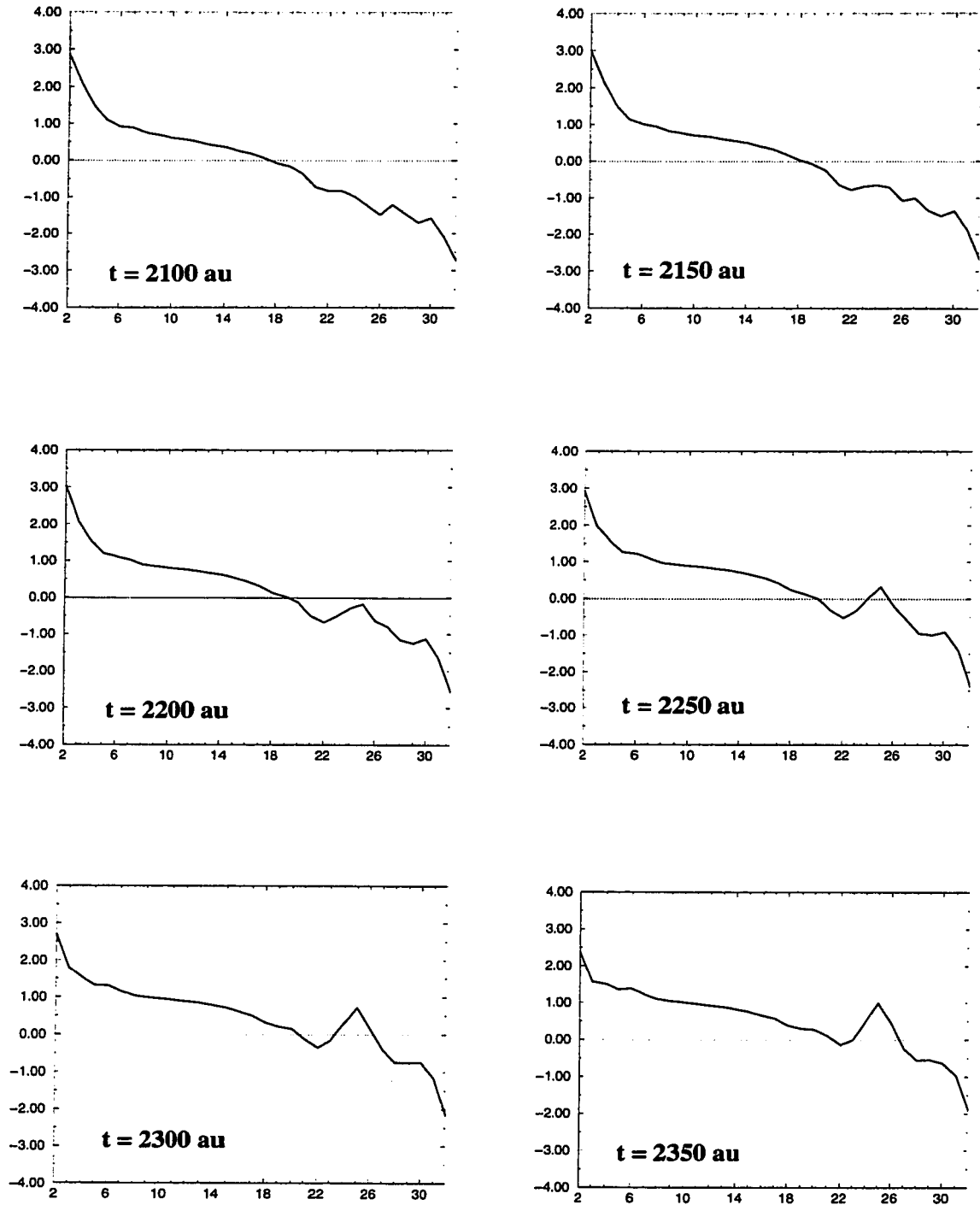


FIG. 30: Order parameter from $t = 2100$ to 2350 au.

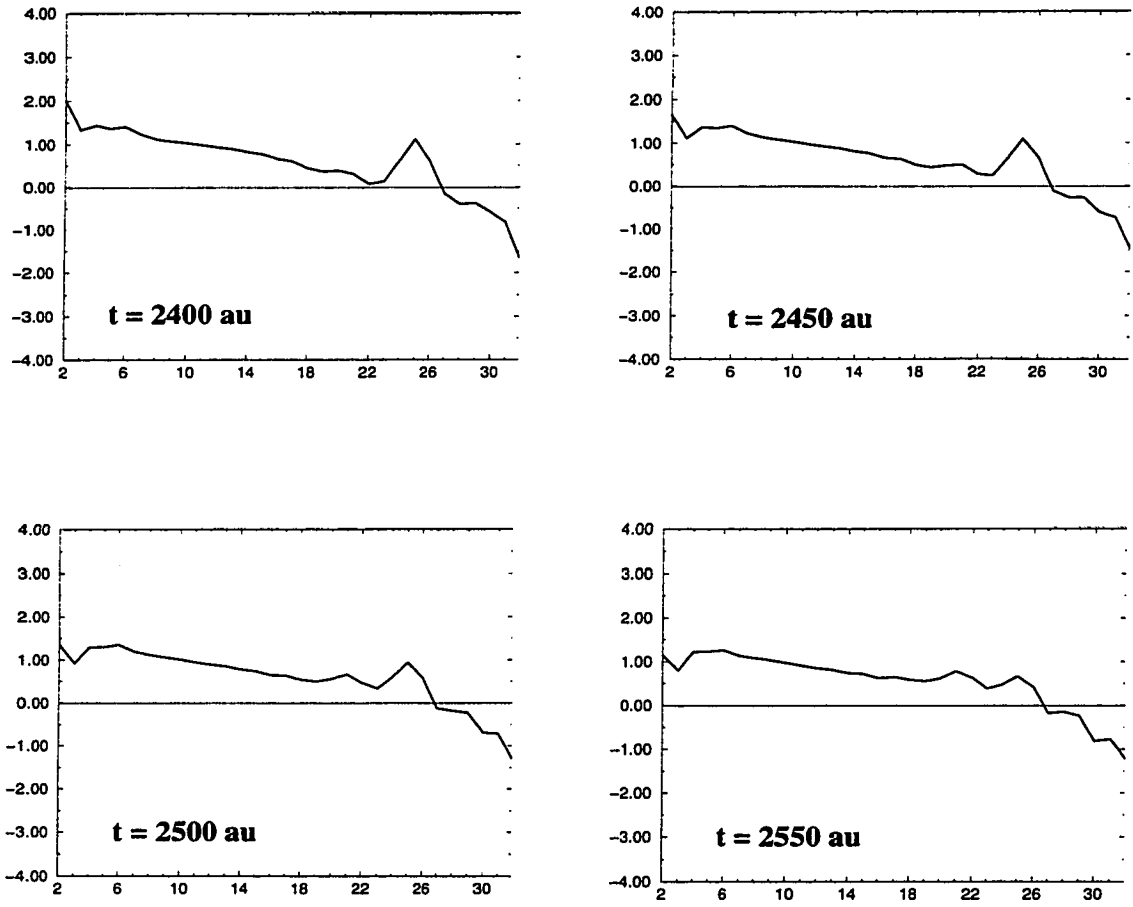


FIG. 31: Order parameter from $t = 2400$ to 2550 au.

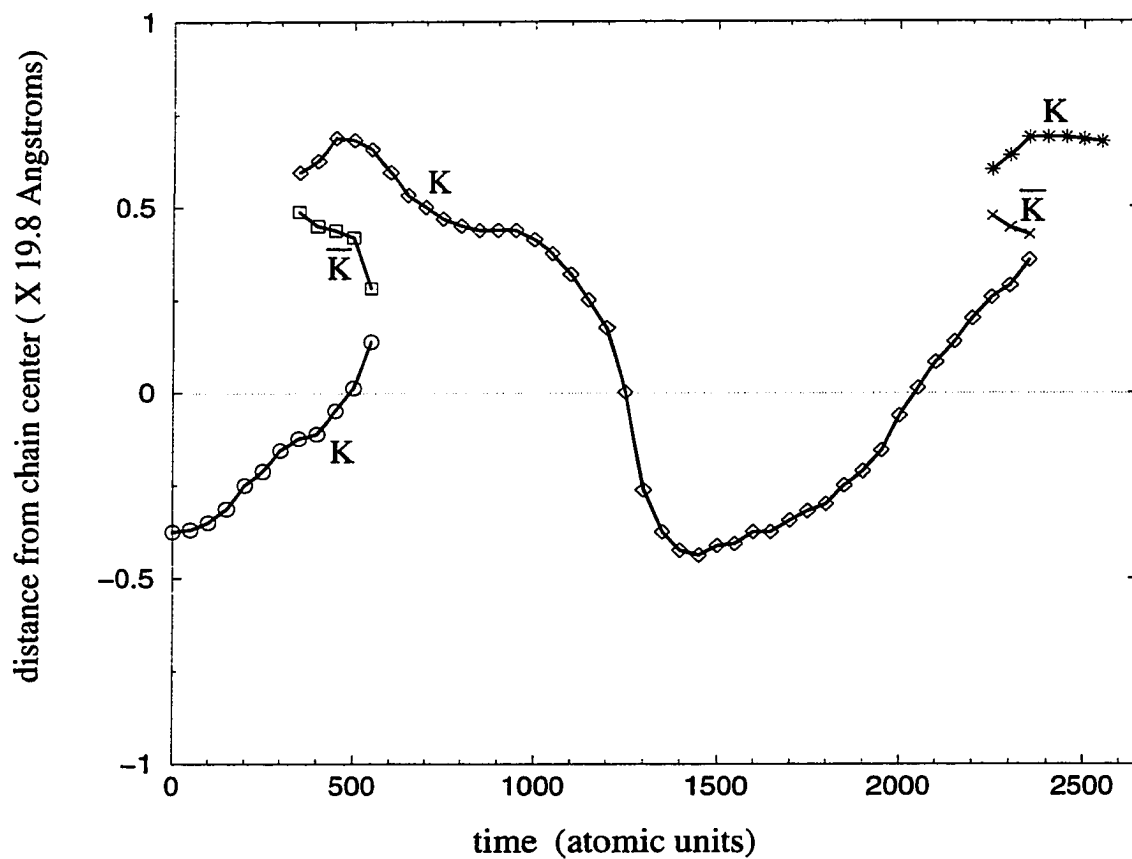


FIG. 32: Position of each kink and antikink vs. time.

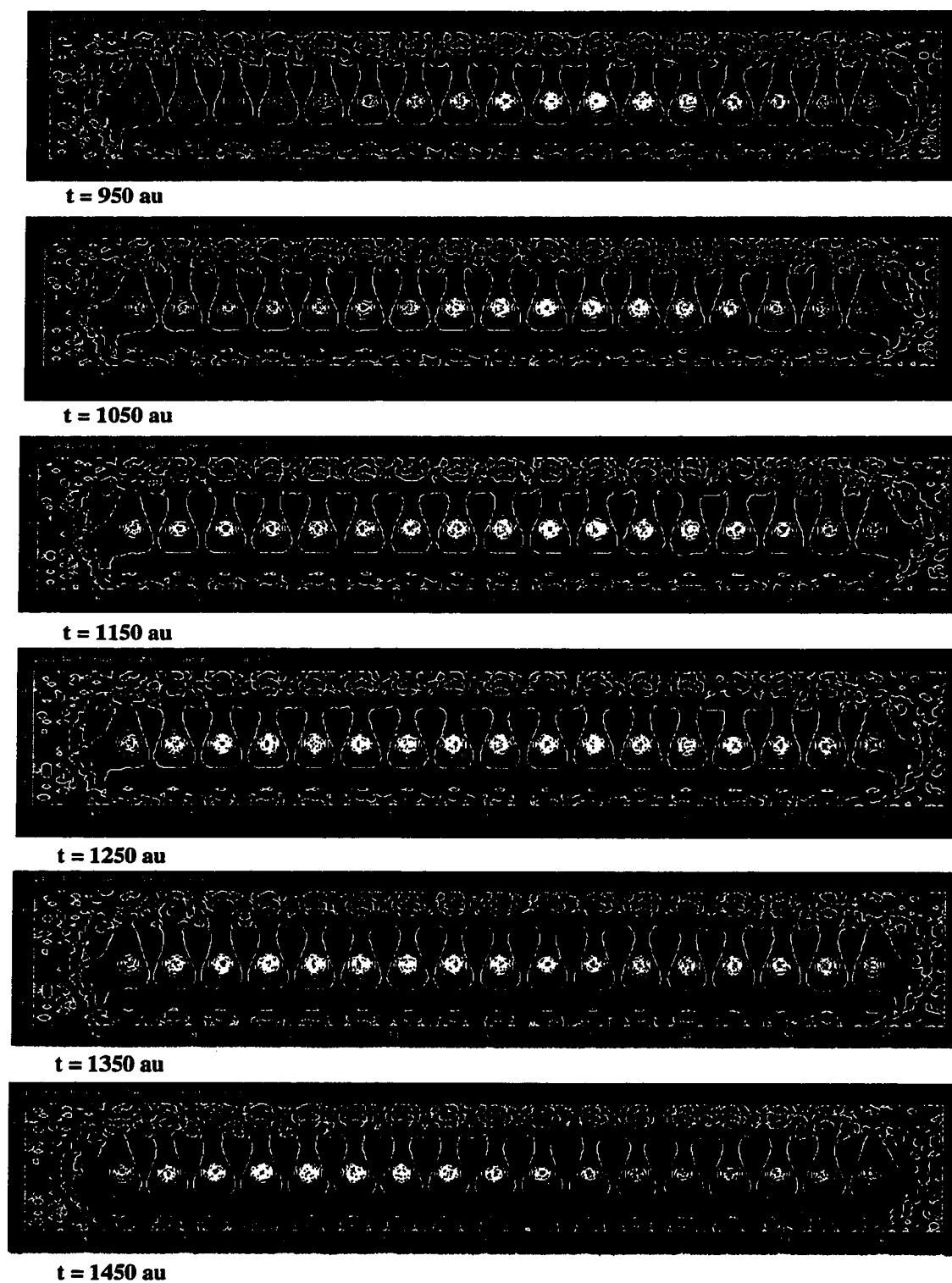


FIG. 33: Spin-polarization density 1 au above the plane of the polyene.

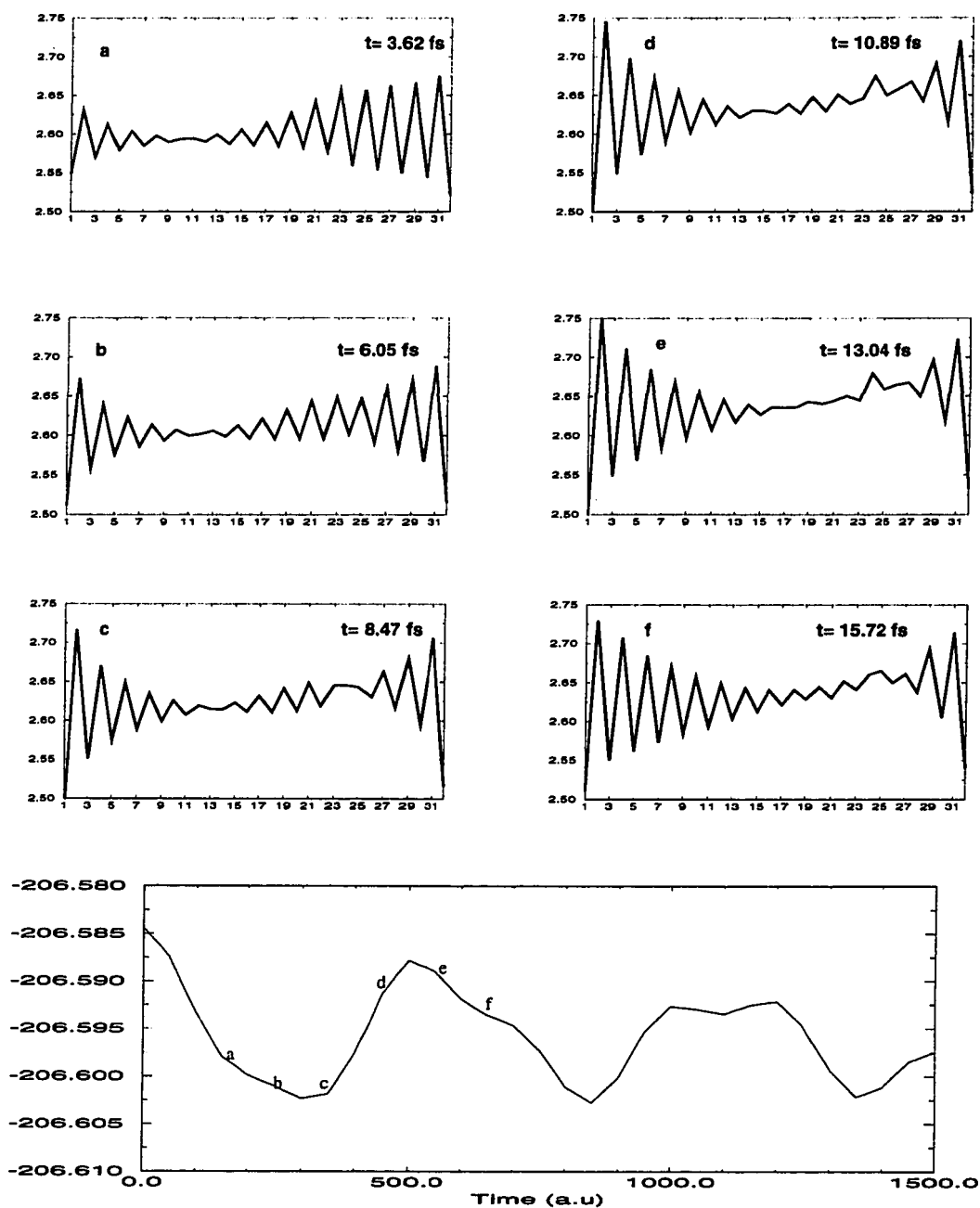


FIG. 34: Potential energy and carbon-carbon bond lengths for times shown.

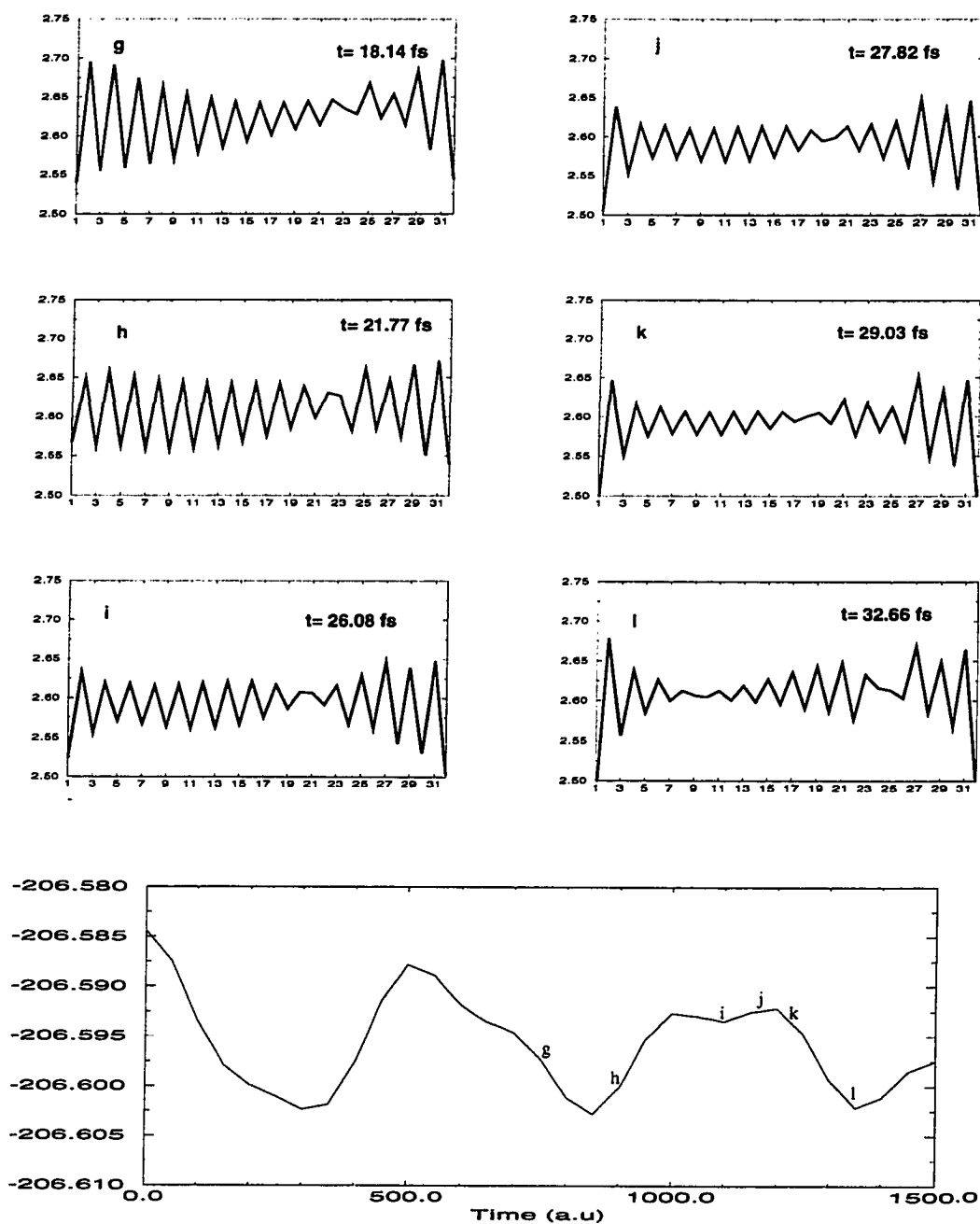


FIG. 35: Potential energy and carbon-carbon bond lengths for times shown.

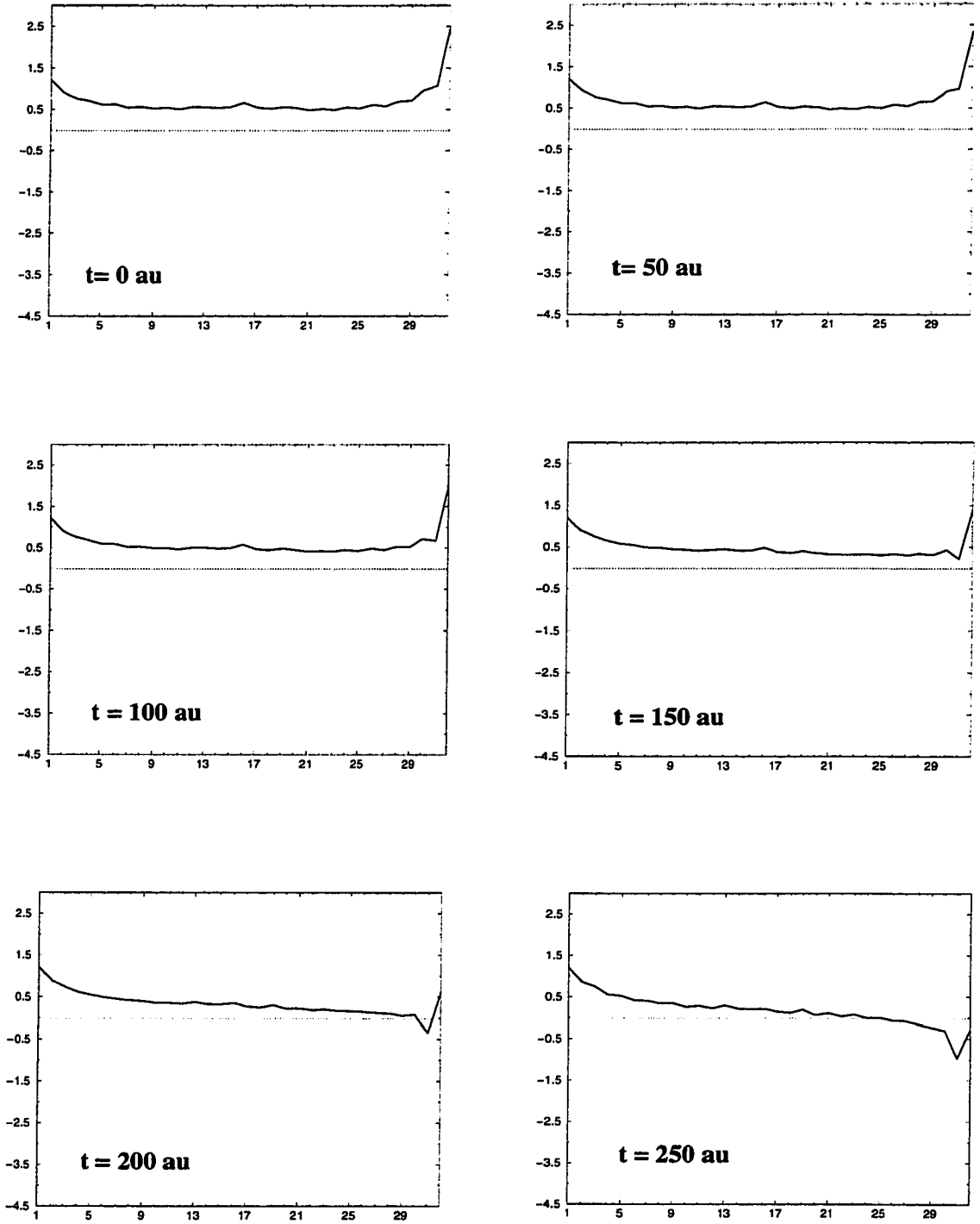


FIG. 36: Order parameter from $t = 0$ to 250 au.

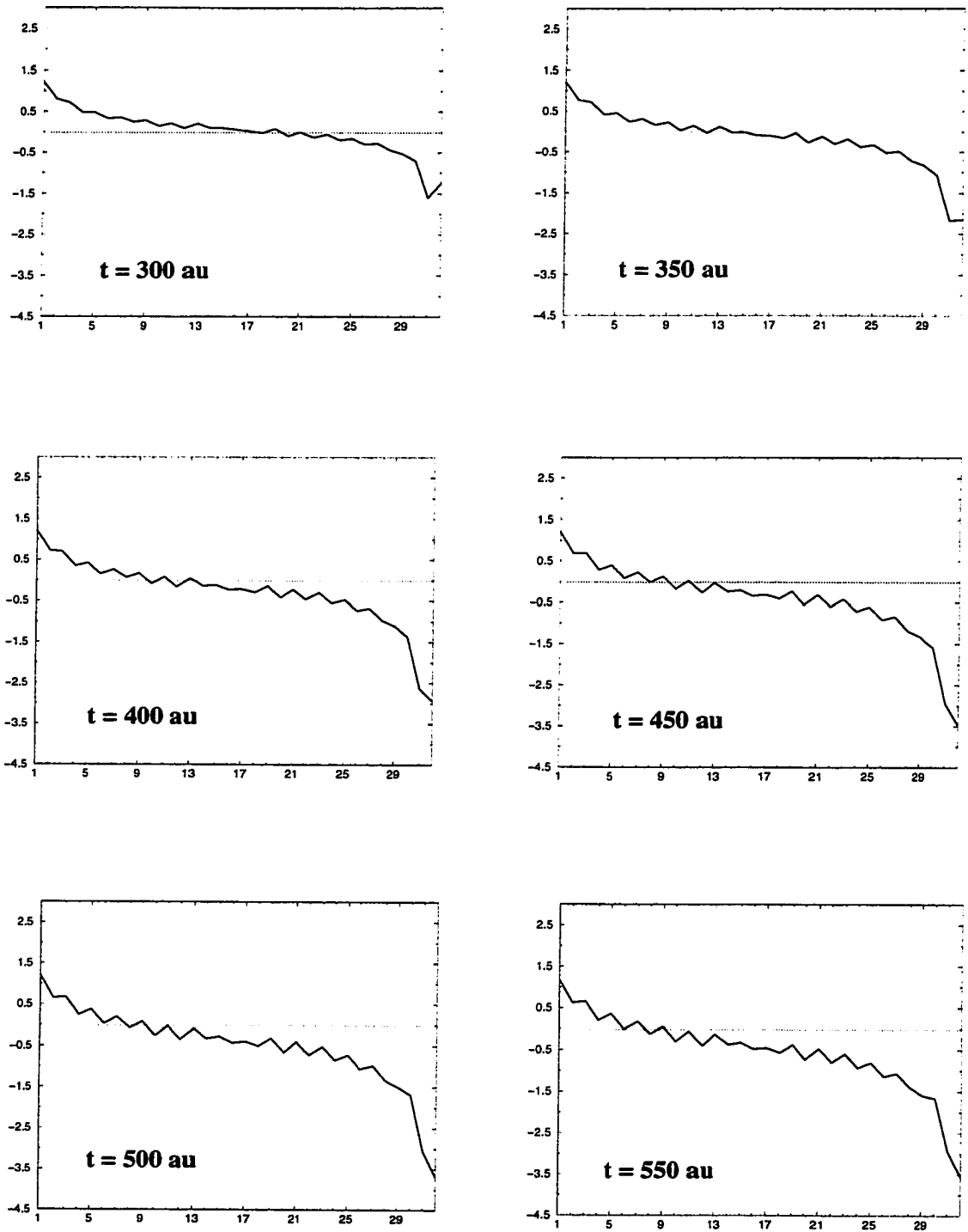


FIG. 37: Order parameter from $t = 300$ to 250 au.

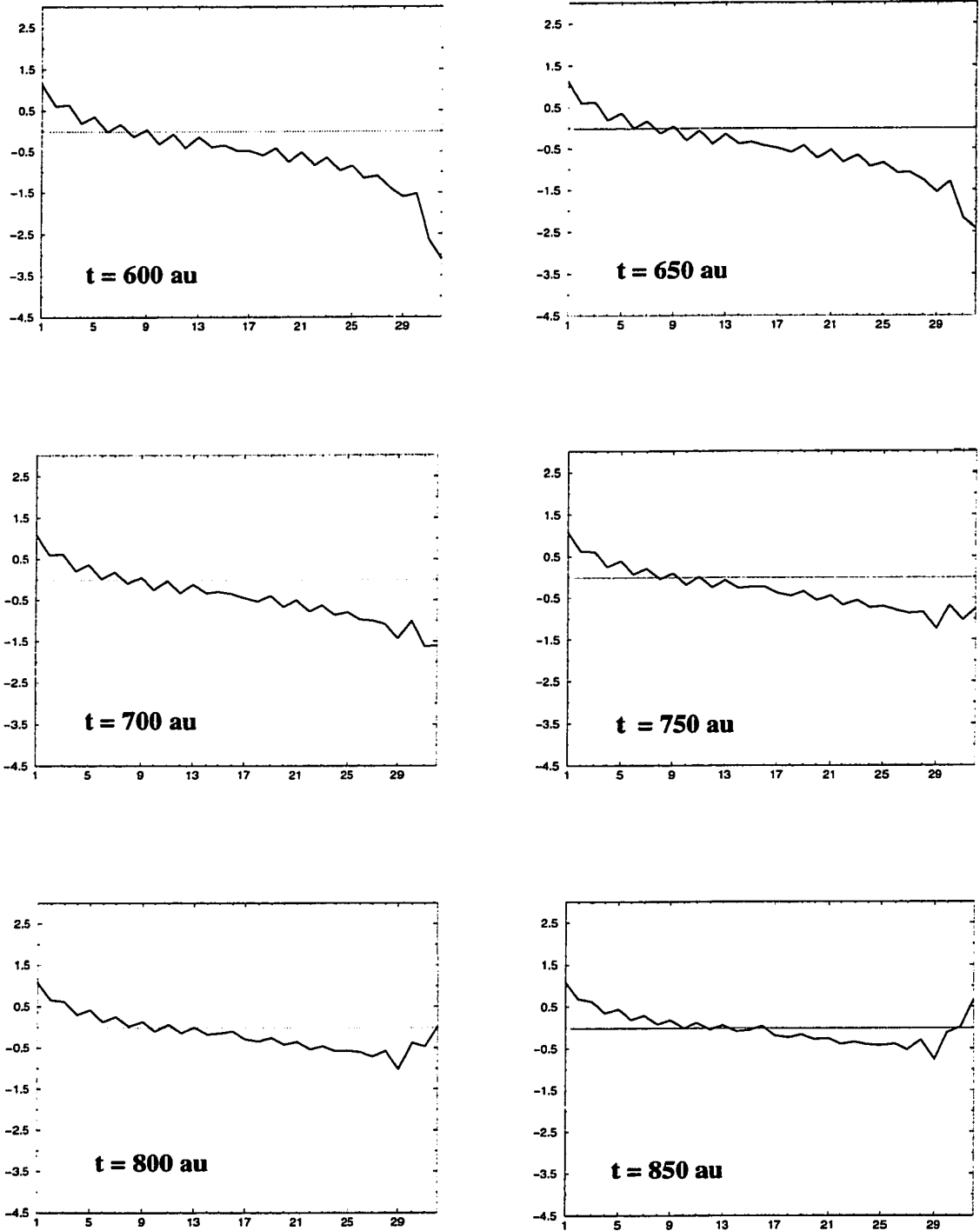


FIG. 38: Order parameter from $t = 600$ to 850 au.

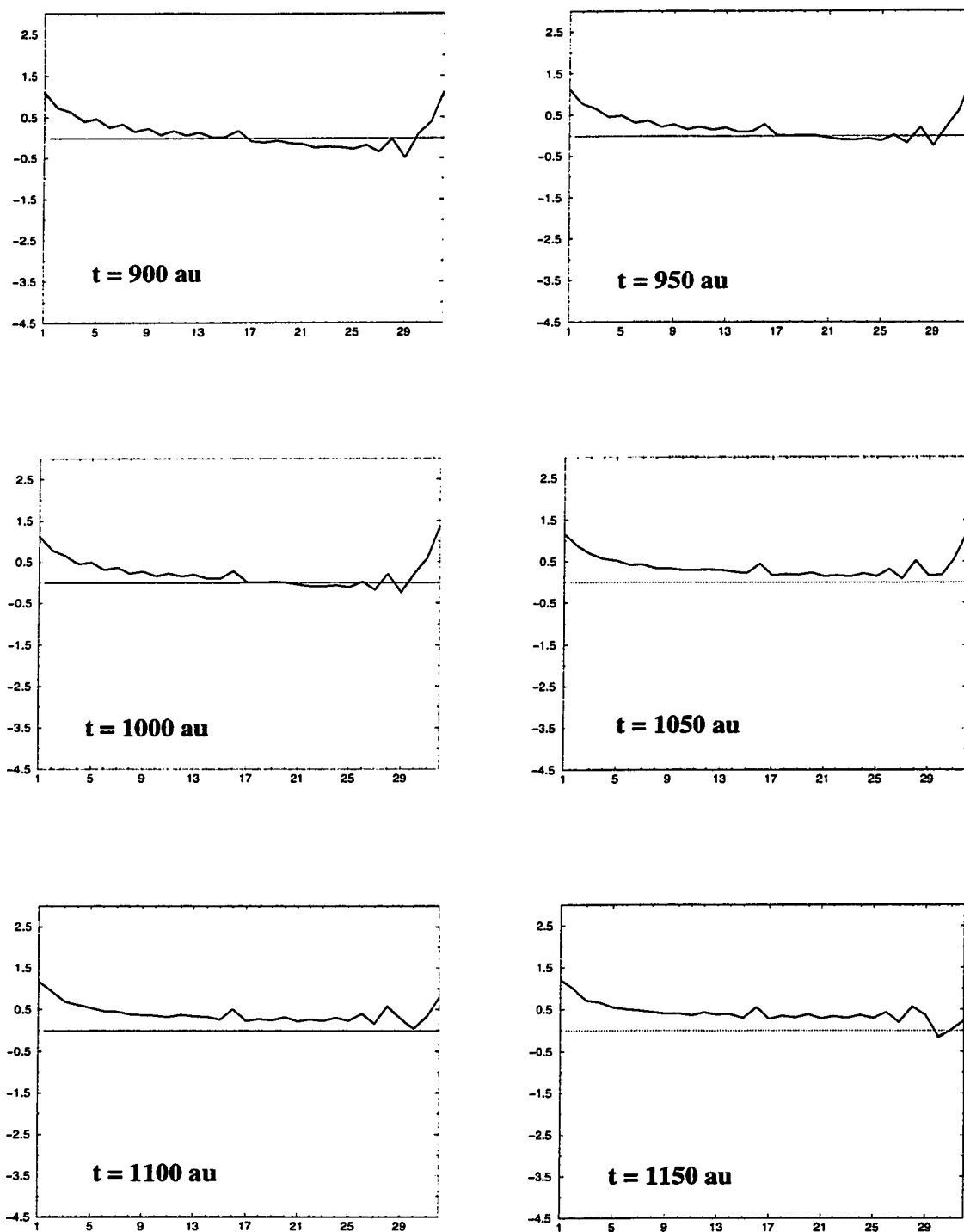


FIG. 39: Order parameter from $t = 900$ to 1150 au.

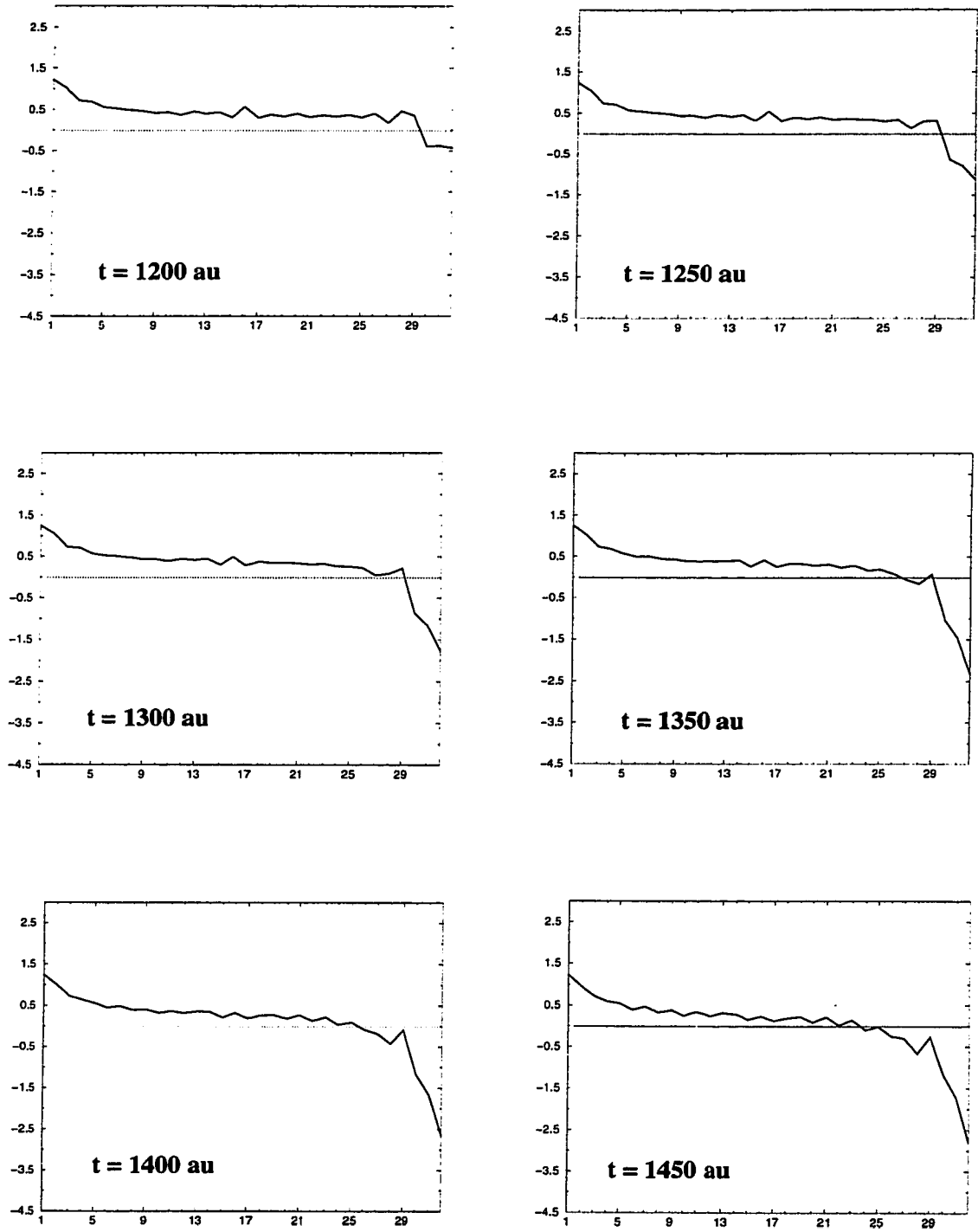


FIG. 40: Order parameter from $t = 1200$ to 1450 au.

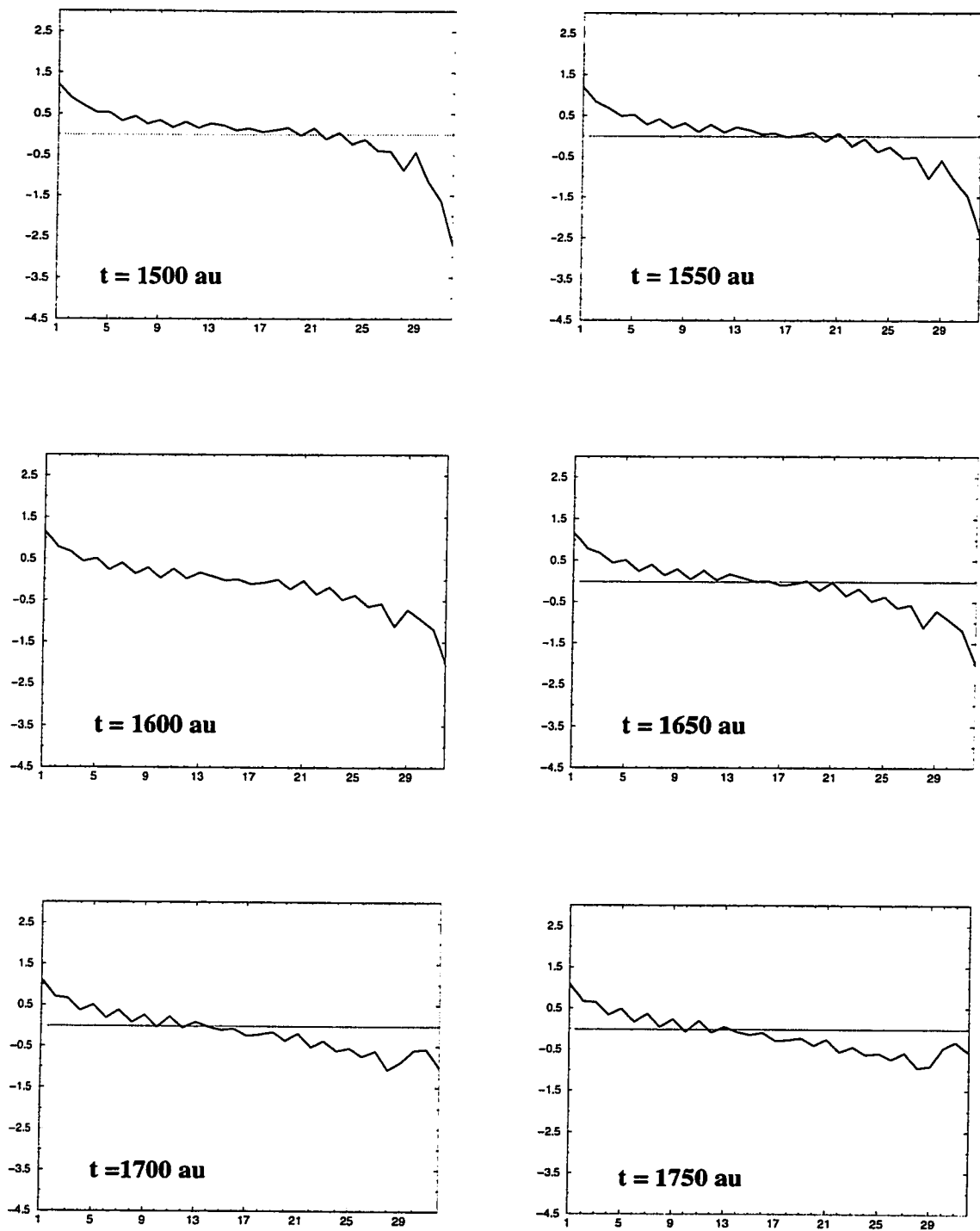


FIG. 41: Order parameter from $t = 1500$ to 1750 au.

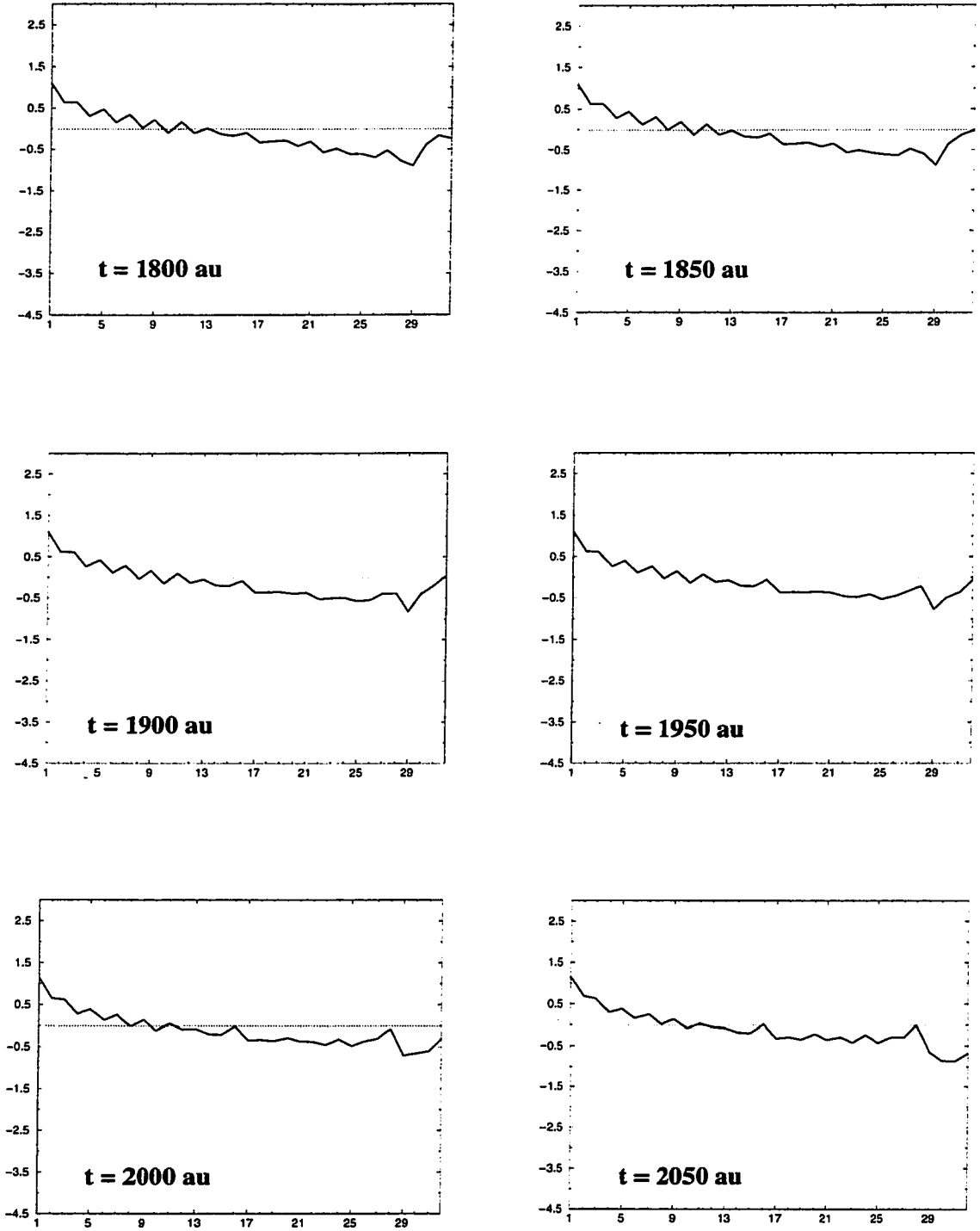


FIG. 42: Order parameter from $t = 1800$ to 2050 au.

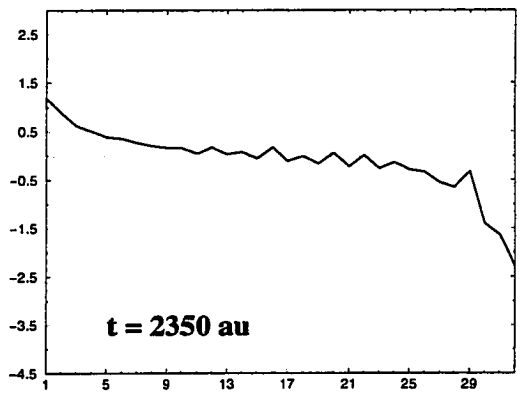
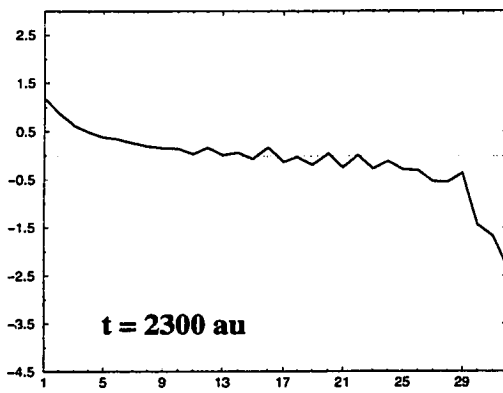
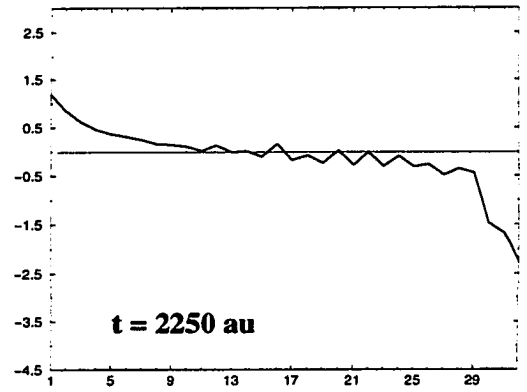
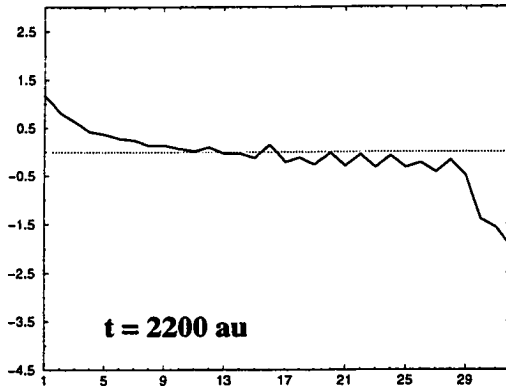
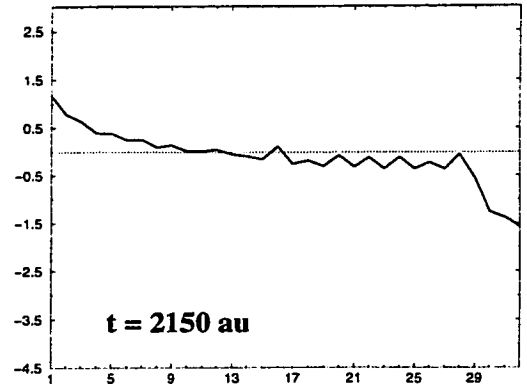
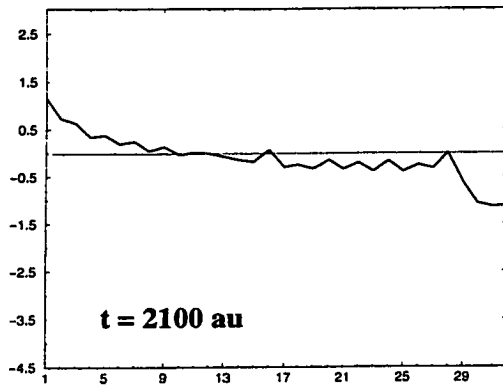


FIG. 43: Order parameter from $t = 2100$ to 2350 au.

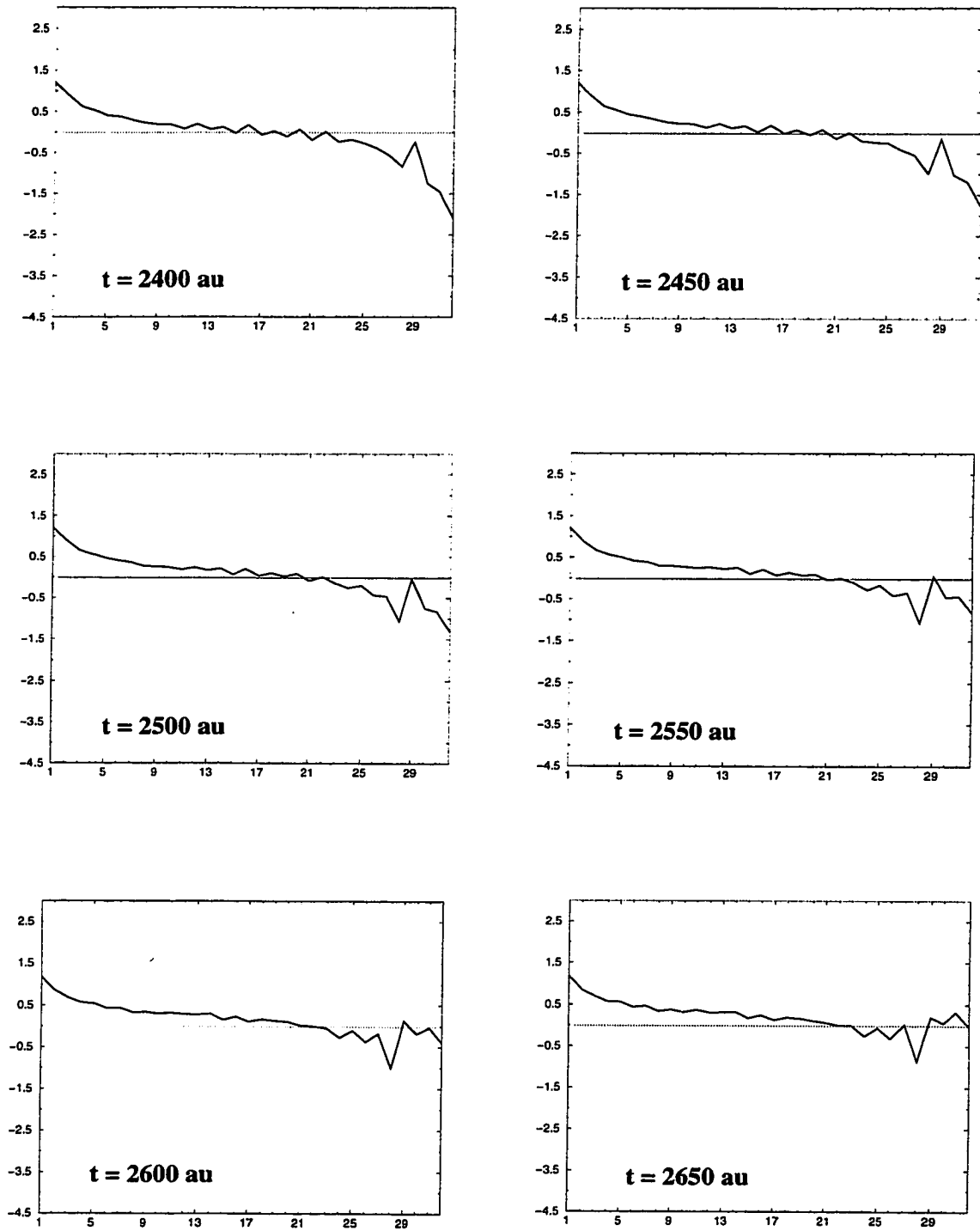


FIG. 44: Order parameter from $t = 2400$ to 2650 au.



FIG. 45: HOMO level density 1 au above polyene at $t = 0$.

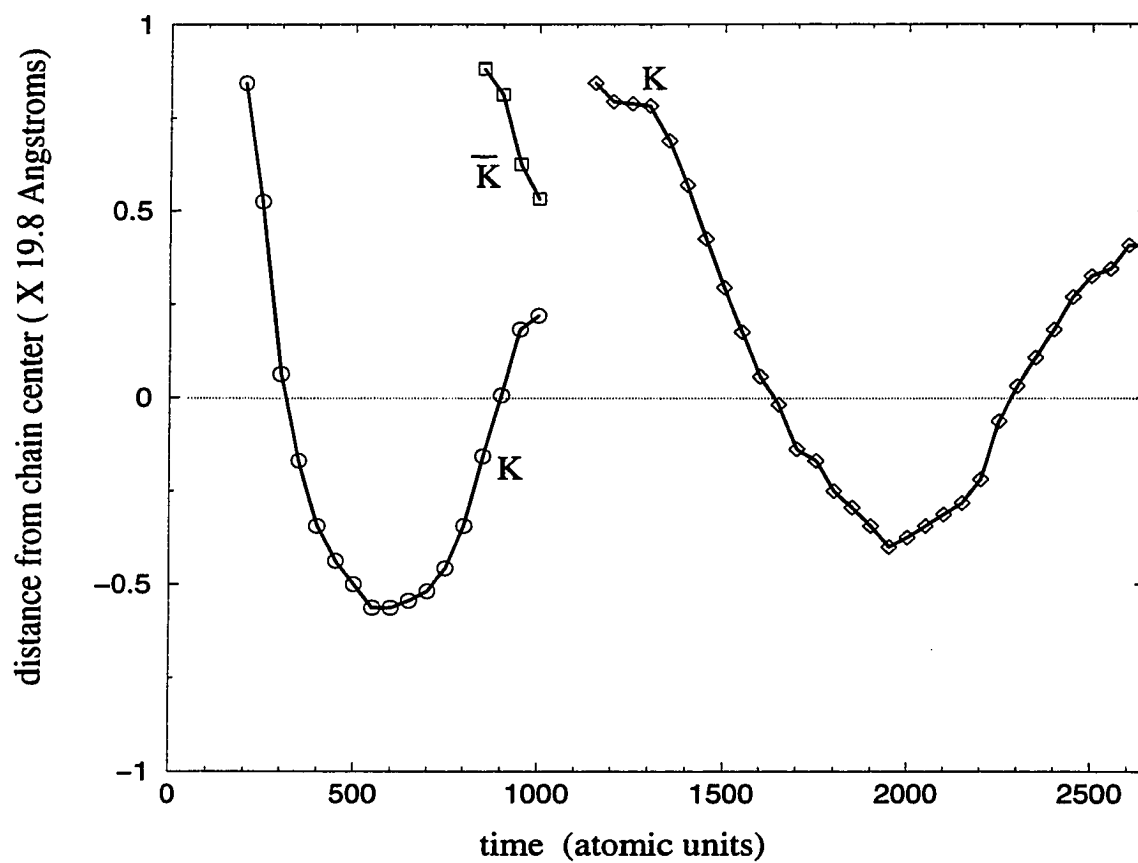
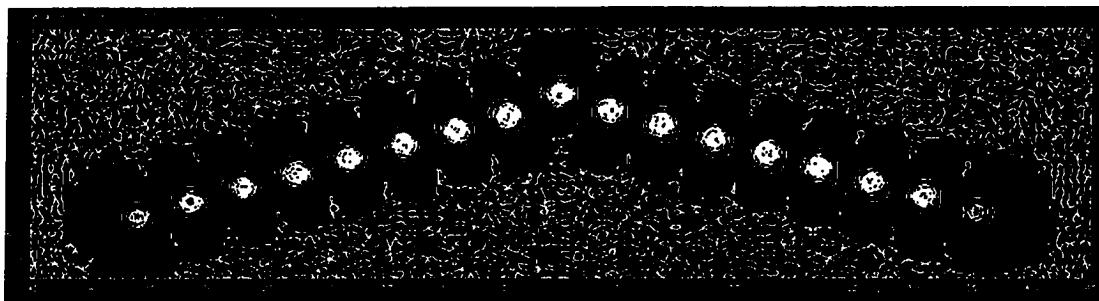
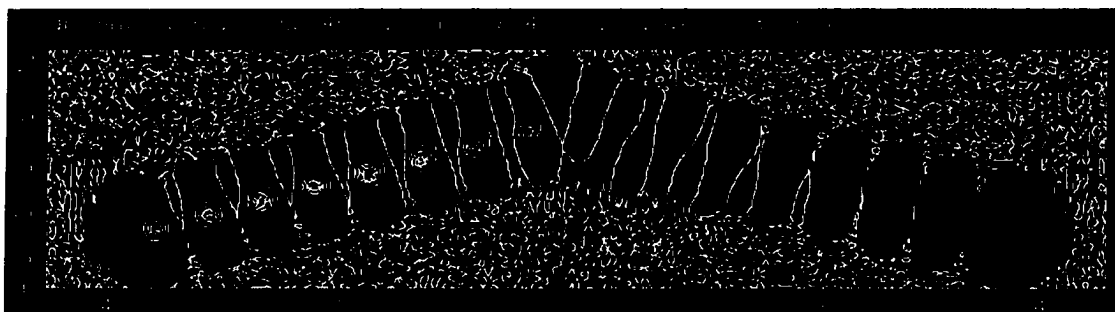


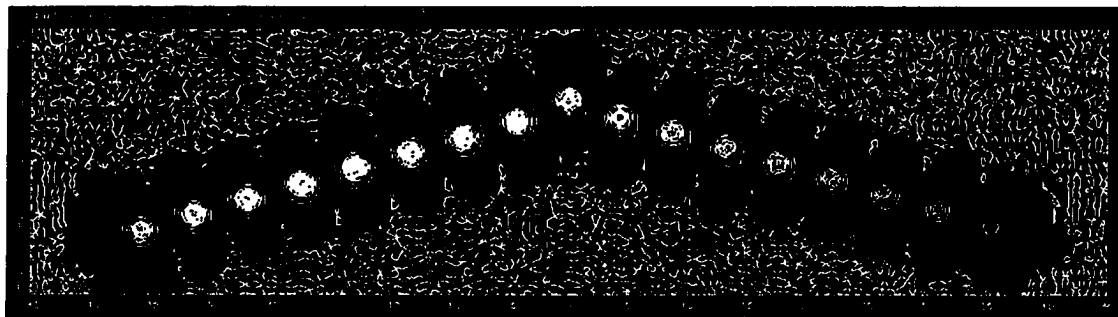
FIG. 46: Position of each kink and antikink vs. time.



HOMO density: $t=350$ au

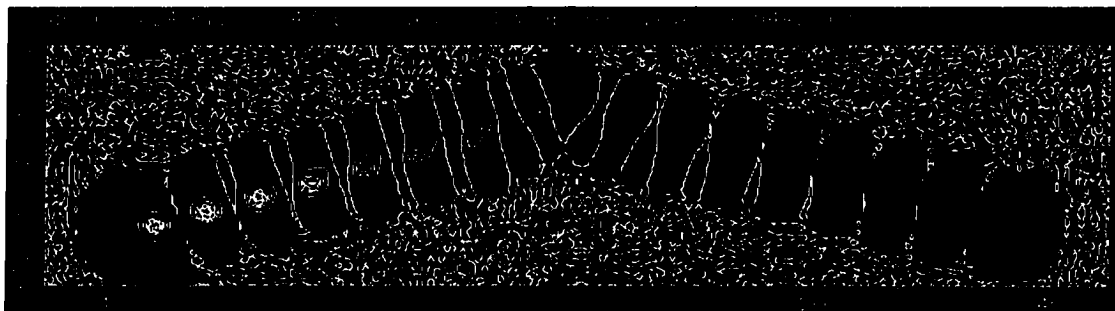


Change in HOMO density: $t=350-450$ au

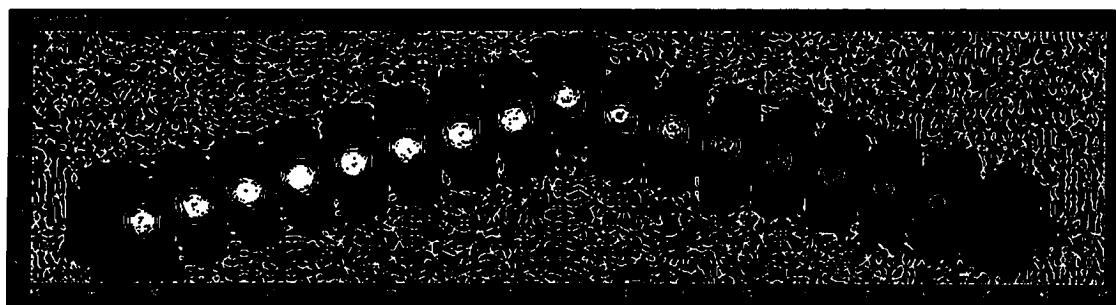


HOMO density: $t=450$ au

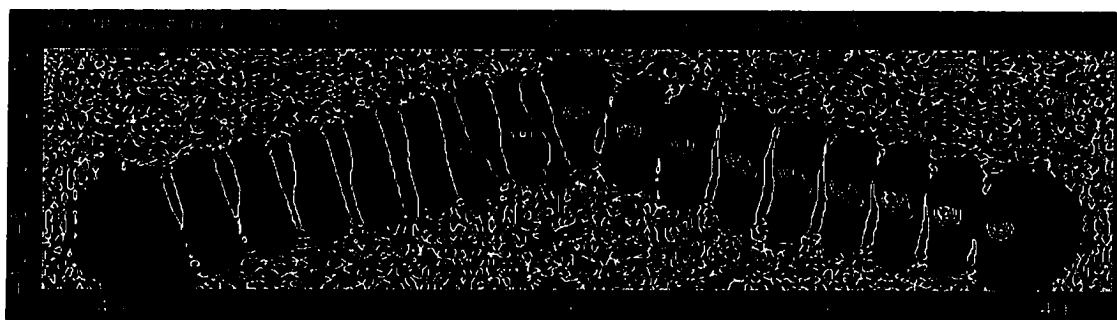
FIG. 47: HOMO density and change for times specified and change in HOMO density between times specified 1 au above the plane of the polyene.



Change in HOMO density: $t = 450-550$ au

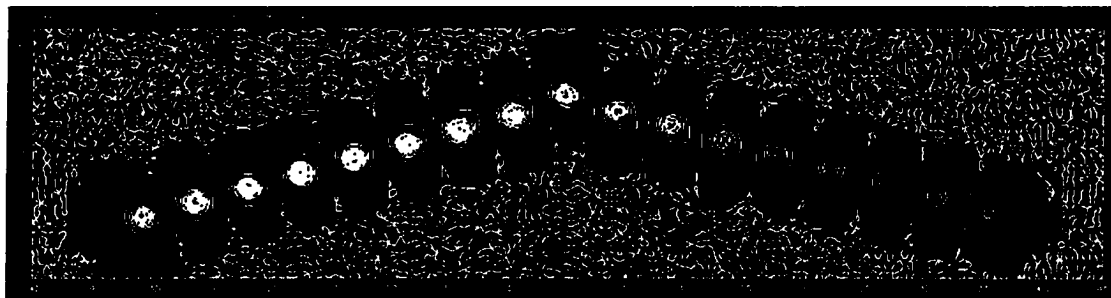


HOMO density: $t = 550$ au

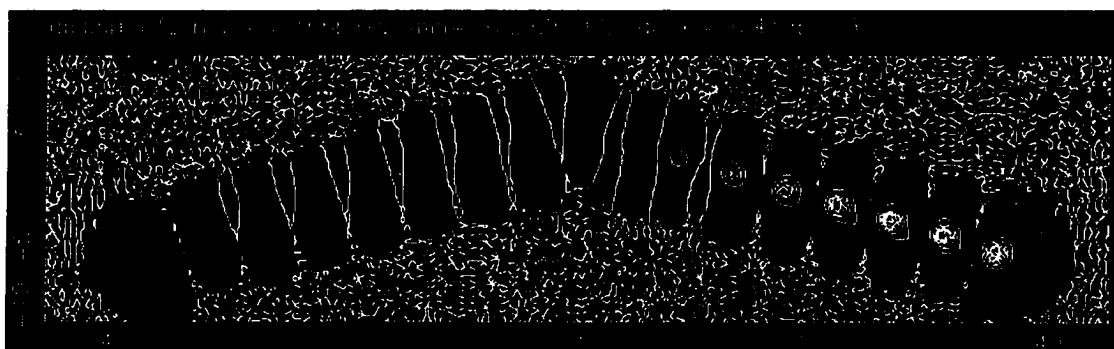


Change in HOMO density: $t = 550-650$ au

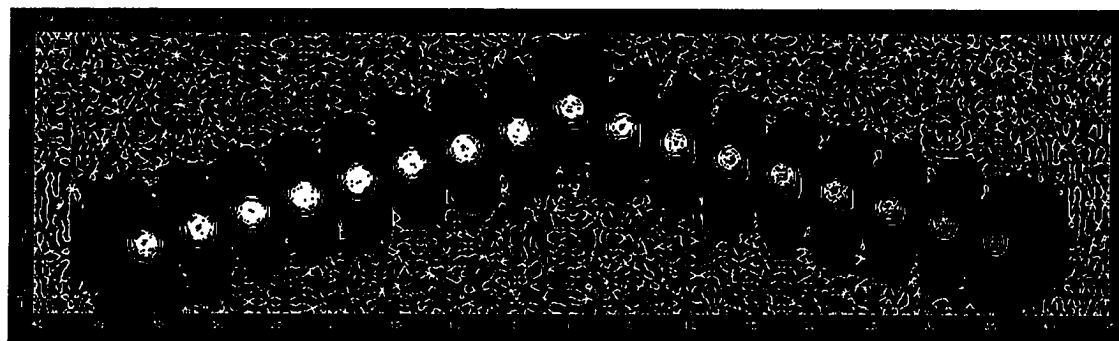
FIG. 48: HOMO density and change for times specified and change in HOMO density between times specified 1 au above the plane of the polyene.



HOMO density: $t = 625$ au



Change in HOMO density: $t = 625-725$ au

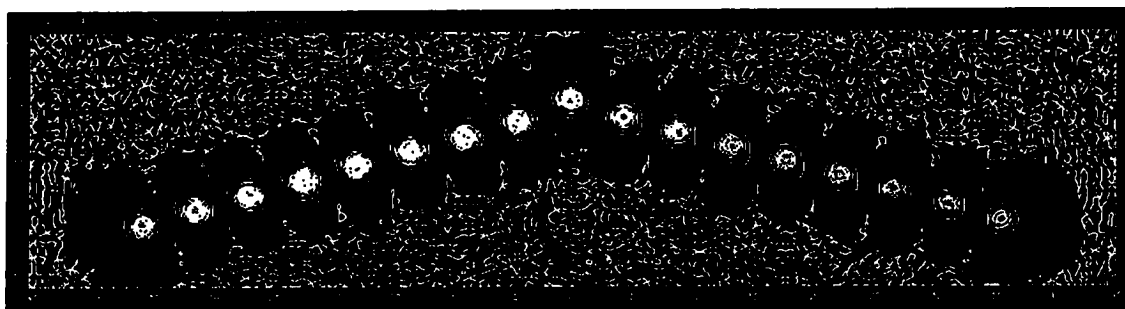


HOMO density: $t = 725$ au

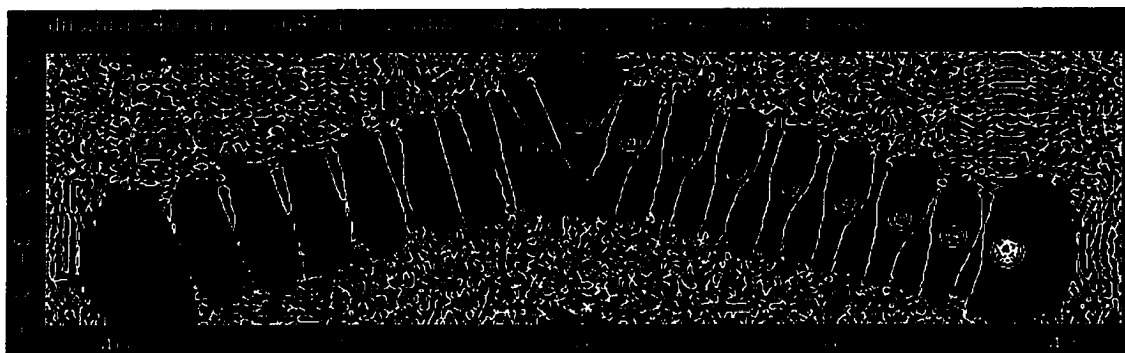
FIG. 49: HOMO density and change for times specified and change in HOMO density between times specified 1 au above the plane of the polyene.



Change in HOMO density: $t = 725-825$ au

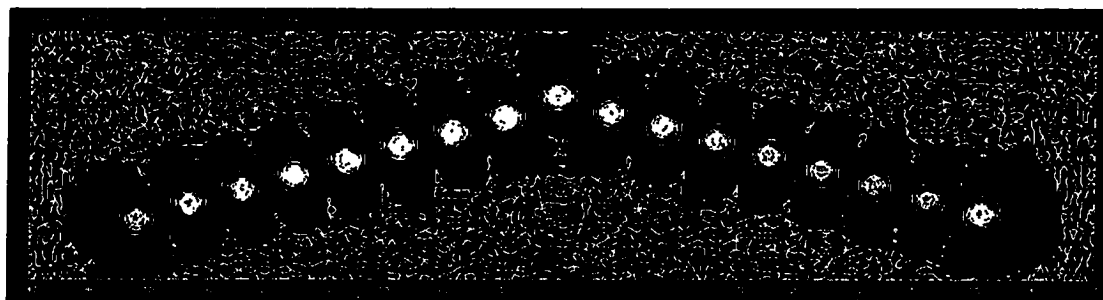


HOMO density: $t = 825$ au

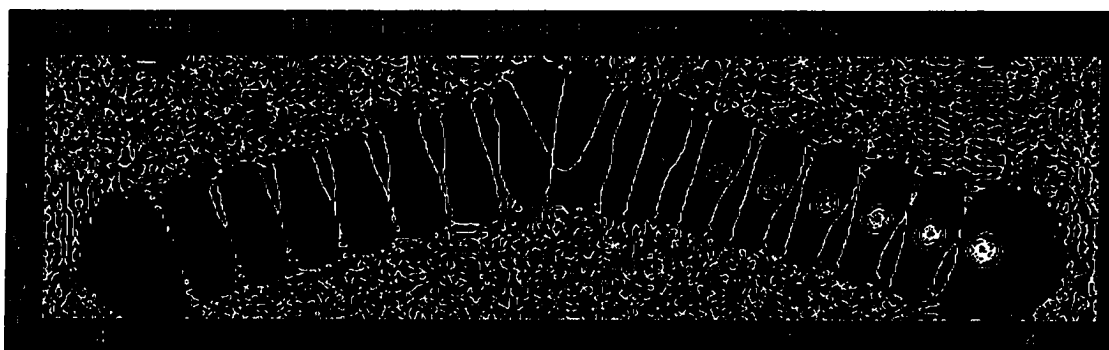


Change in HOMO density: $t = 825-925$ au

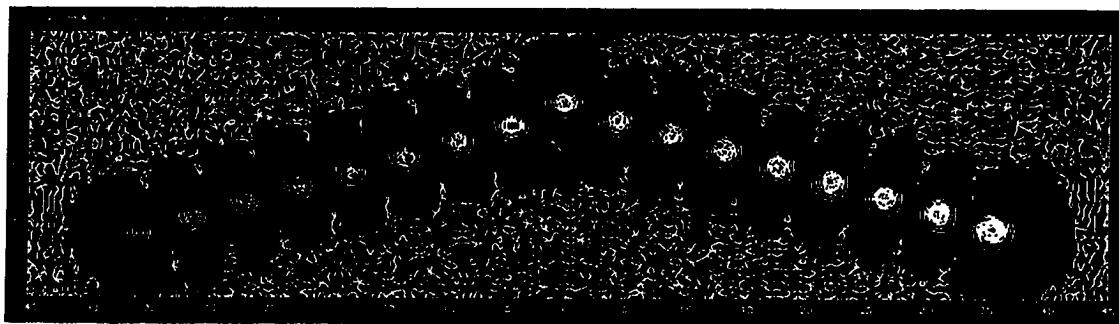
FIG. 50: HOMO density and change for times specified and change in HOMO density between times specified 1 au above the plane of the polyene.



HOMO density: $t = 925$ au



Change in HOMO density: $t = 925-1025$ au



HOMO density: $t = 1025$ au

FIG. 51: HOMO density and change for times specified and change in HOMO density between times specified 1 au above the plane of the polyene.

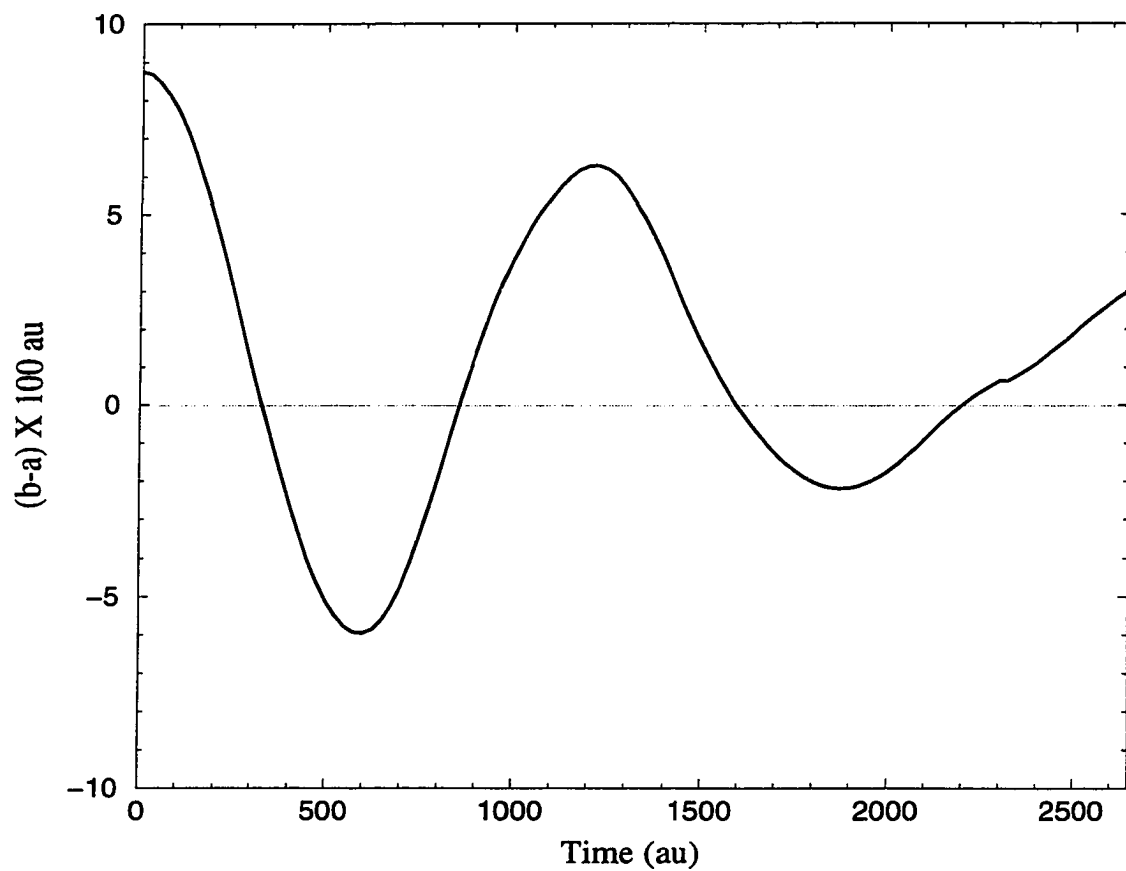


FIG. 52: Difference in bond length between horizontal *cis* bond (of length “b”) and adjacent bond (of length “a”) vs. time.

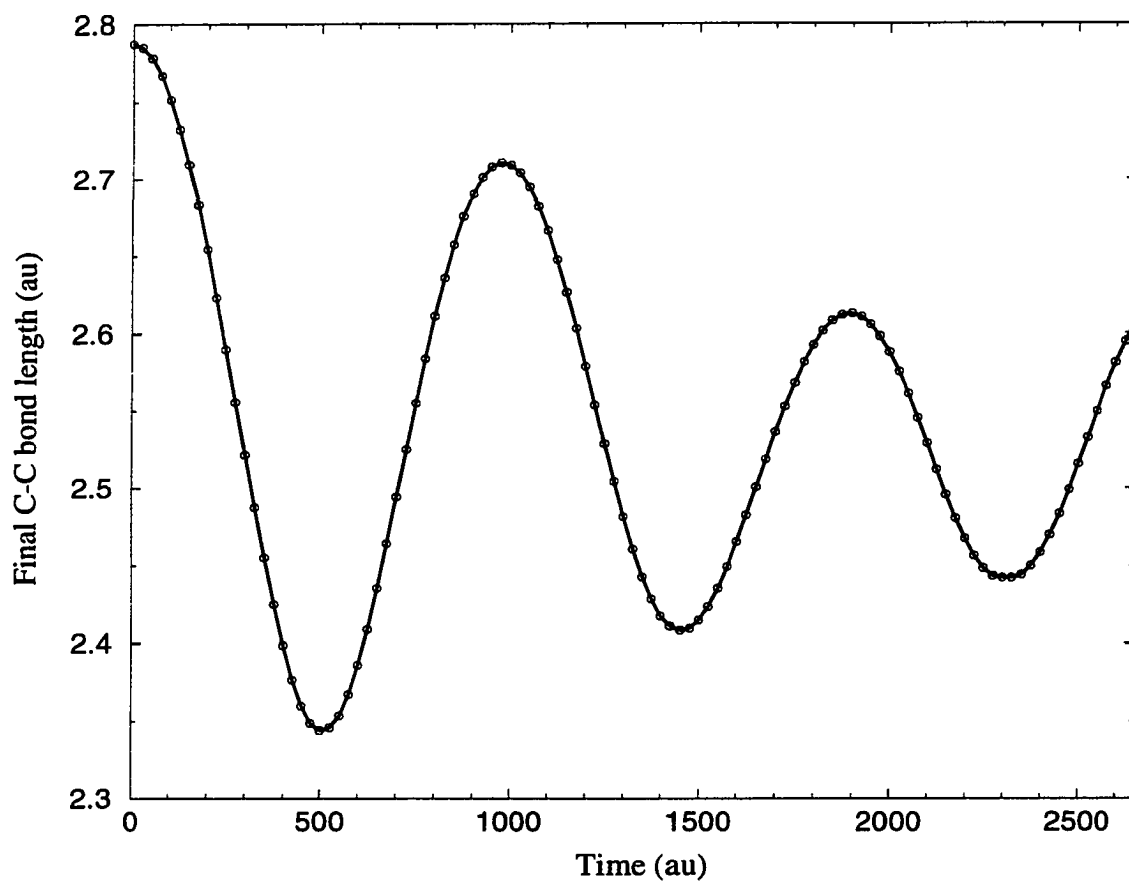


FIG. 53: Bond length of terminal carbon-carbon bond vs. time.

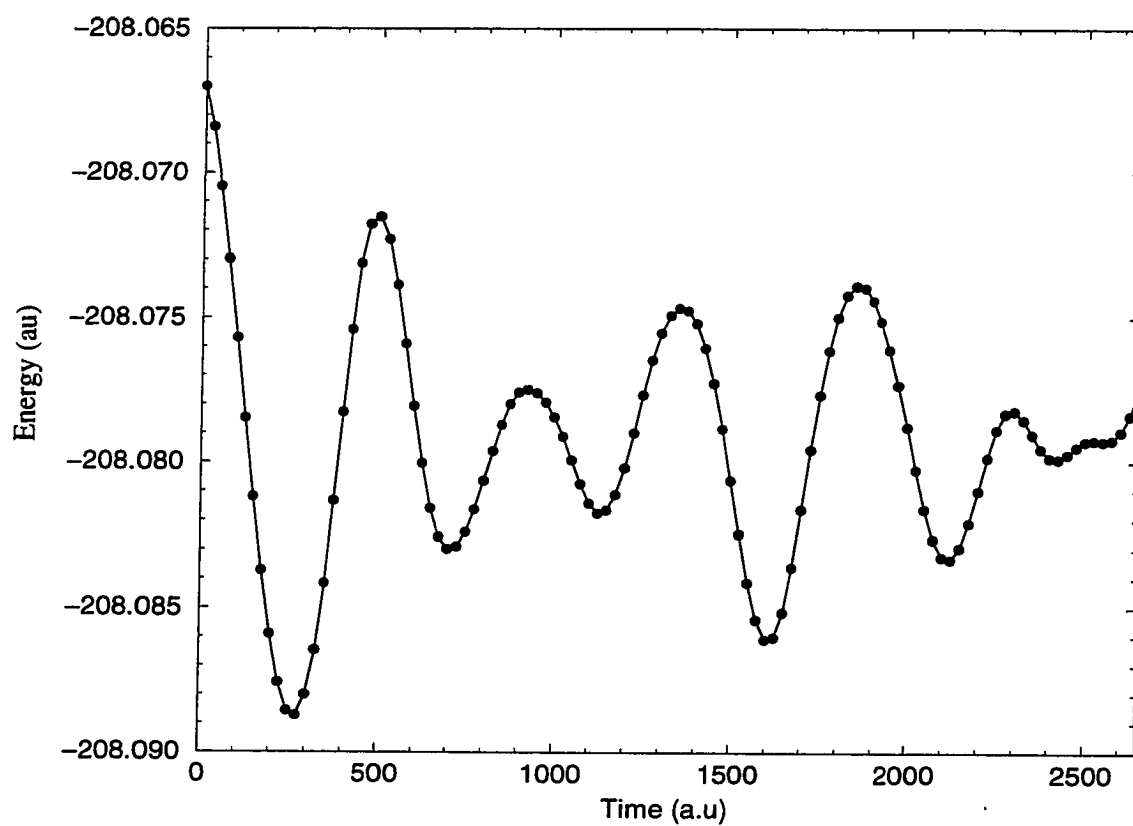


FIG. 54: Change in potential energy vs. time for polyene with *cis* bond.

7 CONCLUSIONS

We list here some general conclusions from this study of PA and mobile solitons in finite polyenes.

(a) My study of the infinite PA system using a supercell method and a plane-wave basis set with LDA finds that the dimerization is underestimated by about 25% when a supercell containing 32 carbon atoms is used. The use of a gradient correction to the LDA using functionals of Becke [26] and Perdew [27] does not improve agreement to experiment. These results agree with other previous calculations. Suhai [19] has reported that the use of a more recently proposed gradient-corrected functional designed by Becke leads to predicted dimerization within 2% of the experimental value. It may be of interest to use this functional in future dynamics studies to see if there are significant changes to the dynamical behavior.

(b) I find that polyenes of *trans*-PA (C_nH_{n+2}) have a dimerization nearly half of the experimental value for the infinite PA system for even-membered polyenes. I find a soliton structure for the ground state of odd-membered polyenes. The geometric width of the soliton predicted by this LDA method is at least twice that predicted by others using a Hartree-Fock method.

(c) I initiate soliton dynamics simulations with Car-Parrinello ab initio molecular dynamics by using an initial distortion of the ground state geometry that has a soliton structure off-center or near the polyene end. I find the average speed of solitons started from these geometries to be about 1.0×10^5 m/s. This is about 5 to 10 times faster than speeds reported from model calculations using similar geometry distortions to start simulations. Unlike simulations such as those by Su et al. which use the popular SSH Hamiltonian, I find the velocity varies with position along the

chain and noticeably decreases with time. The results here seem to indicate that negatively charged solitons move with a slightly higher velocity than neutral solitons with the same geometrical initial conditions.

(d) Inspection of the potential energy change during dynamics reveals that the soliton activation energy, or the energy required to translate the soliton to a nearest-neighbor site, is roughly estimated to be about 0.025 eV. This is about an order of magnitude greater than an estimate given by Su et al. which uses the SSH model and does not consider the effects of phonon interaction. My rough estimate of the effective mass is the same order of magnitude as values estimated from SSH and other models. This small effective mass indicates the need to treat the soliton as a quantum particle.

(e) From results of simulations of a charged soliton moving in a polyene with a central *cis* bond, I find that a soliton moving with a speed on the order of 10^5 m/s has enough kinetic energy for the soliton center to pass over the *cis* bond. The soliton charge density wave appears to stay coherent as the soliton moves back and forth across the *cis* region.

In summary, we have shown that LDA and Car-Parrinello molecular dynamics are useful tools for the study of mobile solitons in long polyenes. Due to the complexity of the bulk PA material, experimental information about the microscopic details of solitons is still inconclusive; thus, it is not yet possible to compare these simulation results with experiment. Our results are qualitatively similar to previous model and ab initio simulations. However, our simulations include correlation effects and a common *cis* bond defect which represents only one of the many types of defects present in the real material. Many fundamental questions remain concerning the importance of interchain interactions and their role in promoting soliton transport. Perhaps this type of ab initio investigation can be extended in the future to study these issues.

APPENDIX: LDA CALCULATION IN MOMENTUM SPACE FORMALISM

Electronic density and total energy are calculated using the Kohn-Sham (KS) scheme of the local DFT [37], in which the total energy of the system is defined as a function of electron orbitals $\psi_{i,\sigma}$ and coordinates of ions R_I by

$$E[\{\psi_{i,\sigma}\}, \{\mathbf{R}_I\}] = \sum_{\{i,\sigma\}}^{occ} \int d\mathbf{r} \psi_{i,\sigma}^*(\mathbf{r}) \left(-\frac{1}{2}\nabla^2\right) \psi_{i,\sigma}(\mathbf{r}) + \int d\mathbf{r} V_{ext}(\mathbf{r}) n(\mathbf{r}) \\ + \frac{1}{2} \int d\mathbf{r} d\mathbf{r}' \frac{n(\mathbf{r}) n(\mathbf{r}')}{|\mathbf{r} - \mathbf{r}'|} + E_{xc}[n_\uparrow, n_\downarrow] + \frac{1}{2} \sum_{I \neq J} \frac{Z_I Z_J}{|\mathbf{R}_I - \mathbf{R}_J|}, \quad (75)$$

where n_\uparrow and n_\downarrow are spin electron densities for spin up and spin down, respectively, and $n(\mathbf{r})$ is total electron density, defined as

$$n(\mathbf{r}) = \sum_{\{i,\sigma\}}^{occ} |\psi_{i,\sigma}(\mathbf{r})|^2. \quad (76)$$

$V_{ext}(\mathbf{r})$ is the total external potential felt by electrons; in pseudopotential formulation, $V_{ext}(\mathbf{r})$ is a sum of ionic pseudopotentials. E_{xc} is the exchange-correlation energy. The last term in Eq. (75) represents the Coulomb interaction of ionic cores, where Z_I is ionic core charge. The single-particle orbitals $\{\psi_{i,\sigma}\}$ are subject to the orthonormality constraints

$$\int d\mathbf{r} \psi_{i,\sigma}^*(\mathbf{r}) \psi_{j,\sigma}(\mathbf{r}) = \delta_{i,j}. \quad (77)$$

The derivative of $E[\{\psi_{i,\sigma}\}, \{\mathbf{R}_I\}]$ with respect to $\delta\psi_{i,\sigma}^*(\mathbf{r})$ with constraint $\sum_j \Lambda_{ij} \psi_{j,\sigma}$ leads to the Euler-Lagrange equations $H_\sigma \psi_{i,\sigma} = \sum_j \Lambda_{ij} \psi_{j,\sigma}$, where

$$\frac{\delta E}{\delta\psi_{i,\sigma}^*(\mathbf{r})} = \left(-\frac{1}{2}\nabla^2\right) \psi_{i,\sigma}(\mathbf{r}) + \frac{\delta \left[\int d\mathbf{r} V_{ext}(\mathbf{r}) n(\mathbf{r}) + \frac{1}{2} \int d\mathbf{r} d\mathbf{r}' \frac{n(\mathbf{r}) n(\mathbf{r}')}{|\mathbf{r} - \mathbf{r}'|} \right]}{\delta n(\mathbf{r})} \frac{\delta n(\mathbf{r})}{\delta\psi_{i,\sigma}^*(\mathbf{r})} \\ + \frac{\delta E_{xc}[n_\uparrow, n_\downarrow]}{\delta n_\sigma(\mathbf{r})} \frac{\delta n_\sigma(\mathbf{r})}{\delta\psi_{i,\sigma}^*(\mathbf{r})} \\ = \left(-\frac{1}{2}\nabla^2\right) \psi_{i,\sigma}(\mathbf{r}) + \left[V_{ext}(\mathbf{r}) + \int d\mathbf{r}' \frac{n(\mathbf{r}')}{|\mathbf{r} - \mathbf{r}'|} \right] \psi_{i,\sigma}(\mathbf{r}) + \mu_{xc}^\sigma(\mathbf{r}) \psi_{i,\sigma}(\mathbf{r}) \\ \equiv H_\sigma \psi_{i,\sigma}(\mathbf{r}). \quad (78)$$

The Hamiltonian operator H_σ , which is associated with Euler-Lagrange equation, is defined as

$$H_\sigma = -\frac{1}{2}\nabla^2 + V_{ext}(\mathbf{r}) + V_H(\mathbf{r}) + \mu_{xc}^\sigma(\mathbf{r}), \quad (79)$$

where $V_H(\mathbf{r}) = \int d\mathbf{r}' \frac{n(\mathbf{r}')}{|\mathbf{r}-\mathbf{r}'|}$ is the Hartree potential and $\mu_{xc}^\sigma(\mathbf{r}) = \frac{\delta E_{xc}[n]}{\delta n_\sigma(\mathbf{r})}$ with $\sigma = \uparrow$ or \downarrow is the exchange-correlation potential. Therefore, Eq. (75) can be rewritten as

$$\begin{aligned} E[\{\psi_{i,\sigma}\}, \{\mathbf{R}_I\}] &= \sum_{i,\sigma} \langle \psi_{i,\sigma} | H_\sigma | \psi_{i,\sigma} \rangle - \frac{1}{2} \int d\mathbf{r} \int d\mathbf{r}' \frac{n(\mathbf{r})n(\mathbf{r}')}{|\mathbf{r}-\mathbf{r}'|} \\ &\quad - \sum_\sigma P_{xc}^\sigma + E_{xc}[n_\uparrow, n_\downarrow] + E_{ion-ion}, \end{aligned} \quad (80)$$

where $P_{xc}^\sigma \equiv \int d\mathbf{r} \mu_{xc}^\sigma(\mathbf{r}) n_\sigma(\mathbf{r})$.

In the plane-wave formalism, the wave function is expanded in a sum of plane-waves, i.e.,

$$\psi_{i,\sigma}(\mathbf{r}) = \frac{1}{\sqrt{\Omega}} \sum_{\mathbf{G}} C_{\mathbf{G}}^{i,\sigma} e^{i\mathbf{G} \cdot \mathbf{r}}, \quad (81)$$

where \mathbf{G} is a reciprocal lattice vector, defined as $\mathbf{G}_i \equiv 2\pi \frac{\mathbf{a}_j \times \mathbf{a}_k}{\mathbf{a}_i \cdot \mathbf{a}_j \times \mathbf{a}_k}$ with \mathbf{a} as the basis vector in \mathbf{r} space and $i, j, k = x, y, z$. The orthonormal condition is $\sum_{\mathbf{G}} C_{\mathbf{G}}^{*i,\sigma} C_{\mathbf{G}}^{j,\sigma} = \delta_{ij}$. In practical application the sum over \mathbf{G} is truncated to include only M plane-waves, defined by the condition $\frac{1}{2}\mathbf{G}^2 < E_{cut}$. The energy cutoff E_{cut} determines the accuracy of the calculation. In order to complete the calculation of the electronic part, similar to Eq. (78), I solve the derivative of energy E with respect to $\delta C_{\mathbf{G}}^{*i,\sigma}$, which is

$$\frac{\delta E}{\delta C_{\mathbf{G}}^{*i,\sigma}} = \sum_{\mathbf{G}'} H_{\mathbf{G}\mathbf{G}'}^\sigma C_{\mathbf{G}'}^{i,\sigma} + \text{constraint}. \quad (82)$$

The total energy E is now

$$\begin{aligned}
E[\{\psi_{i,\sigma}\}, \{\mathbf{R}_I\}] &= \sum_{i,\sigma} \left(\sum_{\mathbf{G}'\mathbf{G}''} C_{\mathbf{G}'}^{*i,\sigma} H_{\mathbf{G}'\mathbf{G}''}^{\sigma} C_{\mathbf{G}''}^{i,\sigma} \right) - E_H - \sum_{\sigma} P_{xc}^{\sigma} \\
&\quad + E_{xc} + E_{ion-ion},
\end{aligned} \tag{83}$$

where the Hamiltonian matrix is given by

$$\begin{aligned}
H_{\mathbf{G}\mathbf{G}'}^{\sigma} &\equiv \frac{1}{\Omega} \int_{\Omega} d\mathbf{r} e^{-i\mathbf{G}\cdot\mathbf{r}} H_{\sigma} e^{i\mathbf{G}'\cdot\mathbf{r}} \\
&= T_{\mathbf{G}\mathbf{G}'}^{\sigma} \delta_{\mathbf{G},\mathbf{G}'} + V_{\mathbf{G}-\mathbf{G}'}^{ext} + V_{\mathbf{G}-\mathbf{G}'}^H + \mu_{\mathbf{G}-\mathbf{G}'}^{\sigma,xc}.
\end{aligned} \tag{84}$$

Since the kinetic energy operator is diagonal in momentum space and the potential energy operating on a wave vector is a convolution [see Eq. (84)], the number of operations required to solve the KS equation can be reduced dramatically by using fast Fourier transform (FFT) [75] and some minimization technique such as the steepest descent method. The fast-Fourier-transform algorithm can reduce the number of operations from $O(M^2)$ to $O(M \log_2 M)$, where M is total number of plane-waves for expansion of the wave functions. Solving the KS equation for a system in momentum space requires calculating Eqs. (82) and (83). The first term of Eq. (82) is essential to calculate $H_{\sigma} \psi_{i,\sigma}$ in momentum space, which is the object in the first part of this Appendix. The calculation of Hamiltonian and total energy are shown term by term in the following sections.

A.1 Calculation of Hamiltonian

The first most important task is how to evaluate Hamiltonian matrix $H_{\mathbf{G}\mathbf{G}'}^{\sigma}$. The following is the detailed calculation of Hamiltonian.

Kinetic Part

The first term of Eq. (84) is from kinetic energy; by definition,

$$\begin{aligned}
T_{\mathbf{G}\mathbf{G}'} &= -\frac{1}{\Omega} \int_{\Omega} d\mathbf{r} e^{-i\mathbf{G}\cdot\mathbf{r}} \frac{\nabla^2}{2} e^{i\mathbf{G}'\cdot\mathbf{r}} \\
&= \frac{(G')^2}{2} \frac{1}{\Omega} \int_{\Omega} d\mathbf{r} e^{i(\mathbf{G}'-\mathbf{G})\cdot\mathbf{r}} \\
&= \frac{G^2}{2} \delta_{\mathbf{G},\mathbf{G}'} \equiv T(\mathbf{G}) \delta_{\mathbf{G},\mathbf{G}'},
\end{aligned} \tag{85}$$

where $T(\mathbf{G}) = \frac{G^2}{2}$.

Local and Nonlocal Pseudopotentials

V_{ext} is the total external potential felt by electrons, which is sum of the ionic pseudopotential, i.e.,

$$V_{ext}(\mathbf{r}) = \sum_I v^{ps}(\mathbf{r} - \mathbf{R}_I); \tag{86}$$

the ionic pseudopotential is usually taken as [49, 76]

$$v^{ps}(\mathbf{r}) = \sum_l v_l(\mathbf{r}) \hat{\mathbf{P}}_l = v_{\bar{l}}(\mathbf{r}) + \Delta_{NL}(\mathbf{r}) = v_{\bar{l}}(\mathbf{r}) + \sum_{l=0}^{\bar{l}-1} \Delta v_l(\mathbf{r}) \hat{\mathbf{P}}_l, \tag{87}$$

where $\hat{\mathbf{P}}_l$ is the projector onto the l th angular momentum and $\Delta v_l(\mathbf{r}) = v_l(\mathbf{r}) - v_{\bar{l}}(\mathbf{r})$ with $\bar{l} = l_{max}$. This equation assumes $v_l(\mathbf{r}) = v_{\bar{l}}(\mathbf{r})$ when $l > \bar{l}$. The values of pseudopotentials $v_l(r)$ and correspondent pseudo wave functions $\varphi_l(r)$ with $r \leq r_{cut}$ are given numerically by Hamann's result [49]. The first term of Eq. (87) is purely local and defined as $v_{local}(r) = v_{\bar{l}}(r)$, where

$$v_{local}(r) = \begin{cases} v_{\bar{l}}(r), & r \leq r_{cut} \\ -\frac{Zv}{r}, & r > r_{cut}. \end{cases} \tag{88}$$

Therefore, the Fourier transform of $v_{local}(r)$ is

$$v_{\mathbf{G}}^{local} = \int d\mathbf{r} e^{-i\mathbf{G}\cdot\mathbf{r}} v_{local}(r) = \int_0^\infty \int_0^\pi \int_0^{2\pi} e^{-iGr \cos \theta} v_{local}(r) r^2 \sin \theta dr d\theta d\phi$$

$$\begin{aligned}
&= 2\pi \int_0^\infty \int_0^\pi e^{-iGr \cos \theta} v_{local}(r) r^2 dr d(\cos \theta) \\
&= \frac{4\pi}{G} \int_0^\infty r v_{local}(r) \sin(Gr) dr \\
&= \frac{4\pi}{G} \int_0^{r_{cut}} r v_l(r) \sin(Gr) dr - \frac{4\pi Z_v}{G} \int_{r_{cut}}^\infty \sin(Gr) dr \\
&= \frac{4\pi}{G} \int_0^{r_{cut}} r v_l(r) \sin(Gr) dr + \frac{4\pi Z_v}{G^2} \cos(Gr) \Big|_{r_{cut}}^\infty \\
&= \frac{4\pi}{G} \int_0^{r_{cut}} r v_l(r) \sin(Gr) dr - \frac{4\pi Z_v}{G^2} \cos(Gr_{cut}). \tag{89}
\end{aligned}$$

At $G = 0$,

$$\begin{aligned}
v_{G=0}^{local} &= 4\pi \int_0^\infty r^2 v_{local}(r) dr \\
&= 4\pi \int_0^{r_{cut}} r^2 v_l(r) dr - 4\pi Z_v \int_{r_{cut}}^\infty r dr \\
&= 4\pi \int_0^{r_{cut}} r^2 v_l(r) dr + 2\pi Z_v r_{cut}^2 - 2\pi Z_v r_\infty^2. \tag{90}
\end{aligned}$$

The last term of Eq. (90) will be canceled by the divergence term of Hartree potential for a neutral system (will be shown later). The second term in Eq. (87) is the nonlocal contribution. In order to reduce the calculation to M operations, it is made completely separable, as suggested by Bylander and Kleinman [41], i.e.,

$$\begin{aligned}
v_{nonlocal}(\mathbf{r}) &= \sum_{l=0}^{\bar{l}-1} \Delta v_l(r) \hat{P}_l = \sum_{lm} |Y_{lm}\rangle \Delta v_l(r) \langle Y_{lm}| \\
&\approx \sum_{lm} \frac{|\Delta v_l \Phi_{lm}\rangle \langle \Phi_{lm} \Delta v_l|}{\langle \Phi_{lm} | \Delta v_l | \Phi_{lm} \rangle}, \tag{91}
\end{aligned}$$

where $\Phi_{lm}(\mathbf{r}) = \varphi_l(r) Y_{lm}(\theta, \phi)$, with $\varphi_l(r)$ the pseudo wave function in correspondence of the pseudopotential $v_l(r)$ from Hamann's results. $v_{nonlocal}$ is also separable in momentum space, i.e.,

$$v_{GG'}^{non-local} \equiv \sum_{lm} \chi_G^{lm} \chi_{G'}^{*lm}.$$

$$\begin{aligned}
&= \sum_{lm} \left(\int d\mathbf{r} e^{-i\mathbf{G}\cdot\mathbf{r}} \chi_l(r) Y_{lm}(\theta, \phi) \right) \left(\int d\mathbf{r} e^{i\mathbf{G}'\cdot\mathbf{r}} \chi_l(r) Y_{lm}^*(\theta, \phi) \right) \\
&\equiv \sum_{lm} I_{\mathbf{G}}^{*lm} I_{\mathbf{G}'}^{lm},
\end{aligned} \tag{92}$$

where

$$\chi_l(r) = \frac{|\Delta v_l \varphi_l\rangle}{\langle \Phi_{lm} | \Delta v_l | \Phi_{lm} \rangle} = \frac{\Delta v_l(r) \varphi_l(r)}{\sqrt{\int_0^\infty \Delta v_l(r) \varphi_l^2(r) r^2 dr}} \tag{93}$$

and $I_{\mathbf{G}}^{lm} \equiv \int d\mathbf{r} e^{i\mathbf{G}\cdot\mathbf{r}} \chi_l(r) Y_{lm}^*(\theta, \phi)$. Expanding the plane-wave $[e^{i\mathbf{G}\cdot\mathbf{r}}]$ in spherical harmonic functions,

$$e^{i\mathbf{G}\cdot\mathbf{r}} = 4\pi \sum_{l=0}^{\infty} i^l j_l(Gr) \sum_{m=-l}^l Y_{lm}^*(\theta, \phi) Y_{lm}(\theta_G, \phi_G) \tag{94}$$

Inserting Eq. (94) into $I_{\mathbf{G}}^{lm}$ yields

$$\begin{aligned}
I_{\mathbf{G}}^{lm} &= \int d\mathbf{r} e^{i\mathbf{G}\cdot\mathbf{r}} \chi_l(r) Y_{lm}^*(\theta, \phi) \\
&= 4\pi \sum_{l'=0}^{\infty} i^{l'} \sum_{m'=-l'}^{l'} Y_{l'm'}(\theta_G, \phi_G) \int \chi_l(r) j_{l'}(Gr) r^2 dr \times \\
&\quad \int \int Y_{lm}^*(\theta, \phi) Y_{l'm'}(\theta, \phi) \sin \theta d\theta d\phi.
\end{aligned} \tag{95}$$

Because we have relations $Y_{lm}^*(\theta, \phi) = (-1)^m Y_{l-m}(\theta, \phi)$ and orthonormality condition $\int \int Y_{lm}^*(\theta, \phi) Y_{l'm'}(\theta, \phi) \sin \theta d\theta d\phi = \delta_{ll'} \delta_{mm'}$,

$$\begin{aligned}
I_{\mathbf{G}}^{lm} &= 4\pi \sum_{l'=0}^{\infty} i^{l'} \sum_{m'=-l'}^{l'} Y_{l'm'}(\theta_G, \phi_G) \int \chi_l(r) j_{l'}(Gr) r^2 dr \times (-1)^{m'} \delta_{l,l'} \delta_{m,-m'} \\
&= 4\pi i^l (-1)^{-m} Y_{l-m}(\theta_G, \phi_G) \int \chi_l(r) j_l(Gr) r^2 dr \\
&= 4\pi i^l Y_{lm}^*(\theta_G, \phi_G) \int \chi_l(r) j_l(Gr) r^2 dr.
\end{aligned} \tag{96}$$

Therefore, Eq. (92) can be written as

$$v_{\mathbf{G}\mathbf{G}'}^{non-local} = \sum_{lm} (4\pi)^2 Y_{lm}(\theta_G, \phi_G) Y_{lm}^*(\theta_{G'}, \phi_{G'}) \times \int \chi_l(r) j_l(Gr) r^2 dr \int \chi_l(r) j_l(G'r) r^2 dr. \quad (97)$$

Because of the addition theorem

$$P_l(\cos \theta_{GG'}) = \sum_{m=-l}^l \frac{4\pi}{2l+1} Y_{lm}^*(\theta_G, \phi_G) Y_{lm}(\theta_{G'}, \phi_{G'}), \quad (98)$$

where $P_l(\cos \theta_{GG'})$ is the Legendre polynomial of the angle between the wave vector \mathbf{G} and \mathbf{G}' , i.e., $\cos \theta_{GG'} = \cos \theta_G \cos \theta_{G'} + \sin \theta_G \sin \theta_{G'} \cos(\phi_G - \phi_{G'})$. Insert Eq. (98), and Eq. (97) can be written as

$$v_{\mathbf{G}\mathbf{G}'}^{nonlocal} = \sum_l 4\pi(2l+1) P_l(\cos \theta_{GG'}) \int \chi_l(r) j_l(Gr) r^2 dr \int \chi_l(r) j_l(G'r) r^2 dr. \quad (99)$$

The addition theorem can be also written in a different form, which is

$$\begin{aligned} P_l(\cos \theta_{GG'}) &= P_l(\cos \theta_G) P_l(\cos \theta_{G'}) \\ &+ 2 \sum_{m=1}^l \frac{(l-m)!}{(l+m)!} P_l^m(\cos \theta_G) P_l^m(\cos \theta_{G'}) \cos[m(\phi_G - \phi_{G'})]. \end{aligned} \quad (100)$$

Insert this equation into Eq. (99), then

$$\begin{aligned} v_{\mathbf{G}\mathbf{G}'}^{nonlocal} &= \sum_l 4\pi(2l+1) [P_l(\cos \theta_G) P_l(\cos \theta_{G'}) \xi_{\mathbf{G}}^l \xi_{\mathbf{G}'}^l \\ &+ 2 \sum_{m=1}^l \frac{(l-m)!}{(l+m)!} P_l^m(\cos \theta_G) P_l^m(\cos \theta_{G'}) \cos m\phi_G \cos m\phi_{G'} \xi_{\mathbf{G}}^l \xi_{\mathbf{G}'}^l \\ &+ 2 \sum_{m=1}^l \frac{(l-m)!}{(l+m)!} P_l^m(\cos \theta_G) P_l^m(\cos \theta_{G'}) \sin m\phi_G \sin m\phi_{G'} \xi_{\mathbf{G}}^l \xi_{\mathbf{G}'}^l], \end{aligned} \quad (101)$$

where $\xi_{\mathbf{G}}^l = \int \chi_l(r) j_l(Gr) r^2 dr$. The first few Legendre polynomials are

$$\begin{aligned}
P_0(x) &= 1 \\
P_1(x) &= x \\
P_2(x) &= \frac{1}{2}(3x^2 - 1) \\
&\dots
\end{aligned} \tag{102}$$

The first few associate Legendre functions are $[P_l^m(x) = (1 - x^2)^{\frac{m}{2}} \frac{d^m}{dx^m} P_l(x)]$

$$\begin{aligned}
l = 0 \quad P_0^0 &= 0 \\
l = 1 \quad P_1^1 &= \sin \theta \\
&\quad P_1^0 = \cos \theta \\
l = 2 \quad P_2^2 &= 3 \sin^2 \theta \\
&\quad P_2^1 = 3 \sin \theta \cos \theta \\
&\quad P_2^0 = \frac{1}{2}(3 \cos^2 \theta - 1) \\
&\dots \quad \dots
\end{aligned} \tag{103}$$

The first few spherical Bessel functions are

$$\begin{aligned}
j_0(x) &= \frac{\sin x}{x} \\
j_1(x) &= \frac{\sin x}{x^2} - \frac{\cos x}{x} \\
j_2(x) &= \left(\frac{3}{x^3} - \frac{1}{x}\right) \sin x - \frac{3 \cos x}{x^2} \\
&\dots
\end{aligned} \tag{104}$$

If only s , p , and d states ($l \leq 2$) are considered,

$$\begin{aligned}
v_{\mathbf{G}\mathbf{G}'}^{nonlocal} &= \sqrt{4\pi} \xi_{\mathbf{G}}^0 \cdot \sqrt{4\pi} \xi_{\mathbf{G}'}^0 \\
&+ \sqrt{12\pi} \cos \theta_G \xi_{\mathbf{G}}^1 \cdot \sqrt{12\pi} \cos \theta_{G'} \xi_{\mathbf{G}'}^1 \\
&+ \sqrt{12\pi} \sin \theta_G \cos \phi_G \xi_{\mathbf{G}}^1 \cdot \sqrt{12\pi} \sin \theta_{G'} \cos \phi_{G'} \xi_{\mathbf{G}'}^1 \\
&+ \sqrt{12\pi} \sin \theta_G \sin \phi_G \xi_{\mathbf{G}}^1 \cdot \sqrt{12\pi} \sin \theta_{G'} \sin \phi_{G'} \xi_{\mathbf{G}'}^1 \\
&+ \sqrt{20\pi} \frac{3 \cos^2 \theta_G - 1}{2} \xi_{\mathbf{G}}^2 \cdot \sqrt{20\pi} \frac{3 \cos^2 \theta_{G'} - 1}{2} \xi_{\mathbf{G}'}^2 \\
&+ \sqrt{20\pi} \sqrt{3} \sin \theta_G \cos \theta_G \cos \phi_G \xi_{\mathbf{G}}^2 \cdot \sqrt{20\pi} \sqrt{3} \sin \theta_{G'} \cos \theta_{G'} \cos \phi_{G'} \xi_{\mathbf{G}'}^2
\end{aligned}$$

$$\begin{aligned}
& + \sqrt{20\pi}\sqrt{3}\sin\theta_G\cos\theta_G\sin\phi_G\xi_G^2 \cdot \sqrt{20\pi}\sqrt{3}\sin\theta_{G'}\cos\theta_{G'}\sin\phi_{G'}\xi_{G'}^2 \\
& + \sqrt{20\pi}\frac{\sqrt{3}\sin^2\theta_G\cos 2\phi_G}{2}\xi_G^2 \cdot \sqrt{20\pi}\frac{\sqrt{3}\sin^2\theta_{G'}\cos 2\phi_{G'}}{2}\xi_{G'}^2 \\
& + \sqrt{20\pi}\frac{\sqrt{3}\sin^2\theta_G\sin 2\phi_G}{2}\xi_G^2 \cdot \sqrt{20\pi}\frac{\sqrt{3}\sin^2\theta_{G'}\sin 2\phi_{G'}}{2}\xi_{G'}^2 \\
& = \sum_{j=1}^9 \chi_G^j \chi_{G'}^j.
\end{aligned} \tag{105}$$

With $\sin\theta_G = \frac{\sqrt{G_x^2+G_y^2}}{G}$, $\cos\theta_G = \frac{G_z}{G}$, $\sin\phi_G = \frac{G_y}{\sqrt{G_x^2+G_y^2}}$, and $\cos\phi_G = \frac{G_x}{\sqrt{G_x^2+G_y^2}}$, we have

$$\begin{aligned}
\chi_G^1 &= \sqrt{4\pi}\xi_G^0 \\
\chi_G^2 &= \sqrt{12\pi}\frac{G_z}{G}\xi_G^1 \\
\chi_G^3 &= \sqrt{12\pi}\frac{G_x}{G}\xi_G^1 \\
\chi_G^4 &= \sqrt{12\pi}\frac{G_y}{G}\xi_G^1 \\
\chi_G^5 &= \sqrt{20\pi}\frac{3G_z^2-G^2}{2G^2}\xi_G^2 \\
\chi_G^6 &= \sqrt{20\pi}\sqrt{3}\frac{G_z G_x}{G^2}\xi_G^2 \\
\chi_G^7 &= \sqrt{20\pi}\sqrt{3}\frac{G_z G_y}{G^2}\xi_G^2 \\
\chi_G^8 &= \sqrt{20\pi}\frac{\sqrt{3}}{2}\frac{G_x^2-G_y^2}{G^2}\xi_G^2 \\
\chi_G^9 &= \sqrt{20\pi}\sqrt{3}\frac{G_x G_y}{G^2}\xi_G^2
\end{aligned} \tag{106}$$

and

$$\xi_G^0 = \begin{cases} \int_0^{r_{cut}} \frac{r}{G} \sin(Gr) \varphi_0(r) \Delta v_0(r) dr, & G \neq 0 \\ \int_0^{r_{cut}} r^2 \varphi_0(r) \Delta v_0(r) dr, & G = 0 \end{cases} \tag{107}$$

$$\xi_G^1 = \begin{cases} \int_0^{r_{cut}} \frac{r}{G} \left[\frac{\sin(Gr)}{Gr} - \cos(Gr) \right] \varphi_1(r) \Delta v_1(r) dr, & G \neq 0 \\ 0, & G = 0 \end{cases} \tag{108}$$

$$\xi_G^2 = \begin{cases} \int_0^{r_{cut}} \frac{r}{G} \left[\frac{3\sin(Gr)}{(Gr)^2} - \frac{3\cos(Gr)}{Gr} - \sin(Gr) \right] \varphi_2(r) \Delta v_2(r) dr, & G \neq 0 \\ 0, & G = 0 \end{cases} \tag{109}$$

where $\Delta v_l(r) = v_l(r) - v_l(r)$ with $r \leq r_{cut}$ and is 0 with $r > r_{cut}$. All the values of $v_{\mathbf{G}\mathbf{G}'}^{local}$ and $v_{\mathbf{G}\mathbf{G}'}^{nonlocal}$ are precomputed only once for each chosen number of plane-waves.

When summed over all the atoms in the system, the local and nonlocal pseudopotentials in momentum space are written as

$$\begin{aligned} V_{\mathbf{G}\mathbf{G}'}^{local} &= \frac{1}{\Omega} \sum_I \int_{\Omega} d\mathbf{r} e^{-i\mathbf{G}\cdot\mathbf{r}} v_{local}(\mathbf{r} - \mathbf{R}_I) e^{i\mathbf{G}'\cdot\mathbf{r}} \\ &= \frac{1}{\Omega} \sum_I e^{-i\mathbf{G}\cdot\mathbf{R}_I} \left(\int d\mathbf{r} e^{-i\mathbf{G}\cdot\mathbf{r}} v_{local}(\mathbf{r}) e^{i\mathbf{G}'\cdot\mathbf{r}} \right) e^{i\mathbf{G}'\cdot\mathbf{R}_I} \\ &= \frac{1}{\Omega} \sum_I e^{-i\mathbf{G}\cdot\mathbf{R}_I} v_{\mathbf{G}\mathbf{G}'}^{local} e^{i\mathbf{G}'\cdot\mathbf{R}_I} \end{aligned} \quad (110)$$

and

$$\begin{aligned} V_{\mathbf{G}\mathbf{G}'}^{nonlocal} &= \frac{1}{\Omega} \sum_I \int_{\Omega} \int_{\Omega} d\mathbf{r} d\mathbf{r}' e^{-i\mathbf{G}\cdot\mathbf{r}} \left(\sum_j \chi_j(\mathbf{r} - \mathbf{R}_I) \chi_j^*(\mathbf{r}' - \mathbf{R}_I) \right) e^{i\mathbf{G}'\cdot\mathbf{r}'} \\ &= \frac{1}{\Omega} \sum_I \sum_j [e^{-i\mathbf{G}\cdot\mathbf{R}_I} \left(\int d\mathbf{r} e^{-i\mathbf{G}\cdot\mathbf{r}} \chi_j(\mathbf{r}) \right) \left(\int d\mathbf{r}' e^{i\mathbf{G}'\cdot\mathbf{r}'} \chi_j^*(\mathbf{r}') \right) e^{i\mathbf{G}'\cdot\mathbf{R}_I}] \\ &= \frac{1}{\Omega} \sum_I \sum_j \left(\chi_{\mathbf{G}}^j e^{-i\mathbf{G}\cdot\mathbf{R}_I} \right) \left(\chi_{\mathbf{G}'}^{*j} e^{i\mathbf{G}'\cdot\mathbf{R}_I} \right). \end{aligned} \quad (111)$$

However, in practical calculation of $H\psi$, the local pseudopotential part is first to fast-Fourier-transformed to \mathbf{r} space for combining with other potentials in real space. The local pseudopotential is then transformed back to \mathbf{k} space, i.e.,

$$[V_{local}\psi_{i,\sigma}]_{\mathbf{G}} = FFT \left[FFT \left(\frac{1}{\Omega} \sum_I v_{\mathbf{G}}^{local} e^{-i\mathbf{G}\cdot\mathbf{R}_I} \right) \psi_{i,\sigma}(\mathbf{r}) \right]. \quad (112)$$

The nonlocal pseudopotential part, when acting on ψ in momentum space, is as follows:

$$[V_{non-local}\psi_{i,\sigma}]_{\mathbf{G}} = \sum_{\mathbf{G}'} V_{\mathbf{G}\mathbf{G}'}^{non-local} C_{\mathbf{G}'}^{i,\sigma}$$

$$= \frac{1}{\Omega} \sum_I \sum_j \sum_{\mathbf{G}'} \left(\chi_{\mathbf{G}}^j e^{-i\mathbf{G} \cdot \mathbf{R}_I} \right) \left(\chi_{\mathbf{G}'}^{*j} e^{i\mathbf{G}' \cdot \mathbf{R}_I} \right) C_{\mathbf{G}'}^{i,\sigma}. \quad (113)$$

Therefore, in order to calculate $V_{non-local}\psi_{i,\sigma}$ in momentum space, the separable form suggested by Bylander and Kleinman [41] only requires $N_I \bar{l}^2 M'$ operations, where N_I is total number of atoms and M' is the number of nonzero Fourier coefficient.

Hartree Potential

The third term of Hamiltonian [Eq. (84)] is the Hartree potential. The Fourier transform of the Hartree potential is

$$\begin{aligned} V_{\mathbf{G}}^H &= \frac{1}{\Omega} \int_{\Omega} d\mathbf{r} e^{-i\mathbf{G} \cdot \mathbf{r}} \left(\int d\mathbf{r}' \frac{n(\mathbf{r}')}{|\mathbf{r} - \mathbf{r}'|} \right) \\ &= \frac{1}{\Omega} \int_{\Omega} d\mathbf{r}' n(\mathbf{r}') \left(\int d\mathbf{r} \frac{e^{-i\mathbf{G} \cdot \mathbf{r}}}{|\mathbf{r} - \mathbf{r}'|} \right) \\ &= \frac{4\pi}{G^2} \left(\frac{1}{\Omega} \int_{\Omega} d\mathbf{r}' e^{-i\mathbf{G} \cdot \mathbf{r}'} n(\mathbf{r}') \right) \\ &= \frac{4\pi}{G^2} n_{\mathbf{G}}, \end{aligned} \quad (114)$$

where $n_{\mathbf{G}}$ is the Fourier transform of the electronic charge density and is defined by $n_{\mathbf{G}} = \frac{1}{\Omega} \int_{\Omega} d\mathbf{r} e^{-i\mathbf{G} \cdot \mathbf{r}} n(\mathbf{r})$, which can be integrated by FFT. At $\mathbf{G} = 0$, $V_{\mathbf{G}=0}^H = 2\pi N_e r_{\infty}^2$, which is divergent. For a neutral system, $Z_v N_I = N_e$; this divergence term will be canceled by the divergence term from the local pseudopotential [Eq. (90)]. Similar to the treatment of the local pseudopotential, when acting on ψ ,

$$[V_H \psi_{i,\sigma}]_{\mathbf{G}} = FFT \left[FFT \left(V_{\mathbf{G}}^H \right) \psi_{i,\sigma}(\mathbf{r}) \right]. \quad (115)$$

Exchange-correlation Potential

The last term of Hamiltonian [Eq. (84)] is the exchange-correlation potential. A parametrized form of the exchange-correlation energy ($\epsilon_{xc} = \epsilon_x + \epsilon_c$) obtained by

Vosko et al. [38] is used. In this form exchange energy in real space can be written in the form

$$\epsilon_x(r_s, \zeta) = \epsilon_x^P(r_s) + [\epsilon_x^F(r_s) - \epsilon_x^P(r_s)] f(\zeta), \quad (116)$$

where $r_s = (\frac{3\Omega}{4\pi n})^{\frac{1}{3}}$ and $\zeta = (n_{\uparrow} - n_{\downarrow})/n$ are the standard variables for density and spin polarization. P/F stands for para/ferro-magnetic states, with

$$\epsilon_x^P(r_s) = -\frac{3}{2\pi\alpha r_s} = \frac{\epsilon_x^F(r_s)}{2^{\frac{1}{3}}}, \quad \alpha = \left(\frac{4}{9\pi}\right)^{\frac{1}{3}} \quad (117)$$

and

$$f(\zeta) = \frac{[(1 + \zeta)^{\frac{4}{3}} + (1 - \zeta)^{\frac{4}{3}} - 2]}{2(2^{\frac{1}{3}} - 1)}. \quad (118)$$

ϵ_x can be evaluated directly if the electronic density n_{\uparrow} and n_{\downarrow} are known.

Similarly, the correlation energy is written as

$$\epsilon_c(r_s, \zeta) = \epsilon_c^P(r_s) + [\epsilon_c^F(r_s) - \epsilon_c^P(r_s)] f(\zeta), \quad (119)$$

with

$$\begin{aligned} \epsilon_c^{P/F}(r_s) = & A \left\{ \ln \frac{x^2}{X(x)} + \frac{2b}{Q} \tan^{-1} \frac{Q}{2x+b} \right. \\ & \left. - \frac{bx_o}{X(x_o)} \left[\ln \frac{(x-x_o)^2}{X(x)} + \frac{2(b+2x_o)}{Q} \tan^{-1} \frac{Q}{2x+b} \right] \right\}, \end{aligned} \quad (120)$$

where $x = \sqrt{r_s}$, $X(x) = x^2 + bx + c$ and $Q = \sqrt{4c - b^2}$. The required parameters are given in the following table:

	paramagnetic	ferromagnetic
A	3.10907×10^{-2}	1.55453×10^{-2}
x_o	-1.04980×10^{-1}	-3.25000×10^{-1}
b	3.72744	7.06042
c	$1.29352 \times 10^{+1}$	$1.80578 \times 10^{+1}$

Therefore, the correspondent exchange-correlation potential is written as

$$\begin{aligned}
 \mu_{xc}^\sigma(r_s, \zeta) &= \frac{\delta}{\delta n_\sigma} \left[\int d\mathbf{r} (n_\uparrow + n_\downarrow) \epsilon_{xc}(r_s, \zeta) \right] \\
 &= \epsilon_{xc}(r_s, \zeta) + (n_\uparrow + n_\downarrow) \left[\frac{dr_s}{dn_\sigma} \frac{d\epsilon_{xc}(r_s, \zeta)}{dr_s} + \frac{d\zeta}{dn_\sigma} \frac{d\epsilon_{xc}(r_s, \zeta)}{d\zeta} \right] \\
 &= \epsilon_{xc}(r_s, \zeta) - \frac{r_s}{3} \frac{d\epsilon_{xc}(r_s, \zeta)}{dr_s} + n \frac{d\zeta}{dn_\sigma} \frac{d\epsilon_{xc}(r_s, \zeta)}{d\zeta}
 \end{aligned} \tag{121}$$

because

$$\mu_{xc}^{P/F}(r_s) = \epsilon_{xc}^{P/F}(r_s) - \frac{r_s}{3} \frac{d\epsilon_{xc}^{P/F}(r_s)}{dr_s} = \frac{4}{3} \epsilon_{xc}^{P/F}(r_s). \tag{122}$$

Insert this equation and Eq. (116) into Eq. (121):

$$\mu_{xc}^\sigma(r_s, \zeta) = \mu_{xc}^P(r_s) + f(\zeta) [\mu_{xc}^F(r_s) - \mu_{xc}^P(r_s)] - [sgn(\sigma) - \zeta] \frac{df(\zeta)}{d\zeta} [\epsilon_{xc}^F(r_s) - \epsilon_{xc}^P(r_s)], \tag{123}$$

where

$$sgn(\sigma) = \begin{cases} 1 & (\sigma = \uparrow) \\ -1 & (\sigma = \downarrow) \end{cases} \tag{124}$$

and

$$\frac{df(\zeta)}{d\zeta} = \frac{4}{3} \frac{(1+\zeta)^{\frac{1}{3}} - (1-\zeta)^{\frac{1}{3}}}{2^{\frac{4}{3}} - 2}. \tag{125}$$

Therefore, the value of $\mu_{xc}^\sigma \psi_{i,\sigma}$ in \mathbf{k} space is obtained directly by FFT, i.e.,

$$(\mu_{xc}^\sigma \psi_{i,\sigma})_{\mathbf{G}} = FFT [\mu_{xc}^\sigma(n) \psi_{i,\sigma}(\mathbf{r})] \tag{126}$$

Operation Counts to Evaluate $H\psi$

The kinetic term is diagonal in reciprocal space so that its action on the wave functions requires only $O(N_e M)$ operations, where N_e is total number of electrons and

M is the number of plane-waves for calculation. The local pseudopotential, Hartree potential, and exchange-correlation potential require $O(N_e \frac{M}{2} \log_2 M)$ operations to transform from real space to momentum space. To calculate nonlocal pseudopotential requires $O(LN_I N_e M')$, with $L = \bar{l}^2$ and M' is the number of nonzero Fourier coefficient if cutting Fourier space as a sphere. Another $O(N_e \frac{M}{2} \log_2 M)$ is required in order to calculate the electronic density and $O(N_e^2 M')$ to perform the Gram-Schmidt procedure for orthonormalization. Therefore, considering only the most time-consuming terms, the total operations are $O(N_e M \log_2 M + (LN_I N_e + N_e^2) M')$.

A.2 Calculation of Total Energy

Orbital Energy

The first term of Eq. (83) is trivial in momentum space.

Hartree Energy

The second term of Eq. (83) is Hartree Energy. $n(\mathbf{r}) = \sum_{\mathbf{G}} n_{\mathbf{G}} e^{i\mathbf{G} \cdot \mathbf{r}}$,

$$\begin{aligned}
 E_H &= \frac{1}{2} \int_{\Omega} \int_{\Omega} d\mathbf{r} d\mathbf{r}' \frac{n(\mathbf{r})n(\mathbf{r}')}{|\mathbf{r} - \mathbf{r}'|} \\
 &= \frac{1}{2} \int_{\Omega} \int_{\Omega} d\mathbf{r} d\mathbf{r}' \sum_{\mathbf{G}} \sum_{\mathbf{G}'} n_{\mathbf{G}} n_{\mathbf{G}'}^* \frac{e^{i(\mathbf{G} \cdot \mathbf{r} - \mathbf{G}' \cdot \mathbf{r}')}}{|\mathbf{r} - \mathbf{r}'|} \\
 &= \frac{1}{2} \int_{\Omega} \int_{\Omega} d\mathbf{r} d\mathbf{r}' \sum_{\mathbf{G}} \sum_{\mathbf{G}'} n_{\mathbf{G}} n_{\mathbf{G}'}^* \frac{e^{i\mathbf{G} \cdot (\mathbf{r} - \mathbf{r}')}}{|\mathbf{r} - \mathbf{r}'|} e^{i(\mathbf{G} - \mathbf{G}') \cdot \mathbf{r}'} \\
 &= \frac{\Omega}{2} \sum_{\mathbf{G}} \sum_{\mathbf{G}'} |n(\mathbf{G})|^2 \frac{4\pi}{G^2} \delta_{\mathbf{G}, \mathbf{G}'} \\
 &= \frac{\Omega}{2} \sum_{\mathbf{G}} |n(\mathbf{G})|^2 \frac{4\pi}{G^2} \\
 &= \frac{\Omega}{2} \sum_{\mathbf{G} \neq 0} |n(\mathbf{G})|^2 \frac{4\pi}{G^2} + \lim_{G \rightarrow 0} \frac{N_e^2}{2\Omega} \frac{4\pi}{G^2}.
 \end{aligned} \tag{127}$$

The second term of Eq. (127) is divergent. However, it is canceled by the divergence term from ion-ion interaction, which will be shown in the following.

Exchange-correlation Energy

The third and fourth terms of Eq. (83) come from the exchange-correlation potential/energy, which defined in section A.1. By definition, they can be written as

$$E_{xc} = \int d\mathbf{r} \epsilon_{xc}(n)n(\mathbf{r}), \quad P_{xc}^\sigma = \int d\mathbf{r} \mu_{xc}^\sigma(\mathbf{r})n(\mathbf{r}). \quad (128)$$

Ion-Ion Interaction

The last term of Eq. (83) is from ion-ion interaction. Since the cluster is confined in a periodic unit cell, by definition,

$$\begin{aligned} E_{ion-ion} &= \frac{1}{2} \sum_{IJ} \frac{Z_I Z_J}{|\mathbf{R}_I - \mathbf{R}_J|} = \frac{Z_v^2}{2} \left(\sum_{IJ} \sum_{\mathbf{a}} \right)' \frac{1}{|\mathbf{R}_I - \mathbf{R}_J - \mathbf{a}|} \\ &= \frac{Z_v^2}{2} \sum_{I \neq J} \sum_{\mathbf{a}} \frac{1}{|\mathbf{R}_I - \mathbf{R}_J - \mathbf{a}|} + \frac{Z_v^2 N_I}{2} \sum_{\mathbf{a} \neq 0} \frac{1}{|\mathbf{a}|}, \end{aligned} \quad (129)$$

where Z_v is total number of valence electrons on atom and \mathbf{a} is the lattice vector.

From Ewald summation,

$$\sum_{\mathbf{a}} \frac{1}{|\mathbf{R} - \mathbf{a}|} = \frac{1}{\Omega} \sum_{\mathbf{G}} \frac{4\pi}{G^2} e^{i\mathbf{G} \cdot \mathbf{R}} e^{-\frac{G^2}{4G_{cut}^2}} + \sum_{\mathbf{a}} \frac{1}{|\mathbf{R} - \mathbf{a}|} \text{erfc}\{G_{cut}|\mathbf{R} - \mathbf{a}|\}. \quad (130)$$

Substituting Eq. (130) into Eq. (129),

$$\begin{aligned} E_{ion-ion} &= \frac{Z_v^2}{2} \sum_{I \neq J} \left[\frac{1}{\Omega} \sum_{\mathbf{G}} \frac{4\pi}{G^2} e^{i\mathbf{G} \cdot (\mathbf{R}_I - \mathbf{R}_J)} e^{-\frac{G^2}{4G_{cut}^2}} \right. \\ &\quad \left. + \sum_{\mathbf{a}} \frac{1}{|\mathbf{R}_I - \mathbf{R}_J - \mathbf{a}|} \text{erfc}\{G_{cut}|\mathbf{R}_I - \mathbf{R}_J - \mathbf{a}|\} \right] + \frac{Z_v^2 N_I}{2} \sum_{\mathbf{a} \neq 0} \frac{1}{|\mathbf{a}|} \end{aligned}$$

$$\begin{aligned}
&= \frac{Z_v^2}{2\Omega} \sum_{\mathbf{G} \neq 0} \frac{4\pi}{G^2} e^{-\frac{G^2}{4G_{cut}^2}} \left[\sum_{IJ} e^{i\mathbf{G} \cdot (\mathbf{R}_I - \mathbf{R}_J)} - N_I \right] \\
&\quad + \frac{Z_v^2}{2\Omega} \lim_{G \rightarrow 0} \frac{4\pi}{G^2} N_I (N_I - 1) \left[1 - \frac{G^2}{4G_{cut}^2} \right] \\
&\quad + \frac{Z_v^2}{2} \sum_{I \neq J} \sum_{\mathbf{a}} \frac{1}{|\mathbf{R}_I - \mathbf{R}_J - \mathbf{a}|} \text{erfc}\{G_{cut}|\mathbf{R}_I - \mathbf{R}_J - \mathbf{a}|\} \\
&\quad + \frac{Z_v^2 N_I}{2} \left[\sum_{\mathbf{a} \neq 0} \frac{1}{|\mathbf{a}|} - \lim_{G \rightarrow 0} \frac{1}{\Omega} \frac{4\pi}{G^2} \right] + \frac{Z_v^2 N_I}{2\Omega} \lim_{G \rightarrow 0} \frac{4\pi}{G^2} \\
&= \frac{Z_v^2}{2\Omega} \sum_{\mathbf{G} \neq 0} \frac{4\pi}{G^2} e^{-\frac{G^2}{4G_{cut}^2}} [|S_{\mathbf{G}}|^2 - N_I] \\
&\quad + \frac{Z_v^2}{2} \sum_{I \neq J} \sum_{\mathbf{a}} \frac{1}{|\mathbf{R}_I - \mathbf{R}_J - \mathbf{a}|} \text{erfc}\{G_{cut}|\mathbf{R}_I - \mathbf{R}_J - \mathbf{a}|\} \\
&\quad - \frac{Z_v^2 N_I}{2} \frac{\alpha}{r'_s} - \frac{Z_v^2 \pi}{2\Omega G_{cut}^2} N_I (N_I - 1) + \frac{Z_v^2 N_I^2}{2\Omega} \lim_{G \rightarrow 0} \frac{4\pi}{G^2}, \tag{131}
\end{aligned}$$

where $S_{\mathbf{G}} \equiv \sum_I e^{-i\mathbf{G} \cdot \mathbf{R}_I}$, which is the structure factor; $r'_s = \left(\frac{3\Omega}{4\pi}\right)^{\frac{1}{3}}$; and the constant α is

$$\alpha = \begin{cases} 1.7601188 & (sc) \\ 1.791753 & (fcc) \\ 1.791860 & (fcc). \end{cases} \tag{132}$$

The error function $\text{erfc}(x)$ is defined by

$$\begin{aligned}
\text{erfc}(x) &= 1 - \text{erf}(x) = \frac{2}{\pi} \int_x^\infty e^{-t^2} dt = \frac{1}{\pi} \int_{x^2}^\infty e^{-\tau} \tau^{-\frac{1}{2}} d\tau \\
&= \frac{e^{-x^2}}{\sqrt{\pi}x} \left(1 - \frac{1}{2x^2} + \frac{1 \cdot 3}{2^2 x^4} - \frac{1 \cdot 3 \cdot 5}{2^3 x^6} + \dots \right). \tag{133}
\end{aligned}$$

For a neutral system ($Z_v N_I = N_e$), the last term of Eq. (131) will be canceled with the second term of Hartree energy [Eq. (127)] when subtracting two energies. In my case, I chose 1 unit size for G_{cut} , i.e., $G_{cut} = \frac{2\pi}{a}$.

A.3 Hellmann-Feynman Force

I apply the Hellmann-Feynman theory [77, 78] to calculate the forces on ionic cores, i.e.,

$$\begin{aligned}
 \mathbf{F}_I &= -\nabla_{\mathbf{R}_I} E[\{\psi_{i,\sigma}\}, \{\mathbf{R}_I\}] = -\left[\nabla_{\mathbf{R}_I} E_{ext} + \nabla_{\mathbf{R}_I} E_{ion-ion}\right] \\
 &= \sum_{i,\sigma} \left\langle \psi_{i,\sigma} \left| -\frac{\partial V_I^{ps}}{\partial \mathbf{R}_I} \right| \psi_{i,\sigma} \right\rangle + \sum_{I \neq J} Z_I Z_J \frac{\mathbf{R}_I - \mathbf{R}_J}{|\mathbf{R}_I - \mathbf{R}_J|^3}.
 \end{aligned} \tag{134}$$

Local Pseudopotential Part

By definition,

$$\begin{aligned}
 \mathbf{F}_I^{local} &= -\int d\mathbf{r} \, n(\mathbf{r}) \nabla_{\mathbf{R}_I} v_I(\mathbf{r} - \mathbf{R}_I) \\
 &= -\sum_{\mathbf{G}} n_{\mathbf{G}} \int d\mathbf{r} \, e^{i\mathbf{G} \cdot \mathbf{r}} \nabla_{\mathbf{R}_I} v_I(\mathbf{r} - \mathbf{R}_I) \\
 &= -\sum_{\mathbf{G}} n_{\mathbf{G}} \int d\mathbf{r} \, e^{i\mathbf{G} \cdot \mathbf{r}} \nabla_{\mathbf{R}_I} \left(v_I(\mathbf{r}) e^{i\mathbf{G} \cdot \mathbf{R}_I} \right) \\
 &= -\sum_{\mathbf{G}} n_{\mathbf{G}} \left(\int d\mathbf{r} \, e^{i\mathbf{G} \cdot \mathbf{r}} v_I(\mathbf{r}) \right) (i\mathbf{G}) e^{i\mathbf{G} \cdot \mathbf{R}_I} \\
 &= -\sum_{\mathbf{G}} n_{\mathbf{G}} v_{\mathbf{G}}^{local*} (i\mathbf{G}) e^{i\mathbf{G} \cdot \mathbf{R}_I},
 \end{aligned} \tag{135}$$

where $n(\mathbf{r}) = \sum_{\mathbf{G}} n_{\mathbf{G}} e^{i\mathbf{G} \cdot \mathbf{r}}$ and $v_{\mathbf{G}}^{local} = \int d\mathbf{r} \, e^{-i\mathbf{G} \cdot \mathbf{r}} v_{local}(\mathbf{r})$.

Nonlocal Pseudopotential Part

By definition,

$$\begin{aligned}
 F_I^{nonlocal} &= -\sum_j \sum_{i,\sigma} \int \int d\mathbf{r} d\mathbf{r}' \, \psi_{i,\sigma}^*(\mathbf{r}) \left[\nabla_{\mathbf{R}_I} \chi_j(\mathbf{r} - \mathbf{R}_I) \chi_j^*(\mathbf{r}' - \mathbf{R}_I) \right] \psi_{i,\sigma}(\mathbf{r}') \\
 &= -\sum_j \sum_{i,\sigma} \left[\int d\mathbf{r} \, \psi_{i,\sigma}^*(\mathbf{r}) \nabla_{\mathbf{R}_I} \chi_j(\mathbf{r} - \mathbf{R}_I) \right] \left[\int d\mathbf{r}' \, \psi_{i,\sigma}(\mathbf{r}') \chi_j^*(\mathbf{r}' - \mathbf{R}_I) \right]
 \end{aligned}$$

$$\begin{aligned}
& - \sum_j \sum_{i,\sigma} \left[\int d\mathbf{r} \psi_{i,\sigma}^*(\mathbf{r}) \chi_j(\mathbf{r} - \mathbf{R}_I) \right] \left[\int d\mathbf{r}' \psi_{i,\sigma}(\mathbf{r}') \nabla_{\mathbf{R}_I} \chi_j^*(\mathbf{r}' - \mathbf{R}_I) \right] \\
& = - \sum_j \sum_{i,\sigma} 2\text{Re} \left\{ \left[\int d\mathbf{r} \psi_{i,\sigma}^*(\mathbf{r}) \nabla_{\mathbf{R}_I} \chi_j(\mathbf{r} - \mathbf{R}_I) \right] \right. \\
& \quad \left. \left[\int d\mathbf{r}' \psi_{i,\sigma}(\mathbf{r}') \chi_j^*(\mathbf{r}' - \mathbf{R}_I) \right] \right\} \\
& = - \sum_j \sum_{i,\sigma} \sum_{\mathbf{G}\mathbf{G}'} \frac{2}{\Omega} \text{Re} \{ C_{\mathbf{G}}^{*i,\sigma} C_{\mathbf{G}'}^{i,\sigma} \nabla_{\mathbf{R}_I} (e^{-i\mathbf{G}\cdot\mathbf{R}_I}) e^{i\mathbf{G}'\cdot\mathbf{R}_I} \\
& \quad \left[\int d\mathbf{r} e^{-i\mathbf{G}\cdot\mathbf{r}} \chi_j(\mathbf{r}) \right] \left[\int d\mathbf{r}' e^{i\mathbf{G}'\cdot\mathbf{r}'} \chi_j^*(\mathbf{r}') \right] \} \\
& = \frac{2}{\Omega} \text{Re} \left\{ \sum_{i,\sigma} \sum_j \left[\sum_{\mathbf{G}} C_{\mathbf{G}}^{*i,\sigma} (-i\mathbf{G}) e^{-i\mathbf{G}\cdot\mathbf{R}_I} \chi_{\mathbf{G}}^j \right] \right. \\
& \quad \left. \left[\sum_{\mathbf{G}'} C_{\mathbf{G}'}^{i,\sigma} e^{i\mathbf{G}'\cdot\mathbf{R}_I} \chi_{\mathbf{G}}^{*j} \right] \right\}, \tag{136}
\end{aligned}$$

where $\psi_{i,\sigma}(\mathbf{r}) = \sum_{\mathbf{G}} C_{\mathbf{G}}^{i,\sigma} e^{i\mathbf{G}\cdot\mathbf{r}}$ and $\chi_{\mathbf{G}}^j = \int d\mathbf{r} e^{-i\mathbf{G}\cdot\mathbf{r}} \chi_j(\mathbf{r})$.

Ion-ion Interaction Part

From Eq. (131),

$$\begin{aligned}
F_I^{ion-ion} & = \frac{Z_v^2}{\Omega} \sum_J \sum_{\mathbf{G} \neq 0} \text{Im} \left\{ \mathbf{G} \frac{4\pi}{G^2} e^{-\frac{G^2}{4G_{cut}^2}} e^{i\mathbf{G}\cdot(\mathbf{R}_I - \mathbf{R}_J)} \right\} \\
& + Z_v^2 \sum_J \sum_{\mathbf{a}} \frac{\mathbf{R}_I - \mathbf{R}_J - \mathbf{a}}{|\mathbf{R}_I - \mathbf{R}_J - \mathbf{a}|^3} \text{erfc}\{G_{cut}|\mathbf{R}_I - \mathbf{R}_J - \mathbf{a}|\} \\
& + Z_v^2 \sum_J \sum_{\mathbf{a}} \frac{\mathbf{R}_I - \mathbf{R}_J - \mathbf{a}}{|\mathbf{R}_I - \mathbf{R}_J - \mathbf{a}|^2} \frac{2}{G_{cut}\sqrt{\pi}} e^{-G_{cut}^2|\mathbf{R}_I - \mathbf{R}_J - \mathbf{a}|^2}. \tag{137}
\end{aligned}$$

REFERENCES

- [1] A. J. Heeger, in *Handbook of Conducting Polymers*, edited by T. A. Skotheim (Marcel Dekker, Berlin, 1986), Vol. 2, Chap. 21, pp. 729–757.
- [2] J. Tsukamoto, in *Advances in Physics*, edited by D. Sherrington (Taylor & Francis Ltd, London, 1992).
- [3] A. J. Heeger, in *Handbook of Conducting Polymers*, edited by T. A. Skotheim (Marcel Dekker, New York, 1986), Vol. 2, Chap. 21.
- [4] J. C. Scott, *Science* **278**, 2071 (1997).
- [5] D. Clery, *Science* **263**, 1700 (1994).
- [6] B. Weinberger *et al.*, *J. Chem. Phys.* **72**, 4749 (1980).
- [7] P. Bernier, in *Handbook of Conducting Polymers*, edited by T. A. Skotheim (Marcel Dekker, New York, 1986), Vol. 2, Chap. 30.
- [8] H. Gibson *et al.*, *Phys. Rev. B* **31**, 2338 (1985).
- [9] P. Carter and J. Porter, *Phys. Rev. B* **43**, 14478 (1991).
- [10] W. P. Su, J. Schrieffer, and A. Heeger, *Phys. Rev. Lett.* **42**, 1698 (1979).
- [11] W. Su, J. Schrieffer, and A. Heeger, *Phys. Rev. B* **22**, 2099 (1980).
- [12] R. Peierls, *Quantum Theory of Solids* (Clarendon, London, 1955).
- [13] C. R. Fincher, C. E. Chen, A. J. Heeger, and A. G. MacDiarmid, *Phys. Rev. Lett.* **48**, 100 (1982).
- [14] C. Yannoni and T. C. Clarke, *Phys. Rev. Lett.* **51**, 1191 (1983).
- [15] D. Moses *et al.*, *Phys. Rev. B* **26**, 3361 (1982).
- [16] L. Yu, *Solitons and Polarons in Conducting Polymers* (World Scientific Publishing, Singapore, 1988).
- [17] C. H. Choi and M. Kertesz, *J. Chem. Phys.* **107**, 6712 (1997).
- [18] H. O. Villar, M. Dupuis, and E. Clementi, *Phys. Rev. B* **37**, 2520 (1988).
- [19] S. Suhai, *Phys. Rev. B* **51**, 16533 (1995).

- [20] H. Guo and J. Paldus, *Int. J. Quant. Chem.* **63**, 345 (1997).
- [21] P. Vogl and D. K. Campbell, *Phys. Rev. B* **41**, 12797 (1990).
- [22] L. Ye, A. Freeman, D. Ellis, and B. Delley, *Phys. Rev. B* **40**, 6277 (1989).
- [23] M. Springborg, J. Calais, O. Goscinski, and L. Eriksson, *Phys. Rev. B* **44**, 2713 (1991).
- [24] C. Möller and M. S. Plesset, *Phys. Rev.* **46**, 618 (1934).
- [25] A. D. Becke, *J. Chem. Phys.* **98**, 5648 (1993).
- [26] A. D. Becke, *Phys. Rev. A* **38**, 3098 (1988).
- [27] J. P. Perdew, *Phys. Rev. B* **33**, 8822 (1986).
- [28] C. Lee, W. Yang, and R. G. Parr, *Phys. Rev. B* **37**, 785 (1988).
- [29] J. Ashkenazi *et al.*, *Phys. Rev. Lett.* **62**, 2016 (1989).
- [30] R. Kawai, E. Bylaska, and J. H. Weare, (unpublished) .
- [31] P. K. Kahol, G. C. Clark, and M. Mehring, in *Conjugated Conducting Polymers*, edited by H. G. Kiess (Springer Verlag, Berlin, 1992), Chap. 5, p. 217.
- [32] M. Nechtschein *et al.*, *Phys. Rev. B* **23**, 61 (1983).
- [33] B. Ankele, G. Leising, and H. Kahlert, *Solid State Comm.* **62**, 6245 (1987).
- [34] J. D. Joannopoulos, in *Physics of Disordered Materials*, edited by D. Adler and H. Fritzsche (Plenum, New York, 1985), p. 19.
- [35] W. Pickett, *Comput. Phys. Rep.* **9**, 115 (1989).
- [36] R. Hohenberg and W. Kohn, *Phys. Rev.* **136**, B864 (1964).
- [37] W. Kohn and L. Sham, *Phys. Rev. A* **140**, 1133 (1965).
- [38] S. H. Vosko, L. Wilk, and M. Nusair, *Can. J. Phys.* **58**, 1200 (1980).
- [39] R. G. Parr and W. Yang, *Density Functional Theory of Atoms and Molecules* (Oxford University Press, New York, 1989).
- [40] D. R. Hamann, *Phys. Rev. B* **40**, 2980 (1980).
- [41] D. M. Bylander and L. Kleinman, *Phys. Rev. Lett.* **48**, 1425 (1982).
- [42] B. Johnson, P. Gill, and J. Pople, *J. Chem. Phys.* **98**, 5612 (1993).
- [43] W. Kohn and P. Vashishta, in *Theory of the Inhomogeneous Electron Gas*, edited by S. Lundqvist and N. March (Plenum Press, New York, 1981), Chap. 2, p. 79.

- [44] D. Langreth and M. Mehl, Phys. Rev. B **28**, 1809 (1983).
- [45] G. Ortiz and P. Ballone, Phys. Rev. B. **43**, 6376 (1991).
- [46] J. P. Perdew, K. Burke, and M. Ernzerhof, Phys. Rev. Lett. **77**, 3865 (1996).
- [47] R. Car and M. Parrinello, Phys. Rev. Lett. **95**, 1151 (1991).
- [48] L. Verlet, Phys. Rev. **159**, 98 (1967).
- [49] D. Hamann, Phys. Rev. B **40**, 2980 (1989).
- [50] E. J. Bylaska, Ph.D. thesis, University of California San Diego, 1998.
- [51] H. O. Villar *et al.*, J. Chem. Phys. **88**, 1003 (1988).
- [52] G. Fogarasi, R. Liu, and P. Pulay, J. Phys. Chem. **97**, 4036 (1993).
- [53] S. Hirata, H. Torii, and M. Tasumi, J. Chem. Phys. **103**, 8964 (1995).
- [54] C. Lee, W. Yang, and R. G. Parr, Phys. Rev. B **37**, 785 (1988).
- [55] K. Mizoguchi, Jpn. J. Appl. Phys. **34**, 1 (1995).
- [56] K. Holczer, J. P. Boucher, F. Devreux, and M. Nechtschein, Phys. Rev. B. **23**, 1051 (1981).
- [57] C. Q. Wu, J. Miao, J. Z. Yu, and Y. Kawazoe, Phys. Rev. B. **57**, 6 (1998).
- [58] S. Hirata, H. Torii, and M. Tasumi, Phys. Rev. B. **57**, 11994 (1998).
- [59] H. Teramae, J. Chem. Phys. **85**, 990 (1986).
- [60] H. Kass *et al.*, Europhys. Lett. **4**, 947 (1987).
- [61] B. Champagne, E. Deumens, and Y. Ohrn, J. Chem. Phys. **14**, 5433 (1997).
- [62] W. K. Wu and S. Kivelson, Phys. Rev. B **33**, 8546 (1986).
- [63] H. Thomann, L. R. Dalton, and M. Grabowski, Phys. Rev. B **31**, 3141 (1985).
- [64] L. Ye, A. Freeman, D. Ellis, and B. Delley, Phys. Rev. B. **40**, 6285 (1989).
- [65] R. R. Chance, D. S. Boudreaux, J. L. Bredas, and R. Silbey, in *Handbook of Conducting Polymers*, edited by T. A. Skotheim (Marcel Dekker, New York, 1986), Vol. 2, Chap. 24.
- [66] M. J. S. Dewar and W. Thiel, J. Am. Chem. Soc. **99**, 4899 (1977).
- [67] S. Larsson and L. Rodriguez-Monge, Int. J. of Quantum Chem. **58**, 517 (1996).
- [68] W. P. Su and J. R. Schrieffer, Proc. Natl. Acad. Sci. **77**, 5626 (1980).

- [69] W. Förner, C. L. Wang, F. Martino, and J. Ladik, *Phys. Rev. B.* **37**, 4567 (1988).
- [70] W. P. Su, in *Handbook of Conducting Polymers*, edited by T. A. Skotheim (Marcel Dekker, New York, 1986), Vol. 2, Chap. 22.
- [71] W. P. Su, *Solid State Commun.* **42**, 497 (1982).
- [72] E. Fradkin and J. D. Hirsch, *Phys. Rev. B* **27**, 1680 (1983).
- [73] E. Fradkin and J. D. Hirsch, *Phys. Rev. Lett.* **49**, 402 (1982).
- [74] F. Guinea, *Phys. Rev. B* **30**, 1884 (1984).
- [75] W. H. Press, S. A. Teukolsky, W. T. Vetterling, and B. P. Flannery, *Numerical Recipes in Fortran, second edition* (Cambridge University Press, London, 1992).
- [76] G. Bachelet, D. Hamann, and M. Schlüter, *Phys. Rev. B* **26**, 4199 (1982).
- [77] H. Hellmann, *Einführung in die Quantumchemie* (Deuticke, Leipzig, 1937).
- [78] R. Feynman, *Phys. Rev.* **56**, 340 (1939).

**GRADUATE SCHOOL
UNIVERSITY OF ALABAMA AT BIRMINGHAM
DISSERTATION APPROVAL FORM
DOCTOR OF PHILOSOPHY**

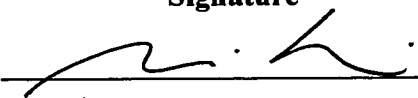


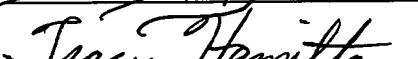
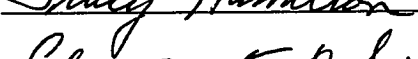
Name of Candidate Todd Edward DeVore


Major Subject Physics


Title of Dissertation Ab Initio Molecular Dynamics Simulation of Charged and
Neutral Solitons in Polyacetylene

I certify that I have read this document and examined the student regarding its content. In my opinion, this dissertation conforms to acceptable standards of scholarly presentation and is adequate in scope and quality, and the attainments of this student are such that _he may be recommended for the degree of Doctor of Philosophy.

Dissertation Committee:

Name	Signature
<u>Ryoichi Kawai</u> , Chair	
<u>Joseph G. Harrison</u>	
<u>David G. Agresti</u>	
<u>Tracy Hamilton</u>	
<u>Charles Katholi</u>	

Director of Graduate Program 

Dean, UAB Graduate School 

Date 9/19/99